Discrete element modelling of concrete behaviour

By

SANMOUGA MAROODEN

MEng (Hons)

A DISSERTATION

Submitted to

The University of Liverpool

in partial fulfilment of the requirements
for the degree of

MASTER OF PHILOSOPHY

In Civil Engineering

April 2018

ABSTRACT

DISCRETE ELEMENT MODELLING OF CONCRETE BEHAVIOUR

By

Sanmouga Marooden

This work presents the study of a three-dimensional (3D) simulation of the concrete behaviour in a uni-axial compressive test and flexural test using discrete element modelling (DEM). The proposed numerical models are namely, unreinforced cylindrical concrete under a uni-axial compressive test, unreinforced concrete beam under three-point flexural test and lastly, steel reinforced concrete beam under four-point flexural test. Those models were built up with fish programming language and python programming language (see Appendix A1 for the code created) and run into a computer program namely Particle flow code (PFC 3D). The main aim of this paper is to validate those numerical models developed and to study the cracking initiation and failure process in order to understand the fracture behaviour of concrete. The particles were distributed using an algorithm that is based on the sieve test analysis. The parameters were set up in order to validate the numerical model with the experimental result. It was observed that all the three models developed show a strong correlation with the laboratory experiment in term of stress-strain response, load-displacement response, crack pattern and macroscopic cracks development. Once, the bond between the spheres is broken, it leads to the formation of microscopic cracks which is not visible in laboratory experiment. DEM can help to identify which part is more prone to the evolution of microscopic cracks to macroscopic cracks under the discrete fracture network. In addition to, the rosette plot allows identifying the orientation that leads to a significant amount of micro cracks which is essential for designing structures. From the observation recorded in this research, it was observed that DEM is capable to reproduce concrete behaviour both quantitatively and qualitatively. It is also possible to measure the strain energy stored in the linear contact bond and parallel bond. At yield point which corresponds to the maximum amount of microcracks recorded, that strain energy is released in the form of kinetic energy, frictional slip energy, energy of dashpot, local damping. This can be extended further to compute fracture energy in the future work. Hence, it can be concluded DEM can be used to study the heterogeneous nature of concrete and as well as randomness nature of the fracturing of concrete structure.

Index terms: DEM, PFC 3D, concrete, fracture, cracking, uni-axial compressive test, unreinforced flexural test, Steel reinforced flexural test

DECLARATION

I hereby certify that this dissertation constitutes my own product, that where the language of others is set forth, quotation marks so indicate, and that appropriate credit is given where I have used the language, ideas, expressions or writings of another.

I declare that the dissertation describes original work that has not previously been presented for the award of any other degree of any institution.

Signed,

Sanmouga Marooden

March 2018

ACKNOWLEDGEMENTS

I would like to first and foremost thank Dr. Guobin Gong for his excellent supervision and support throughout this project. I am indebted to him for his invaluable encouragement, enthusiasm and advice. I would also like to express my appreciation to Dr. Ryan Judge, Dr. Jun Xia, Dr. Chee Seong Chin and Dr David Liu for reviewing my work and offering their valuable suggestions and comments. I would also like to thank Dr. Isaac Galobardes for extending his help during the course of this project.

This research was mainly funded by XJTLU Research Development Fund and I am grateful to them for providing me with this 2-year fully Funded Scholarship.

I would like to thank Almighty God for giving the courage along the way. I would like to thank this special person Marco Dinninghoff who gave me the strength and support to finish this MPhil. I would also like to thank my family for their love and support. Finally, I would like to thank Bhooma Nepal and Abhipsa Sahu for their constant encouragement.

TABLE OF CONTENT

List of Tables

List of figures

Nomenclature

Latin Alphabets

K^n: Normal stiffness at contact

F_i: Total force acting on particles i due to contacts with other particles or walls

$\ddot{x}_i$: Acceleration of particle

g_i: Body force acceleration vector (Gravity loading)

I_1, I_2, I_3: Principal moment of inertia

I_{pb}: Moment of inertia of parallel bond

J_{pb}: Polar moment of inertia of parallel bond

M_1, M_2, M_3: Component of resultant moment about the principal axes

G: 'gain' parameter estimated

N_c: Number of contacts on the wall

F_{ij}**:** Fabric tensor

Z: Coordination number

Greek Alphabets

$\dot{\omega}_1, \dot{\omega}_2, \dot{\omega}_3$: Angular accelerations about the principal axes

$\Delta\sigma^{(w)}$**:** Change mean wall stress

δ_n: contact normal displacement

$\bar{\sigma}_{ij}^{p}$: Average stress tensor

Acronyms

DEM: Discrete Element Method

FEM: Finite Element Method

SHPB: Split-Hopkinson bar

PFC: Particle Flow Code

LAT: Laser Aided tomography

CT: Computer Tomography

ITZ: Interfacial Transition zone

Chapter 1. Introduction

1.1 Background of study

Concrete is a mixture of cement paste, fine aggregate and coarse aggregates. As such, it is difficult to solve the fracture mechanism of heterogeneous solids numerically because there is always creation and continuous motion of new surfaces. It is not appropriate to make use of homogenous approach to methodically analyse these mechanisms because fracture pattern is composed of main crack, micro crack, tortuosity and crack branching. With the application of both analytical and experimental methods, several micromechanics-based approaches have been studied broadly for non-interacting inclusion of heterogeneous materials (Voigt, 1889; Einstein, 1911; Reuss, 1929; Paul, 1960; Hirsh, 1962; Hashin, 1965; Christensen and Lo, 1979). However, using a closed-form solution, it was difficult to predict the behaviour of interacting inclusions in heterogeneous solid as such, with the increasing computational power during the past decade, numerical approximation could be used to study cementitious materials (Rothenburg et al., 1992; Schlangen and van Mier, 1992; Bazant and Jirasek, 1994; Bolander and Saito, 1997; Mohamed and Hansen, 1999; Chang et al., 2002; Sadd et al., 2004).

The “n-body” problem studies the evolution of a system of “n” bodies subjected to Newtonian gravitational forces but nevertheless, there is no general closed solution for the problem with more than 3 bodies. The similarities between the classical ‘n-body’ problem and the interaction of large system of particles have attracted the attention of physicists for hundreds of years (Rapaport, 2004). Likewise, throughout 300 years of research conducted by notable scientists such as Bagnold, Coulomb and Reynold, yet, the understanding and the application of the stress response of granular materials to real applications has remained abstract and elusive. As a result, computer model such as numerical methods is necessary to analyse those complex systems. Malvern, (1969) mentioned about three different independent assumptions for instance isotropy, homogeneity, continuity is made in classical continuum mechanics and Khan and Huang, (1995) referred the idealization of material to be the continuum model of the material. The micromechanical behaviour of granular materials which comprises of void and grain in contact are anisotropic, inherently heterogeneous and discontinuous in nature. Moreover, the determination of constitutive model in continuum mechanical analyses of granular materials is tedious process even though the mechanical interaction between particles are simple and the material constant is explicit (Kishino, 1998). This is because continuum approaches involve material parameters or constants which does not have a clear physical meaning (Kishino, 1998).

The implicit expression of the geometry of a packed assembly of particles could be the source of the ambiguity in the material constants. Hence, it can be more realistic and reliable to analyse granular materials using discrete element method which adopts an explicit approach.

Ideally, an attempt has been made to reduce laboratory expenditures by studying the material's behaviour through numerical simulations in which its primary goal is to accelerate a normally trial and error experimental processes. The recent dramatic increase in computational power available for mathematical modelling and simulation raises the possibility that modern numerical methods (like DEM) can play a significant role in the analysis of the micromechanics of granular composite materials like concrete. Besides, the peculiar nonlinearity behaviour that occurs in the fracture zone ahead of an opening crack makes the theory distinctly different from the range of problems in classical continuum mechanics, see Griffith, (1921), Hillerborg et al., (1976) among many others. Hence, this highlights a challenging feature of this research area because of the frequent encounter of multi–cracks systems in real problems that require an efficient analysis approach for instant DEM.

1.2 Research Aim and Objectives

Discrete Element modelling has advanced due to the increase in computational power and thus, this research proposes to use this approach as an alternative numerical method to continuum-type methods for the study of concrete behaviour. This will help to understand the behaviour of concrete structure in order to improve the safety and prevent disastrous consequences due to fracture. DEM Models are developed and explicitly used to reproduce the macroscopic behaviour of concrete in order to gain a better understanding of fracture mechanism of concrete.

The main aim of this paper is to validate numerical models developed and to study the cracking initiation and failure process in order to understand the fracture behaviour of concrete.

The following are the distinct objectives of this research:

1. The development of three-dimensional numerical models based on a uniaxial compressive test, a three-point flexural test of unreinforced concrete and four-point flexural test of steel reinforced concrete in order to analyse the concrete behaviour.
2. The models, namely uniaxial compressive test, three-point flexural test and the four-point are calibrated and validated against experimental results.

3. The validated models are used to investigate the evolution of microcracking and macrocracking both numerically and experimentally.
4. The study of the application of Particle flow code (PFC3D) to the simulation of concrete which includes particles generation technique, contact model, micromechanics of cracking.

1.3 Scope and limitation of study

This research will encompass the modelling of both unreinforced and reinforced concrete. In addition to, the brittle behaviour of concrete media by simulating the initiation, propagation, and interaction of local cracks will be simulated through DEM using particle flow code (PFC). A heterogeneous fracture model based on discrete element model (DEM) namely 3-point bending test, 4-point bending test, the uniaxial compressive test will be developed to investigate concrete behaviour. Additionally, since the local physical contact mechanism is very complex and this research will study how the macroscopic behaviour is affected by the microscopic behaviour. This study will not encompass the study of cracking in the laboratory due to limited equipment available in the XJTLU lab.

All the numerical modelling for instance, discrete element modelling which is used in this project is developed from mathematical models which are based on the assumptions to an approximate reality. Thus, these assumptions made for mathematical simplicity compromise on the precision to represent the real scenario of the material behaviour. For instance, in DEM, a sphere is assumed to be non-deformable and this is not the case at high stresses. Thus, it is important to understand that numerical simulations are only meant for the understanding and the representation of real scenario.

1.4 Significance of study

It was noted through the literature review in chapter 2 that there is a large discrepancy in present development of three dimensional models due to lack of extensive validation studies because of the research focuses mainly on two dimensional models. Also, the numbers of sphere used in those previous researches do not represent the actual scenario of concrete aggregates. Also, the previous results obtained are not quite satisfactory particularly when it comes to flexural test of unreinforced and steel reinforced concrete beam. As such, there is a high need to perform research in this area. Thus, this thesis will help to cover in those research gaps. Moreover, discrete element modelling could be used as one of the key research tools to study fracture and the behaviour of concrete by looking into its micromechanics response. The knowledge gained from this research will further help to enhance the constitutive models of continuum modelling.

Moreover, this research will help us provide the information on mechanisms which happens at particle scale and cannot be visualized in the laboratory. In an attempt to reduce the laboratory expenses, material's behaviour will be simulated through DEM, with the primary goal being able to accelerate a normally trial and error experimental processes.

This study will strive to explain the macrocracking of concrete through identification of the initiation and propagation of micro-cracking. Design of civil engineering structures needs to take into account the impact of severe loadings related to anthropogenic or natural hazard for instance aircraft, missile impact and rock fall which can induce immense damage to concrete structure. However, although the Codes of Practice (e.g. EC 2 and GB 50010-2010) require designs to meet crack width requirements for the service limit state (SLS), yet, the propagation of cracks (cracking) may be uncontrolled once cracks are initiated. As such, this kind of simulations is necessary in order to assess the vulnerability of structure due to impact response characteristic and failure mechanism.

1.5 Dissertation Layout

Chapter 1 comprises mainly of the background of study, research objectives and scope and significance of study.

Chapter 2 reviews the development and application of DEM in concrete. It also describes the theory and background of discrete element method. The computer program particle flow code (PFC3D) is also described here.

Chapter 3 presents the methodology that will be used in the numerical studies and the experimental studies. It also presents the method that can be used in the laboratory to study cracking.

Chapter 4 presents the three numerical models developed (Uniaxial compressive test, three-point flexural test and four-point flexural test). The three numerical models were validated against experimental result. The microcrack in term of cracking number, cracking opening diameter, cracking dominance and cracking orientation was studied. The energy stored and dissipated during the on-going fracture was quantified and studied.

Chapter 5 summarises the conclusion of this research and presents the recommendation for future work.

Chapter 2. Review of Discrete Element Method

2.1 Discrete Element Model

Discrete element modelling (DEM) is a numerical method which was gradually developed by Cundall, (1971) and it is used to simulate the micromechanical behaviour of geotechnical block and particle group in geotechnical, structural and pavement engineering owing to its perks of solving large deformation and discontinuous medium. Peter Cundall and Otto Strack proposed and described the basic formulation for distinct element method of granular materials in two of the reports (Cundall and Strack, 1978 and 1979b) that were published in National Science foundation and subsequently, a paper was published in the journal Geotechnique (Cundall and Stacks, 1979a). The advantages of using this approach are that each individual particle in the particular granular material and their interactions are explicitly analysed. Also, to reduce the computational cost of simulation in DEM, the particles shapes are simplified using spheres and a basic model of contact response are implemented. Hence, this allows a large number of particles to be analysed while still capturing the salient response characteristics of granular material behaviour. DEM is a numerical method or simulation method whereby finite rotation and displacement of discrete bodies are simulated (Cundall and Hart, 1992). The unique features of using DEM are that loads and deformations can be applied virtually to the sample by researchers. Besides, in a physical laboratory test, it is incredibly difficult to access all the information and data of the particle scale mechanism that underlies the complex overall material response. However, the particle scale mechanism could be monitored and analysed efficiently through DEM approach. Discrete element modelling permits us to understand the macro-scale response in term of the evolution of the contact forces, the particle orientation the fundamental particle interactions underlying the complex, the particles and orientation within the materials.

Currently, there are two micromechanical models which can be divided into two categories namely, discrete element method (DEM) and finite element Method (FEM). Finite element method is based on fracture mechanic and continuum damage theory and it is efficient in stress-strain distribution and the effect on the stiffness anisotropy (Sadd and Dai, 2005; Dai and You, 2007; Kim et al., 2008) but it is limited by the convergence difficulties in modelling which alter the aggregate contact geometry in 3D. Alternatively, DEM's particulate system analyses the rotational and translational behaviour using Newton's second law on each particle with proper contact force at the interface. In fact, DEM has several advantages over FEM that is the discrete nature of concrete can be model explicitly. Secondly, there is no convergence problem in DEM

which are namely caused by moving boundary condition and changing contact. Besides, DEM can support and model large deformation and frictional sliding between particles.

The numerical technique used in DEM can be divided into two categories namely soft sphere models and hard sphere models also called event-driven approach (Duran, 2000 and Zhu et al., 2007). The difference between the two methods in each category is that particles are said to be "soft" whereby case penetration is allowed at contacts and particles are said to be "hard" whereby no deformation or penetration occurred. Delaney et al., (2007) claimed that event-driven modelling approach (hard sphere approach) which is derived from the equations governing momentum exchange and the particle contact force is computationally cheaper than any other methods. Poschel and Schwager, (2005) described two native algorithms for implementations of an event driven computer code. However, it fails to capture those fine details of the response of dense materials that involve multiple simultaneous contacts and also there is a limitation to accurately model the frictional or tangential force between interacting particles (Delaney et al., 2007). Campbell, (2006) stated that in granular material, the real mechanism of force transfer involves deformation of contacting particles; hence, it is inappropriate to use event-driven modelling approach in dense systems.

O'Sullivan, (2002) mentioned about various algorithms that exist under "soft sphere" category, yet, the most commonly approach used is described by Cundall and Stack, (1979a) namely distinct element method and the terms "discrete element method" and "Distinct element method" are used interchangeably. Yet, strictly speaking, "distinct element method" is a type of discrete element method. Moreover, there are two types of discrete element model used namely block DEM and particulate DEM which are made up of several individual bodies either in term of blocks (clumps) or particles that can move and rotate relative to each other. Contacts can be formed and upon deformation, these contacts can break and new contacts can be formed between bodies in a system. Usually, there is slight overlapping at the contact which is akin to deformation between individual bodies. Simple "contact constitutive models" are used to relate the overlapping of particles between and contact forces between the bodies. The moment induces to the bodies are contributed by the shear components of the contact force. Moreover, by considering the dynamic equilibrium of each particle and taking into consideration the contact forces and the inertia of the body, the acceleration of the particles can be determined. From the computed acceleration, displacements of the body over time increments can be calculated. As such, the evolution of the whole system can be simulated over a span of small time steps.

A DEM simulation is carried out by inputting the geometry, the particles coordinates and boundary conditions of the system that need to be analysed by the user. The user specifies the material properties' inputs by the contact model parameters which include namely the stiffness and friction coefficient. Besides, a schedule for loading and deformation of the system is specified by the operator whereby the simulation progresses as a transient or dynamic analysis for a specified interval of time increments and at each time step contacting particles are identified. The magnitude of the inter-particles forces is a function of the distance between contacting particles. Hence, the resultant force and torque or moment on each individual body could be determined through the calculated inter-particle forces. At each time increments, two sets of dynamic equilibrium are solved except for the case whereby the particle rotation is restrained. The rotation motion is determined from the resultant applied moment and the resultant applied force is used to determine the translational movement of each body. The translational and rotational accelerations of the particle can be calculated if the particles inertia is known. Through simple central-difference-type integration through time, the displacement and rotation of the particles over the current time-step could be determined. Besides, Thornton and Antony (2000) and Itasca (2004) stated that the resultant forces and moments that induce this translational and rotational acceleration on these bodies in the system are called "out-of-balance" forces. The particle position and orientation are updated in the next time step using the incremental displacements and rotations. Based on this updated geometry, the contact forces are calculated and the series of calculations are repeated. Hence, a discrete element analysis is, therefore, a transient or dynamic analysis, even if the system of interest is responding in an almost static manner.

2.2 Literature review of discrete element modelling study in concrete

2.2.1 Compressive test

Iturrioz et al., (2013) used a three dimensional lattice model (Truss-like DEM) to model predamage concrete specimen under uniaxial compression test. The validation of the numerical model is line in the laboratory result. The advantages of using this truss-like Discrete Element Method is that it can be implemented with problems that have complex geometries. Nitka and Tejchman, (2015) performed a discrete element modelling of uniaxial compressive test using the model already developped by Univeristy of Grenoble with the work of Kozicki and Donzé, (2008) and Šmilauer and Chareyre, (2010). The specimen used was a cube of 100 ×100×100mm with a particle size (dmin: 0.125mm and dmax: 8mm). Nitka and Tejchman, (2015), mentioned that

the 3D result is much more closer to the experimental one unlike the 2D results. However, most of the the work of Nitka and Tejchman, (2015) was mainly focused on 2D modelling of concrete. Beckmann et al., (2012) conducted a 2D simulation of concrete using discrete element method in order to study crack initiation and failure process. A 10 cm concrete prism model with 5000 particles under uniaxial compressive test was simulated. Based on vectorizable random lattice algorithm developed by Moukarzel and Herrmann, (1992), particles with convex shape and same size were generated. It was found the crack patterns were similar but the exact locations were not identical. Katsaga, (2010) conducted a uniaxial compressive test on a 2D model of concrete. Using a CT images coupled with AutoCAD, the shape of the real aggregate is transferred into PFC2D. Upon validation of the stress-strain response and the cracking pattern, it was observed that the numerical result is satisfactory.

Gyurkó et al., (2014) modelled numerically (2D) the compressive strength of a 150 mm standard concrete cubic sample of concrete and validated through laboratory results. It was observed in the all the cases of the five models tested, that upon plotting deviatoric stress against axial strain, there is dissimilarity between the model and the experimental result at the initial stage. The curve at the initial stage for the DEM model is wavy in contrast to the experimental one which was linear. It was also observed that there was a rapid increase of the stress with small increment of strain. However, later on, it was a reverse phenomenon that was observed. The increase in strain didn't cause any significant increment of the stress. Gyurkó et al., (2014) concluded that after the material genesis procedure, the model was stable that is there was no bond breaking or deformation. It was observed that there was deformation (local behaviour of the material) in the vicinity of the loading planes where some parallel bonds between particles broke. Nevertheless, after several cycles, the pressure has influenced the whole sample and the local behaviour has turned into global. Moreover, it was found that model gives a reasonable result which varies 3 to 5% from that of the experimental one. Hence, Gyurkó et al., (2014) concluded that DEM modelling is capable of modelling uniaxial compression test and the result obtained strongly correlate with that of the laboratory observations.

Suchorzewski et al., (2017) studied numerically (2D and 3D) and experimentally the fracture of concrete cubic specimens under uniaxial compression test. Suchorzewski et al. (2017)) performed a discrete element modelling of uniaxial compressive test using the model already developped by Univeristy of Grenoble with the work of Kozicki and Donzé, (2008) and Šmilauer and Chareyre (2010). It was found that the result obtained from the two-dimensional analysis was satisfactory unlike the three-dimensional analysis. Also, the model could predict the complex

path of the cracking patter which is in accordance with the observation made in the experiment. Abbasnia and Aslami, (2014) proposed a new model (2D) to simulate fracture of concrete under compression. The voronoi diagram method was used to generate the model. It takes into account the distribution of the fully graded aggregates at mesoscopic level and takes into account the random shape of the particles. High strength concrete can be simulated using this model. Abbasnia and Aslami, (2014) concluded that the numerical result is reasonably close to the experimental result. Hentz et al., (2002) studied concrete structure subjected to the impact of dynamic loading. The aim was to identify the correct parameter to be used in order to simulate the elastic, inelastic deformation and fracture of concrete. A uniaxial compression test model was used to calibrate the model parameters by adjusting the material properties of the assembly of discrete elements. The result obtained in contrast with the experimental result was reasonably good. However, Hentz et al., (2002) added that the perturbation in the packing disorder affects Young's modulus and Poisson's ratio. Hence, an energy criterion was introduced to modify the macro-micro constitutive equation through the interaction surface between the two discrete spheres.

Elkadi and Van Mier, (2006) has investigated numerically and experimentally the influence of specimen and aggregate size on concrete fracture under multiaxial compressive loading conditions. Scaled thick-walled cylindrical specimens which are of a size range 1:4 under external hydrostatic pressure were tested whereby the fractures around the inner opening were preserved and stress-induced deformation was monitored around it. Since aggregate size was one of the variables in the investigation; two different concrete mixtures of high similitude and different aggregate size (2mm and 4mm) were used in the experiment and the result is in good agreement with the classical size effect theory (Weibull theory) for three-dimensional similarity. PFC2D was used to analyse the experimental findings and it was observed that with an increase in specimen size, there was a decrease in stress. PFC 2D has proved its ability to simulate and yield the macroscopic material behaviour observed in the laboratory in term of reproducing realistic fracture patterns and damage development (damage zone) but however, more work is yet to be done in particular the calibration process for simulating complex test because simple tests are insufficient for calibration (Elkadi and Van Mier, 2006). Moreover, it was observed that inner and intra-granular crack typed were all mostly aligned parallel around the inner-wall and regardless, the specimen size, slitting mode was the principal failure initiation mechanism for both tested materials in the laboratory observations (Elkadi and Van Mier, 2006).

Hentz et al., (2004) did a quasi-static simulation of uniaxial compression and tension test to calibrate the model parameters and identify the numerical sample behaviour in order to simulate elastic and non-linear deformation, for instance, damage and rupture. A validation of the model was first conducted in the quasi-static domain and in dynamic compression at sample scale using a split Hopkinson pressure bar (SHPB) compressive test. The use of an interaction range was implemented which makes this model distinct from classical DEM. Hentz et al., (2004) observed that the stress state is similar to the experiment result. Nevertheless, Young's modulus and Poisson's coefficient was disturbed by the perturbations in the packing disorder and high dispersions were observed. As such, an energy criterion was introduced to modify the macro-micro constitutive equations of the model in order to reduce the dispersion. This method was efficient to capture quantitative results for instance peak strength in term of compression and tension and their associated fracture and strain energy. It could also be used to obtain the qualitative results such as failure patterns and softening in the post-peak region. Hentz et al., (2004) mentioned that the model doesn't require the use of viscosity or characteristic time to produce quantitatively the increase in compressive strength with the increase of strain rate. This confirms the inertia-based hypothesis whereby the increase in dynamic strength is associated with bulking (structural effect). Moreover, a further validation of this approach was conducted through a dynamic test and the concrete behaviour was investigated. As such it was found that the increase in local tensile strength cannot be explained by inertia only; it could be more of a material intrinsic effect (Hentz et al., 2004).

Zhou et al., (2016) used PFC2D to study the behaviour of fracturing in a concrete specimen with a circular hole and pre-existing crack under a uniaxial compressive test in order to better grasp the effect of different factors on the cracking behaviour. The model was used to study the initiation, propagation, and coalescence of cracks and corresponding stress and strain at each cracking stage. It was observed that the cracks include both primary and secondary cracks and also, the initiation location and stress of the first cracks depend on the preexisting crack inclination angle and ligament length. However, the stress and the displacement fields are disturbed by the initiation and propagation of the primary, secondary and coalescence of cracks. I was also observed that the circular hole tends to attract the propagating cracks. Nevertheless, Zhou et al., (2016) concluded that numerical result obtained in term of cracking pattern is similar to the experimental one. Su et al., (2017) modelled a concrete in two dimensional under a uniaxial compressive test using discrete element method. The stress-strain response obtained is in agreement with the experiments. Also, Su et al., (2017) concluded that DEM can simulate fracture process of concrete. Sinaie, (2017) performed a simulation of a uniaxial compressive test of

concrete to study size effect on the mechanical properties of concrete. Two-dimensional discrete element method was used to simulate the concrete samples with varying diameter and aspect ratio. Upon comparison of the numerical result to experimental result, it was observed that it is relatively good. Thus, it was concluded that DEM can capture many size effect features (Sinaie, 2017)

2.2.2 Flexural test

There are some works on flexural test conducted on asphalt concrete, for instance, Jun et al., (2012) and Ma et al., (2015) using PFC 3D. However, there are lesser people who studied flexural test of concrete using discrete element modelling. For instance, Hentz et al., (2009) used a 3D model which takes into account of the behaviour of concrete, reinforcement and their interface to study the reinforced concrete structure subjected to dynamic loading. The validation of the introduction of steel reinforcement was conducted prior the simulation of a real reinforced concrete structure subjected to dynamic loading. A 3D model of a four-point bending which comprises of a line of discrete elements amongst the concrete discrete element to represent the reinforcement was created. Hentz et al., (2009) added that the model should further be improved because the strength of the beam is overestimated due to the free rotations. Moreover, it was observed that crack starts on the lower face of the beam below the loading point and propagates towards the inner sides and this is similar to the experiment results.

Tavarez et al., (2002) modelled a rectangular fixed ended beam under impact loading. A modified version of the program (TRUBAL) developed by Cundall and Stack, (1979) was used to model granular materials like concrete. Megaclusters concept was used to represent the assembly of the beam. The damage was evaluated both quantitatively and qualitatively through numerical simulation only. Hentz et al., (2009) modelled a three-dimensional model of steel reinforced concrete beam under a four-point flexural test. The beam has a dimension of 120mm height, 60mm width and 1600mm length with 9000 spheres. The reinforcement comprises of two longitudinal steel bars of diameter 6mm. For simplicity, the transversal bars and the stirrups are not modelled. Upon validation with the experimental, it was observed that the elastic phase of numerical result is relatively good. However, the second phase began a bit late due to high stiffness as explained by Hentz et al., (2009). It was proposed to use high local softening value to counterbalance the free rotations when the concrete cracked. It was also observed that the cracking pattern is similar to the experimental one.

2.2.3 Other DEM applications on concrete

Haeri and Sarfarari, (2016) conducted a numerical simulation of tensile failure of concrete using Particle flow code (PFC). Both numerical simulation (PFC 2D) and experiment test are based on compression-to-tension load transformer device (CTT) test, Brazilian tensile test (splitting test), Direct tensile test, modified tension test and ring tests. Moreover, for the conformity of the simulated numerical response, calibration of PFC was conducted using the data obtained from Brazilian test. They observed that failure process and failure pattern in the numerical testing was reasonably in accordance with the experimental results. Haeri and Sarfarari, (2016) used numerical testing and found that the macro fractures in the models are caused by the microscopic tensile breakages on a large number of bonded spheres. Moreover, they also added that upon comparing the tensile strength result obtained, it was concluded that the result obtained from the modified tension test was somehow akin to the direct test result. Hence, a modified tension test could be a replacement for direct test and besides, it is easy to manipulate and used in contrast to other equipment.

Shiu et al., (2005) modelled a concrete slab under a missile impact in three dimensions. The model of the slab comprises of four layers of reinforcement and 17408 spheres. The numerical result was validated by the experiment performed by French Atomic agency and French Electrical Power Company (check report of Sokolovsky et al., (1977). The result obtained from the numerical model shows that perforation, scrabbing and penetration obtained. Upon comparing the numerical result obtained from 3 different velocities namely 102, 151 and 186 m/s against the experimental result, it was observed that the numerical model overestimates the missile penetration particularly in the case of velocity 102 m/s. Overall, the qualitative result is almost similar in respect to the experimental result. Tran et al., (2011) has modelled a three-dimensional concrete model under high triaxial loading through discrete element method (YADE program). A local elastic-hardening-damage constitutive law was formulated in DEM in order to reproduce the response of concrete at high confining pressure. The model was constructed in a cylindrical form with a height of 0.14 m and a diameter of 0.07 m. The number of discrete element in this model was around 10000. The experimental result obtained from the uniaxial compression-traction test was used to calibrate the model's parameter. However, the uniaxial compression test was not enough to calibrate the full irreversible behaviour of the model. Thus, a hydrostatic test was performed to obtain the required missing parameters. After validation with the experimental results, it was observed stress-strain responses and the volumetric curves are quite satisfactory.

2.2.4 Summary of literature review

Based on the above literature review of previous researchers, it was noted that presently, there is a large discrepancy in the development of three-dimensional numerical models to study the behaviour of concrete under loading. There is a lack of extensive validation studies because most of the present researches focus mainly on two dimensional numerical models. When it comes to studying fracture, three-dimensional model gives a full overview of the cracking behaviour. Most of the previous researcher's works neither represent the actual aggregates number nor the aggregates size distribution based on the sieve analysis test. As such, those numerical models do not represent the actual scenario. Moreover, it was observed that most of the results obtained especially when it comes to 3D modelling, was not satisfactory or relatively good.

There is less research work done concerning the three-dimensional discrete element modelling of an unreinforced concrete beam under a three-point flexural test. Similarly, there is a discrepancy in the study of steel reinforced concrete beam under four-point flexural test. Hentz et al., (2009) did simulate steel reinforced concrete beam under four-point flexural test. However, the reinforcement bars were only restricted to the main bar only. The traverse bars and the stirrups were not simulated. As such, the numerical result was quite not matching the experimental result.

Hence, it is concluded that there is a research gap in this area. Thus, this thesis will help to address those research gaps and particle flow code (PFC) will opt as a computer program to run the programming codes.

2.3 Recent Development in experiment methodology to study cracking

Computer tomography was a promising tool that was used as a non-invasively method to study internal structure (Lee, 1994) but it is complex and time consuming to visualise the fabric and its evolution. Konagai et al., 1992 developed a new experimental method called laser-aided tomography (LAT) is be able to visualise the three dimensional model of the interlocking structure of coarse to fine particles. However, some improvements need to be done upon the use of called laser-aided tomography (LAT) when it comes to fine particle less than 1mm which hard to be identified (Konagai and Rangelow, 1994b; Rangelow and Konagai, 1995). In tests for instance, triaxial and plane strain test of dense granular material, there is a development of shear bands where strains are highly localised. As such, if stress and strain are averaged over the specimen, they lose its physical meanings due to the heterogeneity of the material. Hence, a powerful tool such as computer tomography (CT) is required to determine the local strain not the global values.

Computer tomography is synonymous with the 'X-ray scanner' used commonly in medicine. There are several details provided by some papers such as Blumenfeld and Glover., (1981), Latiere et al., (1987), Colliat-Dangus et al., (1988), Raynaud et al., (1989), Bossi et al., (1990) and Desrues et al., (1996).

Skarżyński et al., (2015), studied the micro-structure of real concrete specimen based on 2D images by scanning electron microscope and 3D X-ray micro-computed tomography images. In order to simulate fracture processes in a three-point bending of concrete beams, Skarżyński et al., (2015) developed two different 2D meso-scale models based on high X-ray micro-tomography images. For instance, Figure 1 illustrates the cracking branching and width of the ITZs obtained by Skarżyński et al., (2015). Nemati, (1997) uses a scanning electron microscope to study the generation and interaction of effect of confinement on microcrack behaviour and the microcracks induced compressive stress. The Ultrasonic equipment which is used to detect defects in concrete such as cracks is a portable ultrasonic non-destructive digital indicating tester (PUNDIT). Kalyan and Kishen, (2013) used ultrasonic pulse velocity method where the detailed analysis of the effect of cracks and its extent deterioration which affects elastic modulus and compressive strength of concrete was studied. The comparison between the effect of the surface cracks and internal micro-cracks on the compressive strength was also studied by Kalyan and Kishen, (2013).

Nevertheless, there are other methods based on a non-destructive evaluation that have been developed. For instance, acoustic emission according to Newman, 1996, is the oldest non-destructive testing methods for detecting cracks and growth of microcracks in concrete. Besides, Jones, (1962) mentioned that ultrasonic pulse velocity is a popular method for crack detection as well as to evaluate the quality of concrete. In ultrasonic technique method, the intensity of deterioration due to cracks in concrete structure affects the wavelength and amplitude of the signal recorded. Moreover, holography is another non-destructive testing technique for cracks (Luxmoore, 1973). The use of capacitance strain gauge to continuously monitor of crack was introduced by Owen, (1976) and the presence of cracks around or near the gauge location is identified by a sudden drastic change in strain values. However, it was limited to few applications because the capacitance gauges need to be spot-welded on the surface to be monitored. Katsaga, (2010) developed a numerical approach to study fracture processes in concrete in order to investigate the fundamental aspect of fracture behaviour in concrete. Geophysical methods such as Acoustic Emission technique, ultrasonic wave velocity imaging, and high resolution Computed tomography were employed to validate the model behaviour. Katsaga, (2010)

concluded that geophysical imaging technique coupled with advanced numerical micromechanical modelling can be used to understand damage formation and evolution.

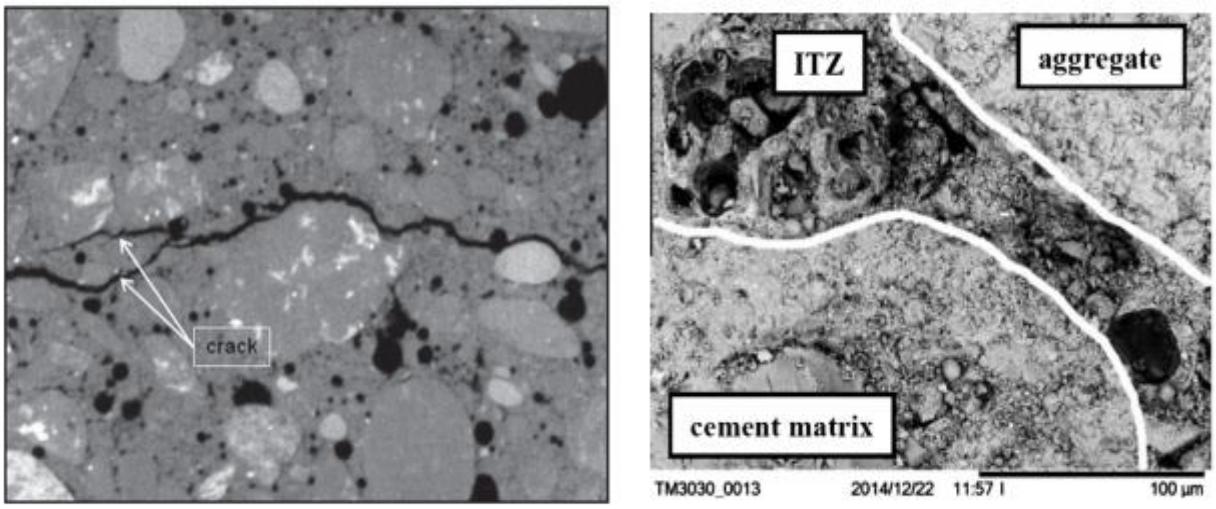

Figure 1: Cracking branching using a 3D micro-CT image (left) and (right) scanning electron micrographs of ITZ (Skarżyński et al., 2015)

2.4 Particle Flow Code in three dimensions (PFC3D)

2.4.1 PFC description

PFC (Particle Flow Code) was developed by ITASCA Consulting Group INC. It is a computer program that can model the interaction and movement of spheres which is based on Discrete Element Method initially developed by Cundall and Stack, (1979). Cundall and Hart, (1992) classified it as discrete element code because it allows finite displacement and rotations of discrete bodies. It can be either operated in 2D or 3D and calculations are taken over a series of time-steps. Hence, this ease the work on the computer memory since a series of time-steps are performed, as such, there is no need of an implicit scheme which requires of storing and reapplying matrices. Nevertheless, this program running time could be lengthy considering the fact that each step takes a fraction of second and this can be an issue on applications which need a large amount of particles to simulate the system (Lorig et al. 1995; Itasca, 2004). Usually, a problem which involves a form of interaction that is there is motion and interaction between the particles can be solved using PFC software. Moreover, the different amount and quality of cementation in concrete that is the variation in term of the strength, quality, and stiffness of the

bonding coupled with other relevant micromechanical properties of the system could be modelled to understand the behaviour of macro-mechanical properties. The perks of using PFC3D are that it is more efficient as it composes of circular objects which facilitate the contact detection, unlike angular objects. Secondly, it is possible for block made up of bonded particles to break unlike in UDEC and 3DEC and besides, there is no limit to the magnitude of displacement that can be modelled.

However, it is possible to model the damage behaviour in PFC3D by introducing a bond at the contacting points. For instance, if the inter-particle force exceeds the specific bond strength at contact in either normal or shear direction, the bond breaks. Hence, this gives path for tensile force to be formed which includes the formation of micro-cracks. The stress and strain can be computed by averaging their quantities over a representative measurement volume and it is possible to model the macroscopic behaviour such as dilation, fracture, and strain softening by treating the system to be an assembly of small particles.

The procedure to perform a PFC3D simulation is to first outline the model to be analysed. This means including particles or any walls essential to present the system. Then, the information could be either input into PFC either by command line or by an input coded file save as “file.dat” form. The programmer assigned the number of cycles to perform and thus, allows the particles to interact accordingly. The cycling is then repeated until the model is fully completed. At each step, with the double integration of newton’s second law, updated new positions and velocities are acquired given a set of contact forces acting on the particle. It should be noted unlike the continuum models, one can utilise different theoretical models to account for the behaviour of different material which facilities the transition to PFC efficiently and hence, one could vary different micromechanical properties in order to analyse the different macro-mechanical response. Nevertheless, in contrast with FLAC (Itasca, 2005) and UDEC, the specification of the properties, geometry of the problem and solution condition is not direct in PFC 3D. Moreover, unlike in continuum models, the setting of boundary condition is more difficult and complex because it does not consist of planar surfaces. Since forces arise from relative positions of spheres in the system, hence the initial stress can’t be independent of initial packing as such a compacted state cannot be pre-specified because there is no unique to pack a number of particles in a system.

2.4.2 Basic calculation cycle of Particle flow code (PFC)

PFC calculation cycle (Illustrated in Figure 2) is based on a time stepping algorithm which recurrently applied the force-displacement law to each contact, the law of motion to each particle and constantly updating the wall position. At the beginning of each time step, a set of contact information is updated based on the known positions of the particles and wall. Then, the updated contact force based on the relative motion between two particles is calculated by the force-displacement law through the contact constitutive model and the relative displacement from previous time step. Using the law of motion, the position and velocity resulting from the force and moment; which arises due to the contact force acting on the particle, can be resolved. During the simulation existing contacts (ball to ball or ball to wall) can break automatically and new contacts may be formed.

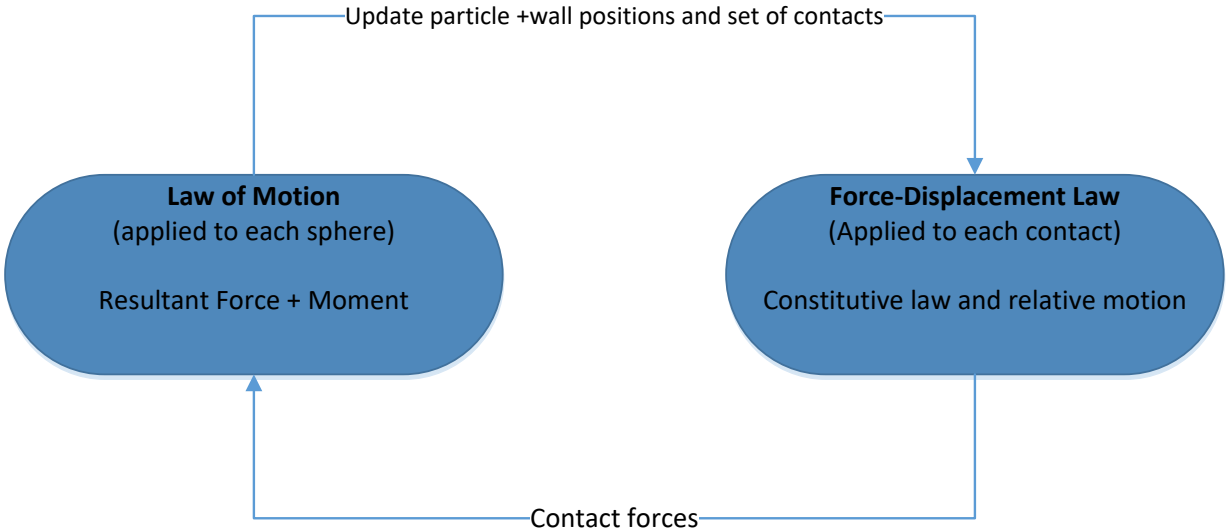

Figure 2: Calculation cycle

2.4.2.1 Stochastic generation of particles in PFC 3D

There are two methods that are used in PFC3D to generate and randomly place particle namely dynamic method and Simple Sequential Inhibition method. One of the approaches which fall under dynamic method is to place a required number of particles with a diameter less than the final one. Then, the diameter of the particles is gradually increased until a dense arrangement is achieved. An alternative way which falls under dynamic method is to assign a final size into a large domain and the walls are slowly moved inwards until the desired density is achieved. These

two dynamic methods both involve multiple collisions in order to achieve a dense arrangement during the densification process.

There is a different stochastic method which forms part of another set of approaches called constructive algorithms namely Simple Sequential Inhibition (SSI) model where spheres of equal diameter are placed at random positions sequentially in the domain. However, if a newly generated particle intersects the previous one, the new particle is discarded and the process continues to make the next attempt. This process stops until no more particles can be placed in the domain of interest. Nevertheless, a user-defined grain size distribution can be implemented using PFC 2D and PFC 3D (see, Döge, G., 2001).

However, in this research, the size of aggregate used in this numerical model is based on the actual particle size distribution obtained from the sieve analysis test conducted in the laboratory. An algorithm coded using fish programming was developed in order to represent the realistic particles size distribution. As such, this numerical model mimics the realistic particle size distribution based on result from the sieve analysis.

2.4.2.2 Force-Displacement Law

The force-displacement law is implemented in order to obtain the new contact force. This law is applied to both balls to wall and ball to ball contacts at the beginning of each cycle.

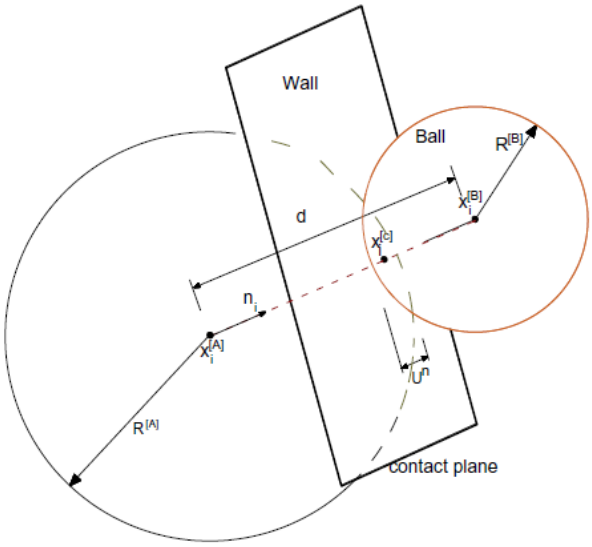

Figure 3: Ball-Ball contact

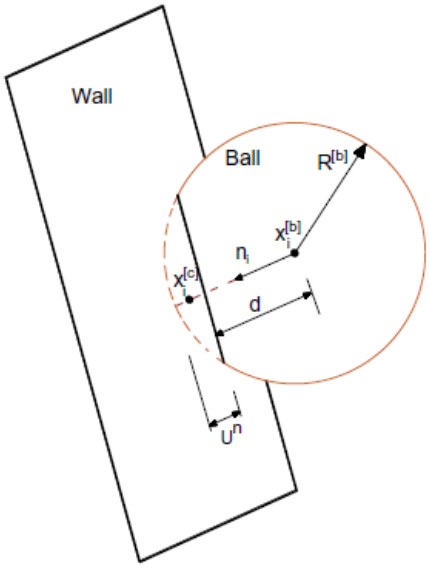

Figure 4: Ball to Wall contact

For ball-ball contact (illustrated in Figure 3), the unit normal vector, n_i that defines the contact plane is expressed as:

$$n_i = \frac{x_i^{[B]} - x_i^{[A]}}{d} \qquad (ball - ball) \qquad (2.1)$$

where;

$x_i^{[B]}$ and $x_i^{[A]}$: position vectors of the centres of balls A and B

Whereby the distance between centroids of the balls is given by:

$$\mathrm{d} = \left|x_i^{[B]} - x_i^{[A]}\right| = \sqrt{\left(x_i^{[B]} - x_i^{[A]}\right)\left(x_i^{[B]} - x_i^{[A]}\right)} \qquad (ball - ball) \qquad (2.2)$$

The overlap, U^n, defined to be the relative contact displacement in the normal direction is given by:

$$U^n = \begin{cases} R^{[A]} + R^{[B]} - d, & (ball - ball) \\ R^{[b]} - d, & (ball - wall) \end{cases} \quad (2.3)$$

where;

$R^{[\Phi]}$: Radius of ball Φ

The location of the contact point as illustrated in Figure 3 and Figure 4 is given by:

$$x_i^{[c]} = \begin{cases} x_i^{[A]} + \left(R^{[A]} - \frac{1}{2}U^n\right)n_i\,, & (ball - ball) \\ x_i^{[b]} + \left(R^{[b]} - \frac{1}{2}U^n\right)n_i, & (ball - wall) \end{cases} \quad (2.4)$$

The contact force vector F_i (action of ball A on ball B and action of ball on wall) can be dissolved into a normal, F_i^n and shear component, F_i^s with respect with the contact plane as expressed below:

$$F_i = F_i^n + F_i^s \quad (2.5)$$

The normal force is derived directly from overlap as follows:

$$F_i^n = K^n U^n n_i \quad (2.6)$$

where,

K^n: Normal stiffness at contact

However, the shear force is derived incrementally as expressed below:

$$\Delta F_i^s = -k^s \Delta U_i^s \quad (2.7)$$

Where the increment shear displacement is expressed as follows:

$$\Delta U_i^s = V_i^s \Delta t \quad (2.8)$$

Based on the relative shear velocity vector expressed below:

$$\begin{aligned} V_i^s &= V_i - V_i^n \\ &= V_i - V_j n_j n_i \end{aligned} \tag{2.9}$$

The relative velocity vector at the contact is given by:

$$\begin{aligned} V_i &= \left(\dot{x}_i^{[C]}\right)_{\phi^2} - (\dot{x}_i^{[C]})_{\phi^1} \\ &= ((\dot{x}_i{}^{[\Phi^2]} + e_{ijk}\omega_j^{[\Phi^2]}\left(x_k^{[c]} - x_k^{[\Phi^2]}\right)) - (\dot{x}_i^{[\Phi^1]} + e_{ijk}\omega_j^{[\Phi^1]}\left(x_k^{[C]} - x_k^{[\Phi^1]}\right)) \end{aligned} \tag{2.10}$$

Using the following notation

$$\{\Phi^1.\Phi^2\} = \begin{cases} \{A,B\}, & (ball - ball) \\ \{b,w\}, & (ball - wall) \end{cases} \tag{2.11}$$

The shear force is derived as follows:

$$F_i^s = \{F_i^s\}_{rot.2} + \Delta F_i^s \tag{2.12}$$

$$\begin{aligned} F_i^{[\Phi^1]} &\leftarrow F_i^{[\Phi^1]} - F_i \\ F_i^{[\Phi^2]} &\leftarrow F_i^{[\Phi^2]} + F_i \\ M_i^{[\Phi^1]} &\leftarrow M_i^{[\Phi^1]} - e_{ijk}\left(x_j^{[C]} - x_j^{[\Phi^1]}\right)F_k \\ M_i^{[\Phi^2]} &\leftarrow M_i^{[\Phi^2]} + e_{ijk}\left(x_j^{[C]} - x_j^{[\Phi^2]}\right)F_k \end{aligned} \tag{2.13}$$

where;

$F_i^{[\Phi^j]}\ and\ M_i^{[\Phi^{j1}]}$: Force and moment sums for entity Φ^j

2.4.2.3 Law of motion

The moment vector and the resultant force which acts as a rigid particle are used to determine the motion of the particle. Newton's equations of motion are expressed as two vector quantities

namely, rotational motion of motion which is related to the resultant moment and translational degree of freedom (translational motion) which is related to the resultant force.

The **translation motion's** equation can be expressed in vector form:

$$F_i = m(\ddot{x}_i - g_i) \tag{2.14}$$

F_i: Total force acting on particles i due to contacts with other particles or walls

$\ddot{x}_i$: Acceleration of particle

g_i: Body force acceleration vector (Gravity loading)

The **rotational motion's** equation can be expressed in vector form:

$$M_i = \dot{H}_i \tag{2.15}$$

where;

M_i: Resultant moment acting on sphere

$\dot{H}_i$: Angular momentum of the particle

This relationship is based on a local coordinate system which is attached to the centre of mass of the particle. If the local system is oriented such that it lies on the principal axes of inertia of the sphere, this relationship reduces to Euler's equation of motion:

$$\begin{aligned} M_1 &= I_1\dot{\omega}_1 + (I_3 - I_2)\omega_3\omega_2 \\ M_2 &= I_2\dot{\omega}_2 + (I_1 - I_3)\omega_1\omega_3 \\ M_3 &= I_3\dot{\omega}_3 + (I_2 - I_1)\omega_2\omega_1 \end{aligned} \tag{2.16}$$

where;

I_1, I_2, I_3: Principal moment of inertia

$\dot{\omega}_1, \dot{\omega}_2, \dot{\omega}_3$: Angular accelerations about the principal axes

M_1, M_2, M_3: Component of resultant moment about the principal axes

The centre of mass of a spherical particle whose mass is uniformly distributed throughout its volume and of radius is R, corresponds to the centre of the sphere. Since the three principal moments of inertia are equal to one another and any local-axis system attached to the centre of mass can be referred as principal axis system, Euler's equation of motion can be further simplified and referred as global axis system:

$$M_i = I\dot{\omega}_i = \left(\frac{2}{5}mR^2\right)\dot{\omega}_i \tag{2.17}$$

where;

I: Moment of inertia of spherical particles

M_i: Resultant moment acting on particle

$\dot{\omega}_i$: Angular acceleration of a particle

R: Radius of a spherical particle whose mass is distributed uniformly throughout its volume.

Using the finite difference procedure by invoking a timestep, Δt, the equation of motion (2.14) and (2.17) are integrated. The quantities $\dot{x}_i$ and ω_i are computed at mid-intervals of $t \pm \Delta t/2$. The quantities $x_i, \ddot{x}_i, \dot{\omega}_i, F_i$ and M_i are computed at the primary interval of $t \pm \Delta t$.

The **translational and rotational accelerations** at time t are computed as follows:

$$\ddot{x}_i^{(t)} = \frac{1}{\Delta t}\left(\dot{x}_i^{(t+\frac{\Delta t}{2})} - \dot{x}_i^{(t-\frac{\Delta t}{2})}\right)$$
$$\dot{\omega}_i^{(t)} = \frac{1}{\Delta t}\left(\omega_i^{(t+\frac{\Delta t}{2})} - \omega_i^{(t-\frac{\Delta t}{2})}\right) \tag{2.18}$$

The **translational and rotational velocities** at time $t \pm \Delta t/2$ can be obtained by substituting equation (2.18) into equation (2.14) and (2.17):

$$\dot{x}_i^{(t+\frac{\Delta t}{2})} = \dot{x}_i^{(t-\frac{\Delta t}{2})} + \left[\frac{F_i^{(t)}}{m} + g_i\right]\Delta t \tag{2.19}$$

$$\omega_i^{(t+\frac{\Delta t}{2})} = \omega_i^{(t-\frac{\Delta t}{2})} + \left[\frac{M_i^{(t)}}{I}\right]\Delta t$$

By integrating the velocities in equation (2.19), the position of the particle centre is updated:

$$x_i^{(t+\Delta t)} = x_i^{(t)} + \dot{x}_i^{(t+\frac{\Delta t}{2})}\Delta t \qquad (2.20)$$

1. Given, $\dot{x}_i^{(t-\frac{\Delta t}{2})}, \omega_i^{(t-\frac{\Delta t}{2})}, x_i^{(t)}, F_i^{(t)}$ and $M_i^{(t)}$, Equation (2.19) is used to obtain $\dot{x}_i^{(t+\frac{\Delta t}{2})}$ and $\omega_i^{(t+\frac{\Delta t}{2})}$.
2. $x_i^{(t+\Delta t)}$ is obtained through equation (2.20).
3. Force-displacement law is applied to obtain the values of $F_i^{(t+\Delta t)}$ and $M_i^{(t+\Delta t)}$ for next cycle.

2.4.2.4 Mechanical Time-step

In PFC3D, accelerations and velocities are considered to be constant within each time-step in the time-stepping algorithm. Hence, in order minimize the propagation of disturbance to any particles other than its own immediate neighbour in the calculation cycle; a small timestep needs to be chosen during a single timestep. If the timestep doesn't exceed the critical point, the computed data from equation (2.19) and (2.20) will be stable. At the start of each calculation cycle, PFC3D estimates the critical timestep and actual timestep is taken as a fraction of this estimated critical value.

The critical timestep estimation is computed by considering a one-dimensional mass-spring system described by a point mass (m) and a spring stiffness (k) as illustrated in Figure 5 with a given coordinate system. It should be noted that the motion of the point mass is governed by the differential equation, $-kx = m\ddot{x}$. Bathe and Wilson, (1976) expressed the critical timestep which correspond to a second-order finite-difference scheme as follows:

$$t_{crit} = \frac{T}{\pi}; \qquad T = 2\pi\sqrt{m/k} \qquad (2.21)$$

where;

T: Time Period of the system

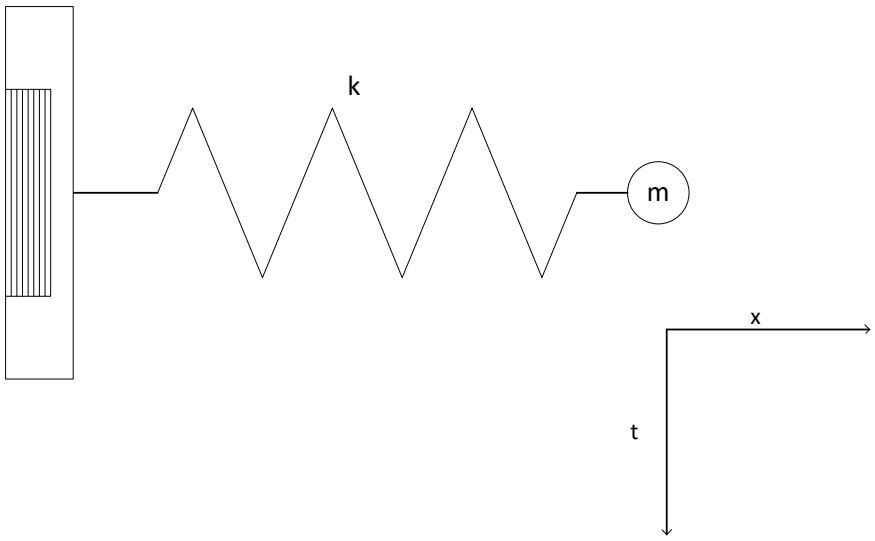

Figure 5: Single mass spring system

Taking into account the infinite series of point masses and spring as illustrated in (Figure 6a), the smallest period will happen when the masses will move in opposite motion synchronically, such that, there is no motion at the centre of each spring. Figure 6b and Figure 6c show how the motion of a single mass can be described by two equivalent systems. Hence, using equation (2.21), the critical timestep can be expressed as:

$$t_{crit} = 2\sqrt{\frac{m}{4k}} = \sqrt{\frac{m}{k}} \tag{2.22}$$

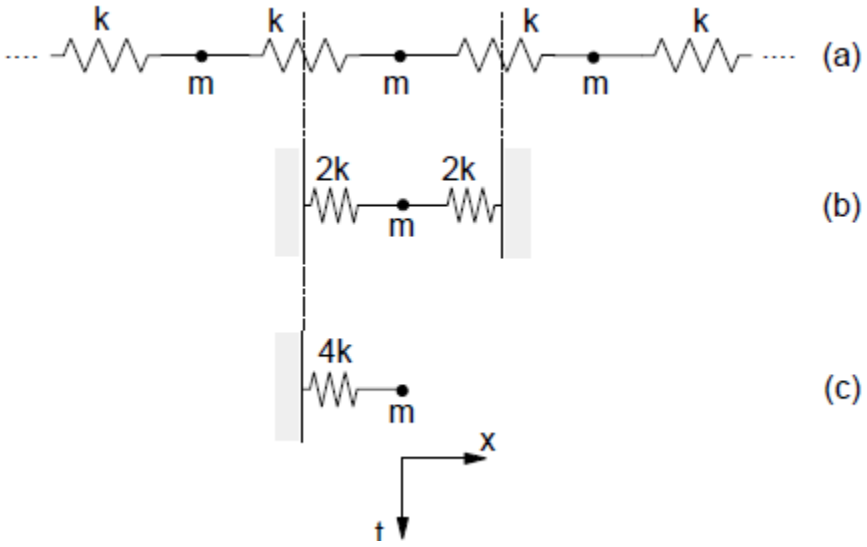

Figure 6: Multiple Mass spring system (Itasca, 2004)

2.4.3 Interaction range

In discrete element modelling, each interaction can be associated with simple constitutive equation in order to reflect or reproduce the macroscopic behaviour of a material for instance concrete. The interaction between two particles or sphere but does not infer that they are in contact is defined by an interaction range, γ (Hentz et al., 2004). Hence, these elements will interact if:

$$\gamma\left(R^a + R^b\right) \geq D^{a,b} \tag{2.23}$$

where;

$D_{a,b}$: Distance between the centroids of elements a and b.

$\gamma \geq 1$

This highlight the main difference from the classical discrete element modelling which uses spherical elements (Cundall and Stack, 1979) where only contact interactions are taken into consideration (Hentz et al., 2004). Hentz et al., (2004) mentioned that the reason that this method was considered is because material other than granular materials, for instance, concrete that involves a matrix, could be simulated. The interaction range, γ is set greater than 1 in order to account for the effect of the matrix between spheres which are cemented together but not in contact. Nevertheless, this long range interaction is limited to the nearest neighbours.

The location of the interaction point is calculated as follows:

$$x^{a,b} = x^a + (R^a - 0.5\left(\left(R^a + R^b\right) - D^{a,b}\right)n \tag{2.24}$$

where;

n: Unit vector pointing from a to b.

x^a: Position vector of element a.

Linked-cell or alternative method (Allen and Tildesley., 1989; Rapaport, 2004) further optimised the short-ranged interaction which makes neighbourhood search more effective. However, it is not possible to use the same method in long range interaction in contrast to short range

interaction; hence more advanced methods are required for optimisation. Luding, (2008) mentioned that for the sake of brevity, neighbouring search was restricted to short range interaction.

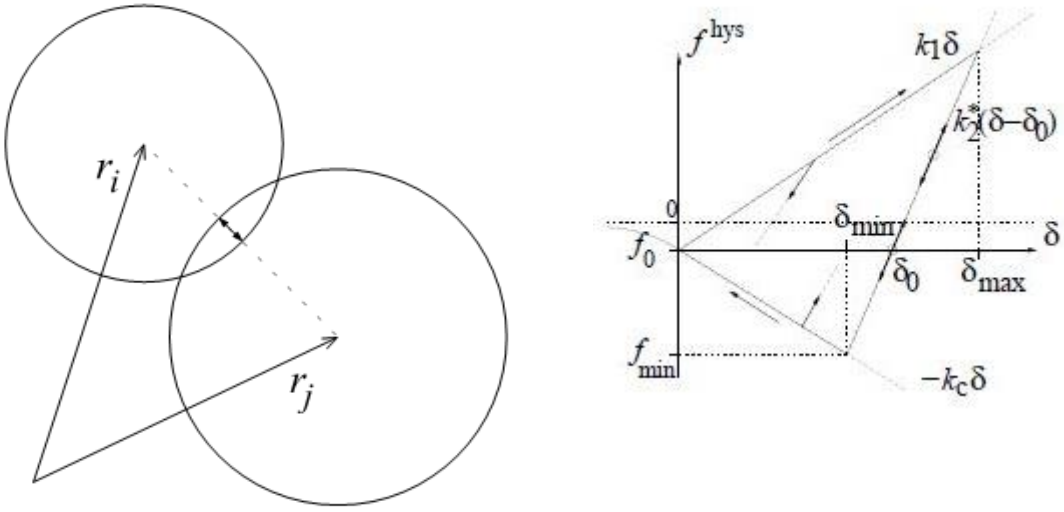

Figure 7: (Left) two particle contact with overlap δ. (Right) schematic graph of the piecewise linear, hysteretic, adhesive force-displacement model (Luding, 2008)

2.4.4 Interaction Forces

The interaction force which caused by the action of element 'a' on element 'b' can be separated into a normal (F^n) and a shear vector (F^s) forces.

$$F = F^n + F^s \tag{2.25}$$

where;

$$F^n = K^n\left(D_{eq}^{a,b} - D^{a,b}\right)n \tag{2.26}$$

$D_{eq}^{a,b}$: Equilibrium distance between two elements a and b when the interaction was created

Hart et al., (1998) computed the shear vector force incrementally and it is stated as follows:

$$\Delta F^s = -K^s \Delta U^s \tag{2.27}$$

where;

ΔU^s: shear displacement vector increment between the locations of the interacting points of the two elements over a timestep, Δt.

2.4.5 Elastic Properties

The strain energy stored in the interaction of particles is not independent of the size of the interacting spheres, as a result, the interaction stiffnesses follows a certain distribution but they are not identical to the sample. The input parameters of the model, for example, the macroscopic elastic properties that are taken into consideration are Young's modulus, E and Poisson's ratio, ν. As such, the local stiffnesses that are needed by the "Macro-micro" relations are deduced from the size of the interacting bodies and the macroscopic elastic properties. Liao et al., (1997) has tried to link the Young's modulus, E and Poisson's ratio, ν to the dimensionless values K^s/K^n by conducting compressive tests with one given sample and fitting relationship as expressed as follows:

$$E = \frac{D_{eq}^{a,b}}{\tilde{A}_{int}} K^n \left(\frac{0.825K^n + 2.65K^s}{2.5K^n + K^s} \right) \tag{2.28}$$

$$\upsilon = \frac{K^n - K^s}{2.5K^n + K^s} \tag{2.29}$$

where;

$\tilde{A}_{int}$: Interaction surface

$$\tilde{A}_{int} = \pi \cdot \min(R^a, R^b)^2 \tag{2.30}$$

2.4.6 Strength Properties

Before rupture (cohesive interaction is broken)

A modified Mohr-Coulomb rupture criterion is used and the maximum tensile strength T (T>0) is given and the maximum normal for F_{max}^{n} is calculated as follows:

$$F_{max}^{n} = -T\tilde{A}_{int} \tag{2.31}$$

The max distance of interaction, D_{max} is calculated as follows:

$$D_{max} = D_{eq} + (\beta + 1)(\frac{|F_{max}^{n}|}{K^{n}} \tag{2.32}$$

where;

D_{eq}: Equilibrium distance

β: softening factor ($\beta > 0$)

Two following cases may occur:

$$F^{n} < F_{max}^{n} \ \ and \ \ D < D_{max} \Rightarrow F^{n} = \frac{K^{n}}{\beta}(D - D_{max}) \tag{2.33}$$

$$F^{n} < F_{max}^{n} \ \ and \ \ D \geq D_{max} \ \Rightarrow \begin{cases} F^{n} = 0 \\ F^{s} = 0 \end{cases} \tag{2.34}$$

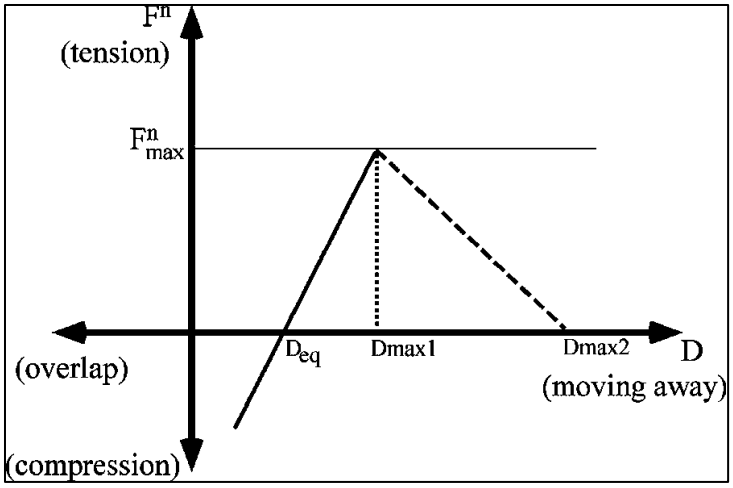

Figure 8: Strength properties of Normal force (Hentz et al, 2004)

The difference between the quasi brittle behaviour that is in the presence of softening (dashed line) and the brittle elastic behaviour is illustrated in Figure 8. Figure 8 illustrates the behaviour of normal force for two different value of β. The normal force is illustrated as the solid line as long as $F^n > F^n_{max}$ but as $F^n < F^n_{max}$; then depending on the value of β, different path could be obtained. For instance,

If β tends to zero, D_{max} tends to D_{max1}; then rupture occurred (dotted line)

If β tends to 2, D_{max} tends to D_{max2} and before rupture; the normal force follows the dashed line.

Moreover, if there is large distribution of radius of the sphere, this may induce a global softening at macroscopic level but however, the local softening factor will incline to zero. According to Herrmann et al. (1989), if there is a large size distribution, there will be a large distribution of maximum normal forces and this will, in turn, induce softening effects. As such one needs to be cautious according to Hentz et al., (2004) before using a local softening factor.

The Max shear force is expressed as follows:

$$F^s_{max} = c\widetilde{A_{int}} + F^n \tan \Phi_i \qquad (2.35)$$

where;

c: cohesion

Φ_i: Internal friction angle

The Absolute value of Shear force is given as follows:

$$|F^s| = (F^s \cdot F^s)^{1/2} \tag{2.36}$$

If the absolute value of shear force is greater than the Max shear force, the shear force is reduced to a limiting value as shown below:

$$F^s_{reduced} = F^s[F^s_{max}/|F^s|] \tag{2.37}$$

After Rupture

Initial interaction is broken and new ones are identified which are merely contact interaction and not cohesive anymore and cannot undergo tension force. The rupture criteria were summarised in Figure 9.

As such, a new max shear force is expressed as follow:

$$F^s_{max} = F^n \tan \Phi_c \tag{2.38}$$

where;

c: Cohesion

Φ_c: contact friction angle which is different from internal friction angle (Φ_i)

The absolute shear force is expressed below:

$$|F^s| = (F^s \cdot F^s)^{1/2} \tag{2.39}$$

If the absolute value of shear force is greater than the Max shear force, the shear force is reduced to a limiting value as shown below:

$$F^s_{reduced} = F^s[F^s_{max}/|F^s|] \tag{2.40}$$

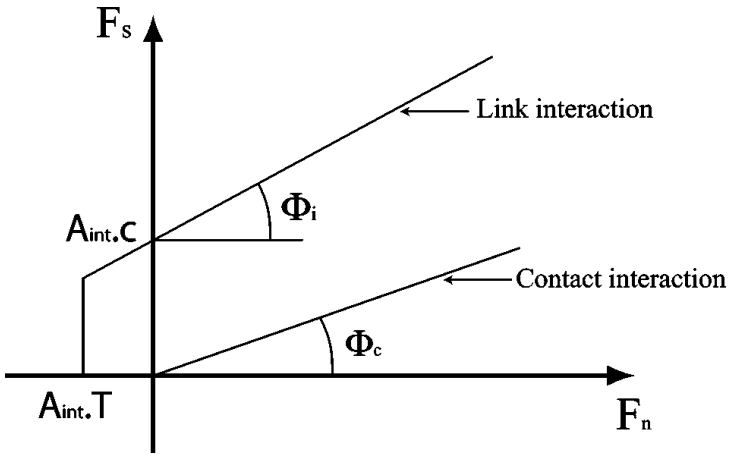

Figure 9: Rupture criteria (Hentz et al., 2004)

2.4.7 Energy Criterion

The Strain energy, E_{sd} is present in the assembly of the discrete element as stated as follows:

$$E_{sd} = \int_{\Omega_d} tr(\sigma_d \cdot \varepsilon_d) d\Omega_d = \sum_{(n,m)} \underline{F}^{n\to m} \cdot (\underline{U}^m - \underline{U}^n) \tag{2.41}$$

$$= \sum_{(n,m)} A^{nm} \cdot \underline{T}^{n\to m} \cdot (\underline{U}^m - \underline{U}^n) \tag{2.42}$$

where;

(n,m): Interaction between n^{th} and the m^{th} element

$\underline{U}^n$: Displacement of n^{th} element

$\underline{F}^{n\to m}$: force applied by n^{th} element on the m^{th} element

A^{nm}: Interaction surface

Hence, according to (Hentz et al., 2004), it appears that strain energy (elastic properties) depends on how the interaction surface is defined. As a result, (Hentz et al., 2004) plotted Young's

modulus versus the total sum of interaction surface in the system assembly as illustrated in Figure 10:

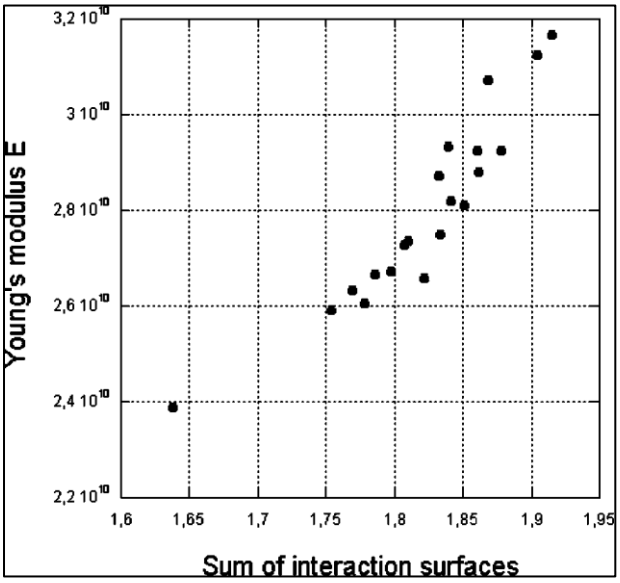

Figure 10: Young's modulus versus sum of interaction surfaces (Hentz et al, 2004)

For each assembly, the ratio of $e=E_{sc}/E_{sd}$ was recorded by Hentz et al., 2004 whereby E_{sd} is the strain energy.

$$e = \frac{E_{sc}}{E_{sd}} = \frac{E}{E_{app}} \cdot \frac{S}{S_{app}} \cdot \frac{l_{app}}{l} \tag{2.43}$$

The computed result obtained from one assembly to another and is not equal to one, as such, Hentz et al., (2004) decided to run the tests with a new interaction surface $A^{nm\prime} = e \cdot A^{nm}$. Hentz et al., (2004) found encouraging result which shows that the dispersion of Young's modulus (respectively of Poisson coefficient) is 12% and standard deviation of the ratio E/Em (respectively v/vm) to be 0.038. In energy criterion, influence of number, size, random aspect of assembly generation and local configuration of elements are reduced.

2.4.8 Contact Constitutive Models

A simple constitutive model of a material simulated in PFC3D comprises of an overall constitutive behaviour at each contact which consists of three parts namely stiffness model, slip model and

bonding model. The elastic relationship between the contact force and relative displacement are established by the stiffness model. In order to the two contacting balls to slip relative to each other, the relationship between the shear and normal contact forces are enforced by the slip model. The bonding model enforces the bond strength limit and thus, restricts the normal and shear force a contact can carry.

Johnson, (1985) differentiates between conforming contact whereby the interactive surface closely fit together preceding deformation and non-conforming contacts whereby the two interactive surfaces that have dissimilar profiles will make contact at only a single point initially. However, the contact between two spheres (disk) in PFC at the interactive surface will be non-conforming that is the contact area will be relatively small in contrast to the particle dimension and stresses are highly concentrated in the contact zone. If the body is distant from the contact area, the stresses are not greatly affected by the geometry of the body in particular. Since most DEM models adopt sphere as particle type; the interactive surface will be non-conforming. Hence, based on one point contact assumption, contact models have been developed. The most commonly used contact models in Geomechanics is namely Hertzian contact model which was developed based on the elastic theory to non-conforming spherical elastic bodies. However, it is more complex to analyse when it comes to the three-dimensional of the real physical contacts. Tavarez et al., (2002) mentioned that there are several scenarios that need to be anticipated and accounted in which clusters can break off by using only normal and tangential springs to model inter-element interactions in the system.

2.4.8.1 Contact-Stiffness Models

Linear elastic spring is the simplest type of contact model that could be used in DEM to simulate load-deformation response where the contact normal force, F_n, and the contact shear force are calculated as respectively:

$$F_n = K_n \delta_n \tag{2.44}$$

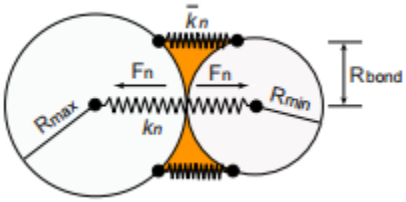

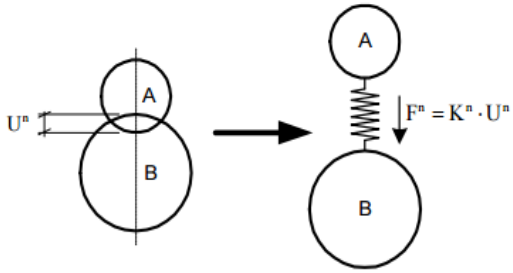

Figure 11: Normal stiffness (Cho el al, 2007)

The normal stiffness is secant stiffness which relates the normal force to the normal displacement.

$$\Delta F_s = -K_s \Delta \delta_s \tag{2.45}$$

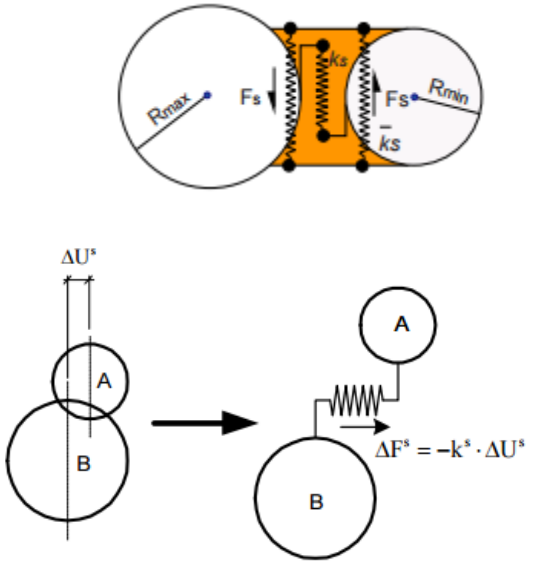

Figure 12: Shear stiffness (Cho el al, 2007)

The shear stiffness is a tangent stiffness since it relates the increment of shear force to the increment of shear displacement.

K_n: contact stiffness in the normal direction.

K_s: contact stiffness in the shear or tangential direction

$\delta_n / \Delta U^n$: The overlap at the contact point measured normal to the contact.

$\delta_s/\Delta U^s$: The overlap at the contact point measured tangential to the contact

2.4.8.1.1 Linear elastic contact springs

The calculated force acts in a normal direction to the contact surface and its orientation is along the line joining the centre of the two-contacting sphere. In Itasca PFC codes, the user choose and agree upon the spring stiffness for each sphere that is if two spheres A and B are in contact; there will two spring stiffness $K_n^{p,A}\ and\ K_n^{p,B}$ in the normal direction and $K_s^{p,A}\ and\ K_s^{p,B}$ in the tangential or shear direction. This results in effective normal stiffness, $K_n^{contact}$ and shear stiffness, $K_s^{contact}$ at the contact point of

$$K_n^{contact} = \frac{k_n^{p,A} K_n^{p,B}}{k_n^{p,A} + K_n^{p,A}} \tag{2.46}$$

$$K_s^{contact} = \frac{k_s^{p,A} k_s^{p,B}}{k_s^{p,A} + k_s^{p,B}} \tag{2.47}$$

Moreover, there is no tension that is transmitted across the particles that are uncemented and unbounded. The contact bond is considered to be ruptured if there is gap developing between particles. In the linear elastic model, the spring should act conceptually as “penalty spring” as the spring constant is not directly related to the solid particles’ properties. Stiff springs are used to minimise the overlapping of particle at the contact point. Besides, in order to match the overall response of the assembly of particles in laboratory, the DEM Model can be calibrated and the stiffness of the contact springs could be adjusted. It was mentioned by Latzel et al., (2000) that the use of a linear contact model is more appropriate for 2D analysis; it is not worth to simulate a 3D material on 2D model because there is a need to simplify the representation which requires tremendous effort. Publications using linear contact model into material response has been achieved by Chen and Ishibashi, (1990), Calvetti et al., (2004) and Rothenburg and Kruyt, (2004).

2.4.8.1.2 Simplified Hertzian contact model

The model has been created to link the spring parameters to the particle material properties in order overcome the non-physical nature of the linear spring stiffness. An expression for the secant contact stiffness using the Hertzian theory of elastic contact could be developed for the

interaction of two particles or sphere. The Hertzian contact model is composed of a set of non-linear contact formulation which is also referred as Hertz-Mindlin model which is an approximate model to describe the tangential force draws upon the work of Mindlin and Deresiewicz, (1953).

The contact normal secant stiffness is expressed by:

$$K_n = \left(\frac{2(G)\sqrt{2R}}{3(1-\nu)}\right)\sqrt{\delta_n} \tag{2.48}$$

The contact shear tangent stiffness is expressed by:

$$K_s = \left(\frac{2\left(\langle G\rangle^2 3(1-\langle\nu\rangle)\check{R}\right)^{1/3}}{2-\langle\upsilon\rangle}\right)|F_i^n|^{1/3} \tag{2.49}$$

Sphere-Sphere contact coefficient:

$$\begin{aligned} R &= \frac{2R_A R_B}{R_A + R_B} \\ G &= \frac{1}{2}\,(G_A + G_B), \qquad (ball\ to\ ball) \\ \upsilon &= \frac{1}{2}(\nu_A + \nu_B) \end{aligned} \tag{2.50}$$

Ball-Wall contact

$$\begin{aligned} \check{R} &= R^{[ball]} \\ \langle G\rangle &= G^{[ball]},\ (ball\ to\ wall) \\ \langle\nu\rangle &= \upsilon^{[ball]} \end{aligned} \tag{2.51}$$

G is the elastic shear modulus, ν is poisson's ratio, R is the sphere radius and the subscripts A and B denote the two spheres in contact. Different researchers for instant Chen and Hung, (1991), Lin and Ng, (1997), Sitaram et al., (2008) and Yimsiri and Soga, (2010) have published DEM simulation based upon this type of contact model.

2.4.8.2 Slip Model

A slip model does not provide normal strength in tension and it allows slip to occur by limiting the shear force. In the absence of a contact bond, this model becomes active whereby the slip model behaviour supersedes the contact bond behaviour. Slip model occurs simultaneously with parallel bond model in the absence contact bond. This is because both contact model and slip model describe the constitutive behaviour of particle contact occurring at a point in contrast to parallel bond model which describes the constitutive behaviour of cementitious material that exists between the two contacting entities. The slip model is defined by the friction coefficient at the contact, μ, where μ, is the minimum friction coefficient between those two contacting balls.

The contact is checked for slip condition by computing the max allowable shear contact force as expressed below:

$$F_{max}^{s} = \mu |F_i^n| \tag{2.52}$$

If $|F_i^s| > F_{max}^s$, then slip is allowed to occur (during the next calculation cycle) by setting the magnitude of F_i^s equal to F_{max}^s via

$$F_i^s \leftarrow F_i^s (F_{max}^s / |F_i^s|) \tag{2.53}$$

2.4.8.3 Bonding Model

PFC comprises of two built-in contacting models which are namely contact-bond and parallel bond. The contact-bond glue is of a vanishingly small size which acts only at the contact point, while parallel-bond glue is of a finite size that acts over a circular cross-section lying between the particles. It is possible for both bonds to be active simultaneously; nevertheless, the slip model is inactive in the presence of contact bond.

2.4.8.3.1 Contact bond model

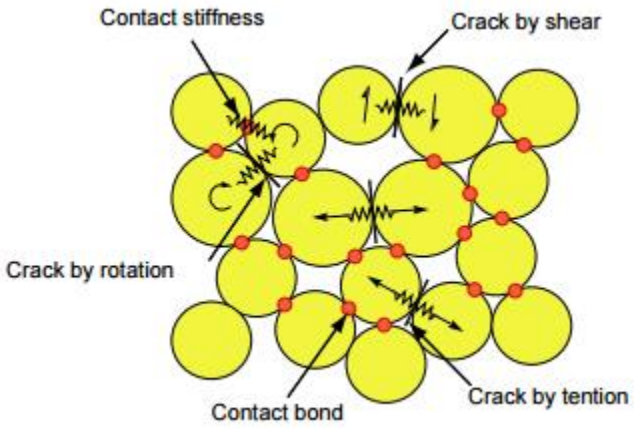

Figure 13: Contact Bond model (Cho el al, 2007)

A contact bond model is visualized as a pair of elastic springs or a point of glue with a constant normal and shear stiffness acting at a point. These two springs have specified shear and tensile normal strength. If the magnitude of the tensile normal contact force and the shear contact force is equal to or exceeds the normal contact bond strength, the bond breaks and the bond revert to unbonded behaviour where slip is possible. In PFC, the particles are free to move in a normal and shear direction and as well as to rotate between particle. However, the moment induces by this moment cannot be resisted by the contact. Besides, after bond breakage, the contact stiffness is active in the contact model as long as the particles are kept in contact. The contact behaviour is illustrated as follows:

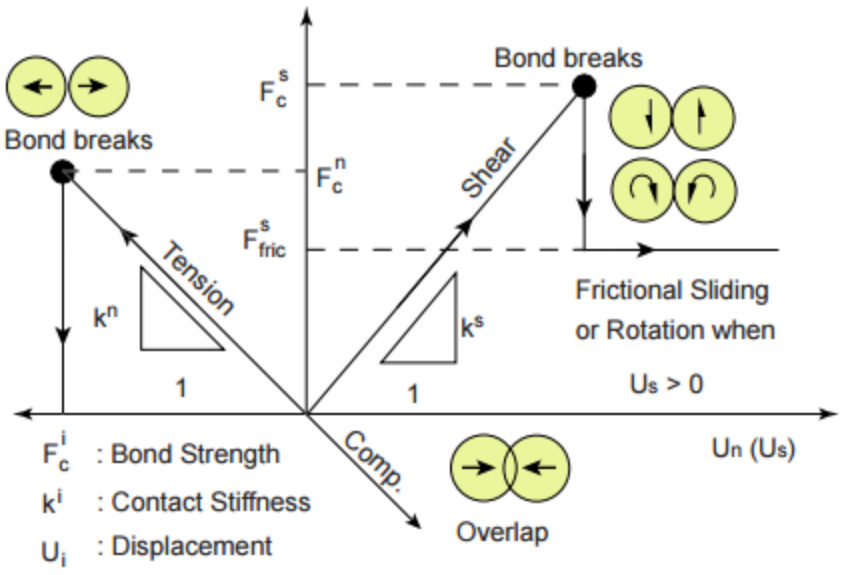

Figure 14: Normal and shear component of contact force (Cho el al, 2007):

2.4.8.3.2 Parallel bond model

A parallel bond model simulates the physical behaviour of a cement-like substance which connects two particles. It establishes an elastic interaction between particles which act in parallel with slip or contact-bond model. It can be imagined as a set of elastic spring distributed uniformly over a rectangular cross-section with a constant normal and shear stiffness centred at contact point and lying on the contact plane as illustrated in Figure 15. Besides, parallel bond assumes that bonding is over a finite area of contact as such, there is a moment which may be induced due to twisting and bending.

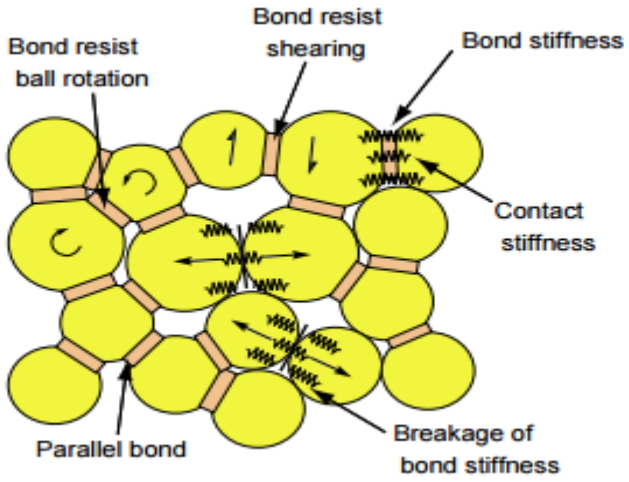

Figure 15: Parallel Bond model (Cho el al, 2007)

From the work of Gutierrez, (2007), the cement at the sphere contacts covers a finite area of sphere surface and has a finite volume according to the scanning electron microscope (SEM) images of the microstructure of cemented sands. Hence, it could be assumed that the strength of the cemented bonds depends on the volume of cement present at the contact. A resistance to rotation and a moment can be transmitted to the normal direction owing to the fine finite area of the cemented bonds. Nevertheless, Potyondy and Cundall, (2004) described that the shortcomings are overcome in parallel bond model and implemented within Itasca's commercially available codes PFC2D and PFC3D.

A pair of parallel linear springs that work in parallel with the no tension contact springs is introduced whenever there is a parallel bond model implemented at each cement contact. As compared to simple bonding model, the moments are transmitted to the particle by both tangential and normal contacts in parallel bond and besides, it has a finite size. A parallel bond radius multiplier, α, is used to specify the bond area so that 0 ≤ α ≤1 and the radius of the bond is, $R_{bond}=\alpha r_{min}$. The bond area (A_{pb}) is given by $A_{pb} = \pi R_{bond}$ for a unit thickness in 2D while in 3D by $A_{pb} = \pi R_{bond}^2$.

The size of the bond represents the amount of cement that is with a larger α value, there is more cement which means that there is a greater degree of bonding. However, the void ratio will be unaffected by the size of the parallel bond. Besides, it is difficult to link the specific α value to the volume of cement and moreover, with the increment of α value, there is an increase in resistance in term of moment and strength. Apart from parameters required for conventional linear contact stiffness model, parallel bond model requires input parameters such as the bond tangential or shear stiffness(K_t^{pb}), the bond shear strength (τ^{max}), the bond stiffness(K_N^{pb}), bond stiffness (K_N^{pb}) and size of the parallel bond, α.

The forces carried by the parallel bond in the normal and tangential directions (F_{pb}^N) and (F_{pb}^t/F_{pb}^s) are given by

$$F_{pb}^N = K_N^{pb} A_{pb} \delta_n \tag{2.54}$$

$$F_{pb}^t = K_t^{pb} A_{pb} \sum \Delta\delta_t \tag{2.55}$$

δ_n: contact normal displacement

$\sum \Delta\delta_t$: Cumulative tangential displacement

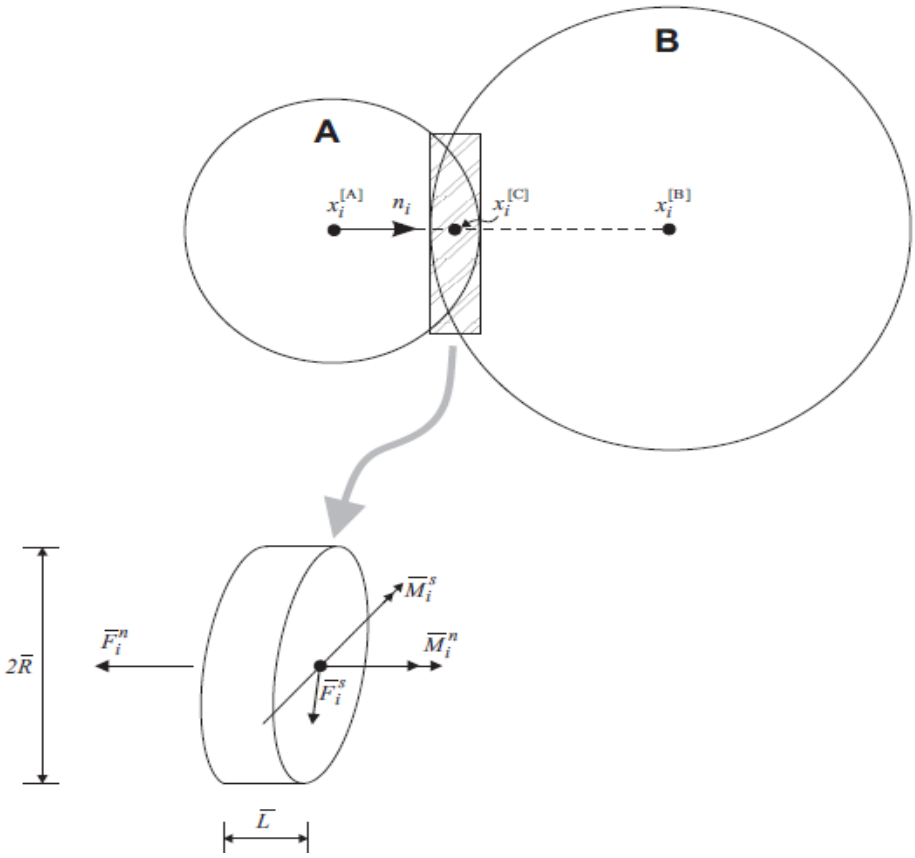

Figure 16: Parallel bond depicted as a cylinder of cementitious material (Itasca, 2004)

The bond breaks when either the maximum tensile or shear stress computed in the bond exceeds the defined strength.

Two types of moments are transmitted by the parallel bond: a spin or twisting moment by parallel bond: a spin or twisting moment (M_{pb}^{spin}) and a bending moment(M_{pb}^{b}). The spin moment can only be calculated in a 3D implementation of this model as it relates to a moment caused by relative rotation about the contact normal. The increments in moments (ΔM_{pb}^{spin} and ΔM_{pb}^{b}) caused by an incremental rotation of the particles are given by:

$$\Delta M_{pb}^{spin} = K_t^{pb} I_{pb} \Delta\theta_n \tag{2.56}$$

$$\Delta M_{pb}^{b} = K_N^{pb} I_{pb} \Delta\theta_s \tag{2.57}$$

I_{pb}: Moment of inertia of parallel bond

$I_{pb} = \frac{2}{3} R_{bond}^3$; for 2D

$I_{pb} = \frac{1}{4} \pi R_{bond}^4$; for 3D

The breakage criteria, i.e the stresses that will cause bond breakage of the normal and tangential parallel bond springs, are defined by the maximum tensile and shear stresses respectively. The expression of the maximum normal stress (σ_N^{max}) and the maximum shear stress (τ^{max}) were derived by consideration of beam bending theory to be:

$$\sigma_N^{max} = \frac{-F_{pb}^N}{A_{pb}} + \frac{\left|M_{pb}^b\right|}{I_{pb}} R_{bond} \tag{2.58}$$

$$\tau^{max} = \frac{\left|-F_{pb}^s\right|}{A_{pb}} R_{bond} + \frac{\left|M_{pb}^{spin}\right|}{J_{pb}} R_{bond} \tag{2.59}$$

J_{pb}: Polar moment of inertia of parallel bond (required only for 3D simulations)

$$J_{pb} = \frac{1}{2} \pi R_{bond}^4 \tag{2.60}$$

Two simple particle analyses were carried by Cheung, (2010) in order to understand the distribution of forces between the contact bond and parallel bond. Parallel bonds take all the tensile force in tensile while in compression the force is shared by both contact model and parallel bond (Cheung, 2010). Moreover, the resultant moment and force acting on the two contacting particles are calculated at each time step. The moment contribution is a function of the relative rotational velocities of the two contacting particles and bond moment of inertia (Itasca, 2004). The relative stiffness and the load share between the particle-particle model and parallel bond model must be taken into consideration in order to capture the brittle response observed in cemented sands (Cheng, 2010). Moreover, this model is available within the commercial DEM code, PFC

2D and has been used to model rock mass or cemented sand response in 2D (Wang et al., 2003 and Fakhimi et al., 2006) and 3D (Potyondy and Cundall, 2004 and Cheung, 2010).

2.4.9 Discrete Fracture Network (DFN)

Discrete fracture network (DFN) is embedded in Particle flow code (PFC) and it is a modelling stochastic approach which explicitly characterised the geometrical properties of each fracture in term of the size, position, shape, aperture or orientation. It also accounts for the topological relationships between fracture set and individual fractures. In other words. A DFN is a collection of fracture and several DFN can coexist in a sample to represent several fracture types or fracture sets. In PFC 3D, fractures are represented as disk-shaped.

In DFN, the fracture size density distribution describes the number of fractures per unit volume, $n(l)$ which size lies within the range of $l \; and \; l + dl$. This relationship is described in a power law distribution below:

$$n(l) = \alpha \cdot l^{-a} \tag{2.61}$$

where;

$n(l)$: Fracture per unit volume

α: Density term of the DFN Model

a: the scaling exponent

The value of α fixes the total fracture density and the total fracture density is dependent on the range of the fracture sizes.

The cumulative fracture size distribution is expressed as follows:

$$C(l) = \int_{l}^{\infty} n(l') \cdot dl' = \alpha \left(\frac{l^{1-a}}{a-1} \right) \tag{2.62}$$

where;

$C(l)$: cumulative fracture size distribution

$n(l)$: Fracture per unit volume

α: Density term of the DFN Model

a: the scaling exponent

2.5 Micro- and Macro-mechanical behaviour of DEM

Constitutive models define the relationship between external excitations and the response of a material. Although the material response of concrete is conventionally described in terms of the macro-scale measurements of stress and strain inferred at the boundaries of elements, better constitutive models also include micro-scale parameters, representing changes in internal structure so that phenomena such as anisotropy, yielding, hardening and softening can be captured by physically meaningful parameters.

Micromechanics are linked with the micro-fields and macro-field. For instance, micro-fields are field variables of microscopic length scale, for example, the dimension of the micro-constituents, say d and macro-fields are field variables of macroscopic length scale, say D, which larger than d. Besides, the relation between macro-fields and micro-field are linked by two recognised theories namely the homogenization theory and the average field theory in a consistent manner. The relationship between the response of the material and the external excitations is defined by the constitutive models. Conventionally, the material response of the soils in term of stress and strain imposed at the boundaries is described in term of macro-scale measurements. Yet, better constitutive models that could represent the changes in internal structure in term of micro-scale parameters could be used in order to capture phenomenon such as hardening, softening, anisotropy and yielding. However, the internal structure could be represented by the grain-size profile, the spatial distribution of grain and voids, material fabric and coordination number of grain

Discrete element method (DEM) is used as an approach toward the microscopic understanding of macroscopic particulate material behaviour (Herrmann, 1997; Kishino, 2001; Hinrichsen and Wolf, 2004). Generally, millions of particles are simulated in a system; as such it is too small to be regarded as macroscopic. Hence, different methods and tools for instance DEM simulation are required to perform a so-called micro-macro transition (Kirkwood et al. 1949; Pöschel and Luding, 2001 and Vermeer et al., 2001). The macroscopic constitutive relationship could be derived from the 'microscopic' simulation of a small sample in order to describe the material within the framework of a macroscopic continuum theory. There are several general expressions which were used to develop the micromechanical-based constitutive model for granular material by relating the macroscopic characteristic such as spin tensor, stress, deformation rate and strain to local data such as particle displacement, contact vector and contact force (Christoffersen and Mehrabadi, 1981; Mehrabadi et al., 1982; Bagi, 1996; Kruyt and Rothenburg, 1996). Although there have been reports of micro-mechanical investigations using DEM (e.g. Rothenburg &

Bathurst), there is little research that focuses on concrete (Hemalatha et al., 2013). Nemat – Nasser (2000) strived to describe the microstructure and kinematic hardening of granular material by developing an inter-testing kinematic model using fabric tensor.

The constituents' properties of concrete do play an important role in determining the properties at macro level. The processes occurring at micro level are used to establish the major properties of concrete such as the durability, strength, fracture, and ductility of concrete. Moreover, other properties such as elastic modulus, creep and micro-hardness could be also studied on cementious composite with a special focus on the difference between micromechanical properties of the interfacial transition zone (ITZ) and those of bulk matrix which are published (Trtik et al., 2000; Ulm et al., 2004). In laboratory, advanced tools such as micro-indentation technique are used to determine the micro level properties (Igarashi, 1996; Zhu and Bartos, 2000; Zhu et al., 2004). The indentation method is used to measure the force required to penetrate a material and this is linked to the hardness of the material depending on the size of indentation or penetration depth. The microscopic studies of complex heterogeneous nature of cementitious material could be conducted with the aid of image analysis, scanning electron microscopy (SEM) and transmission electron microscopy (TEM) (Richardson, 1999; Diamond, 2004) which can shed some light on the randomness of the microstructure at different length scales. Upon averaging the properties acquired at micro level, it provides the homogeneous single value that represents the macro-scale properties of concrete.

Concrete is composed of a matrix and aggregate bonded together at interface at mesoscale. Owing to the effect of segregation and bleeding in its green state of concrete, micro cracks are initiated at interface which in turn weakens the region. Interfacial transition zone (ITZ) is the weakest region where microcracking is initiated and propagated because the modulus of elasticity of the aggregate and matrix are different, hence making ITZ between those two phases, weak (Ortiz, 1988; Opara, 1993). The heterogeneity of cementitious material at different scales increases due to the differences in mechanical properties of various constituents. The fracture behaviour and the global stiffness of the material is influenced by the stiffness and strength of different components. It is possible to determine from the nano-indentation tests the macroscopic behaviour by homogenization of the microscopic response at various phases (Sorelli et al., 2008; Trtik et al., 2009). It is quite difficult to get access specific phases of matrix and aggregate by means of indentation; hence this can be overcome by the use of grid indentation technique (Constantinides and Ulm, 2004). Grid indentation technique is an efficient method to obtain the

quantitative information about mechanical behaviour of cement pastes at the nanoscale (Constantinides, 2003; Constantinides and Ulm, 2004). Skarżyński et al., (2015) mentioned that micro-structure could be simulated directly with meso-scale modelling where the local phenomena such as such as initiation, growth, and formation of localized zone and cracks that affect the macroscopic behaviour could be studied extensively. The optimization and calibration of continuous and discontinuous constitutive model is improved with mesoscopic result which enhances both the strength and ductility of concrete design (Tejchman and Bobinski, 2012, Nitka and Tejchman, 2015). Skarżyński et al., (2015) further added that discrete model may replace experimental tests that involve the study of behaviour of meso-structure of concrete, for instance, aggregate roughness, shape size, and volume; macroporosity and etc. Nevertheless, like most researchers concluded, this involves difficult calibration technique in regard to the geometric and mechanical properties of ITZs and enormous computational cost.

2.5.1 Micro-Macro relationship

In an assembly of discrete particles, the microscopic level is at the contacts as illustrated in Figure 18. Those microscopic quantities are namely, the contact force, the relative displacement and the relative rotation at contacts. Most of the literature show that the local parameters are namely, contact stiffness (normal and tangential), the particles size, internal friction angle and cohesion. They are interrelated with the macroscopic parameters namely Young's modulus and Poisson ratio.

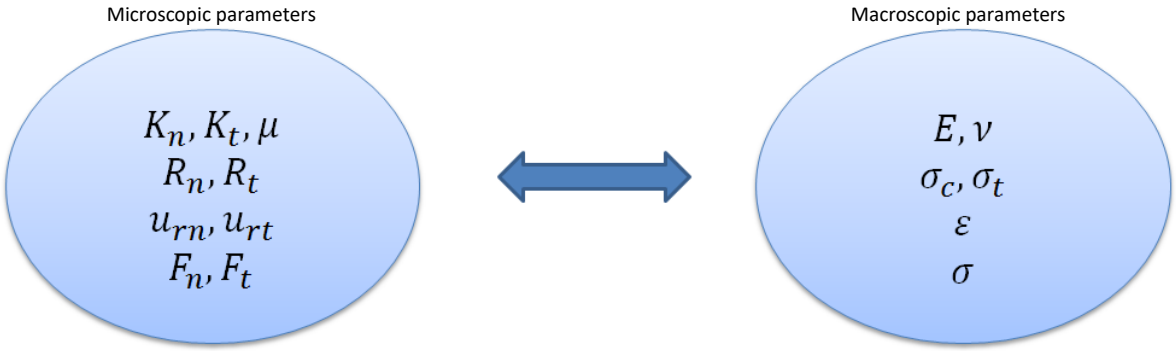

Figure 17: Relationship between microscopic and macroscopic parameter

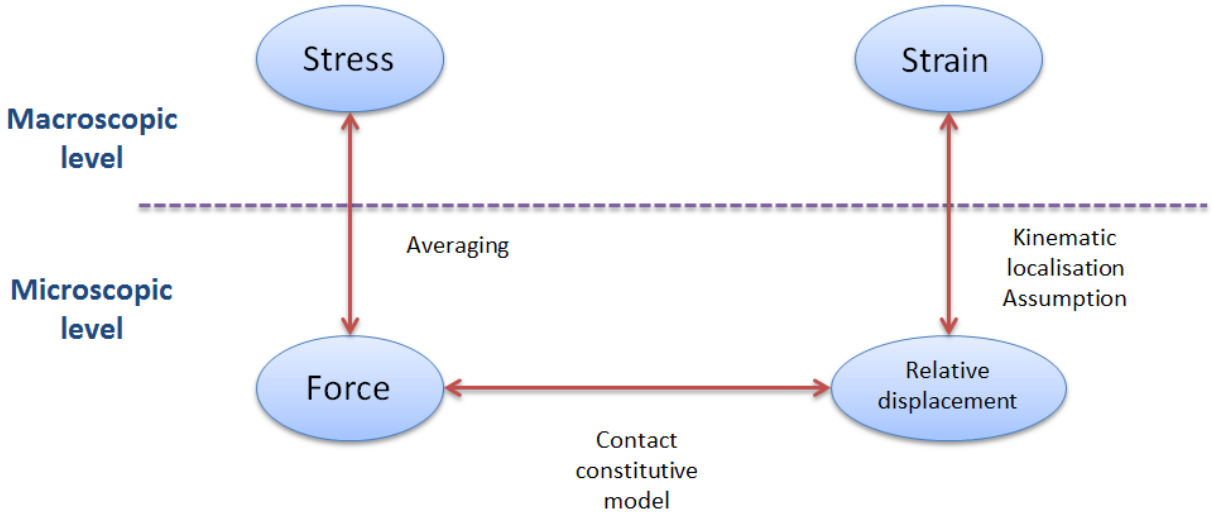

Figure 18: Representation to distinguish between macroscopic level and microscopic level

2.5.2 Calibration of DE Models from Macro parameters to Micro parameter

Based on the work presented by Hentz, (2004) and Rousseau, (2009), the following method based on the contact and cohesive law will be used to calibrate the models.

2.5.2.1 Concrete

Stiffness namely, the normal K_n and the tangential K_s defines the interaction between two spheres. They are related to the macroscopic parameters namely Poisson ratio, ν and Elastic modulus, E. The relationship between the micro and macro parameters is expressed below:

$$E = \frac{D_{eq}}{S_{int}} k_n \frac{\left(\beta + \gamma \frac{k_s}{k_n}\right)}{\left(\alpha + \frac{k_s}{k_n}\right)} \tag{2.63}$$

$$\upsilon = \frac{\left(\beta + \gamma \frac{k_s}{k_n}\right)}{\left(\alpha + \frac{k_s}{k_n}\right)} \tag{2.64}$$

where;

D_{eq}: Initial distance between particles

$S_{inter} = \min(\pi R_a^2, \pi R_b^2)$

α, β, γ: Parameters related to the radius of interaction between particles (Rousseau, 2009)

Based on the work of Rousseau, (2009), the values of the parameter α, β, γ are taken to be:

α: 3.7; β: 2.198 γ: 3.79

There are two parts to be considered upon calibration of the parameter. Firstly, the value of the modulus of elasticity and Poisson's ratio need to be calibrated. Secondly, once these values are determined, the non-linear part of the stress-strain response need to be taken into consideration. In the non-linear part, local parameters to model the macroscopic feature, for instance, compressive strength f_c and tensile strength f_t need to be identified. One assumption made by Camborde, (1882) that contact angle ϕ_c doesn't have a strong effect on the rupture behaviour and can be treated to be equal to frictional angle,ϕ_i.

The following equations define the links breakage between the particles which represents the two local criteria for rupture and it is used to model the non-linear behaviour of concrete:

$$\begin{cases} f_1(F_n, F_s) = F_s - \tan(\phi_i)\, F_n - S_{inter} C_o & Plasticity\ criterion\ (\ sliding\ criterion) \\ f_2(F_n, F_s) = S_{inter} T - F_n & Failure\ Criterion\ (Tensile\ rupture\ Criterion) \end{cases}$$

$$\begin{cases} if\ f_2(F_n, F_s)\ \leq 0 & Cohesive - elastic\ bond \\ if\ f_1(F_n, F_s) \geq 0\ and\ f_2(F_n, F_s) < 0 & F_s \tan(\phi_i)\, F_n - S_{inter} C_o \\ if\ f_2(F_n, F_s) < 0 & Rupture\ (F_s = F_n = 0) \end{cases}$$

where;

C_o: Cohesion factor

T: Local tensile limit

F_n: Normal load

F_s: Tangential load

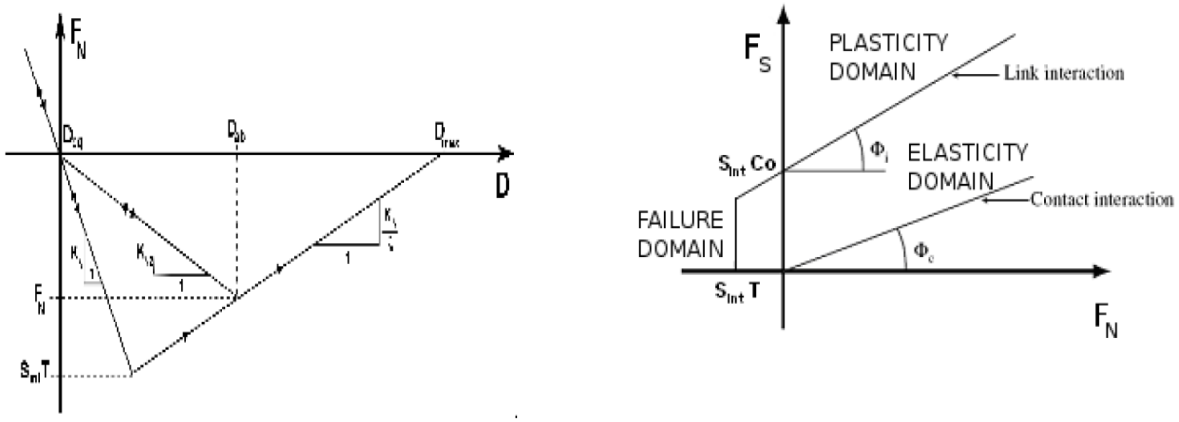

Figure 19: Interaction laws (Hentz et al, 2009)

The interaction between the two spheres follows the laws illustrated in Figure 19. A softening factor ξ is introduced in the law to gradually make then tensile effort tend to zero. A new contact is formed upon the failure of the cohesive link.

2.5.2.2 Steel

Steel is modelled through a representation of group of aligned spheres having the same radius as illustrated in Figure 20. The stiffness between the particles is expressed below:

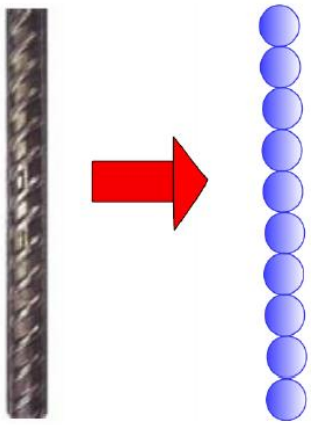

Figure 20: Representation of steel in DEM

$$\begin{cases} K_n = \dfrac{ES_{inter}}{D_{eq}} \\ K_s = \dfrac{ES_{inter}}{(D_{eq}2(1+\nu)} \end{cases} \tag{2.65}$$

where;

S_{inter}: Interaction surface between entities

D_{eq}: Initial distance

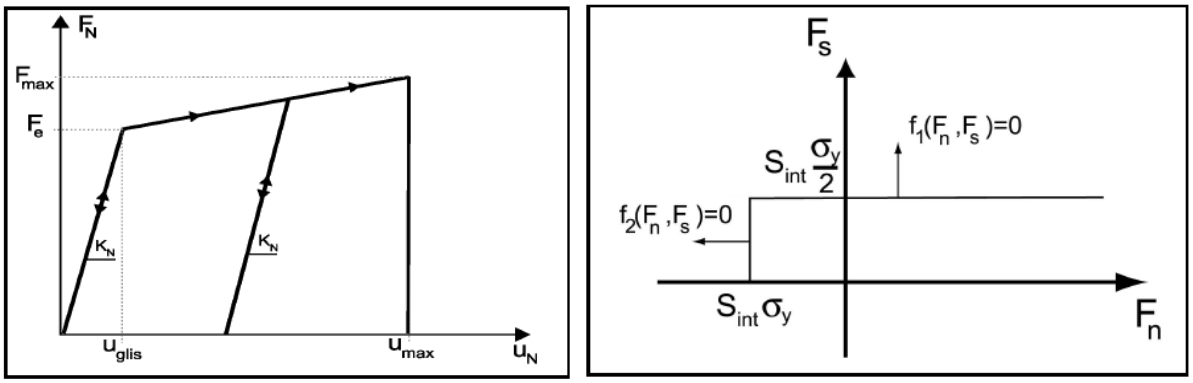

Figure 21: Interaction law for steel

Elastic behaviour

$$F_e = S_{inter} f_e \qquad F_N < F_e$$

Hardening behaviour

$$F_{max} = S_{inter} f_{max} \qquad F_e < F_N < F_{max}$$

2.5.2.3 Steel concrete Interface

Based on the work of Rousseau, (2009), the interaction law between the steel and concrete interface is described in the graph below:

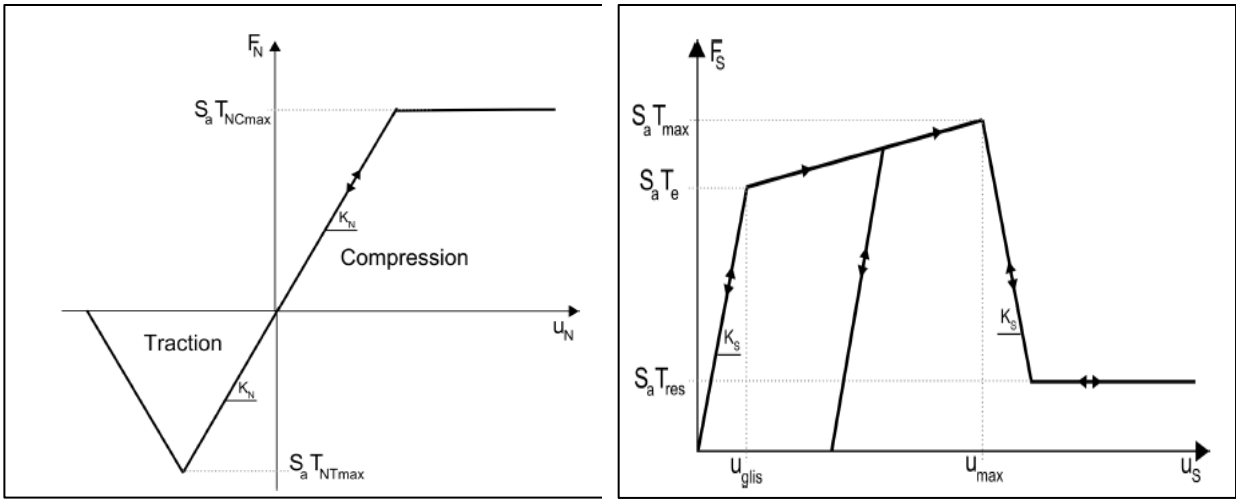

Figure 22: Steel concrete interaction law (Normal and Tangential force)

The graphs in Figure 22 show the interaction law in term of bar displacements for normal and tangential displacement. An elastic phase is always obtained with the normal displacement even beyond the value of S_aT_{NCmax} and S_aT_{NTmax}. Nevertheless, three different phases are identified with tangential displacement namely:

$$\begin{cases} F \leq F_e \text{ , where, } F_e = S_aT_e & (Elastic\ phase) \\ F_e < F \leq F_{max} \text{ where } F_{max} = S_aT_{max} & (Plasticity\ phase) \\ F > F_{res} \text{ where } F_{res} = S_aT_{res} & (friction\ phase) \end{cases}$$

2.5.2.4 Definition of Normal Stiffness, K_n and Shear (Tangential) stiffness, K_s

The stiffness K_n and K_s can be expressed as a function of distance between the sphere, D_{eqNa} and D_{eqSA} of the surface S_a. Both stiffnesses depend on macroscopic parameter, for instance, elastic modulus E and Poisson's ratio ν as expressed below:

$$K_n = \frac{ES_a}{D_{eqNa}} \tag{2.66}$$

$$K_n = \frac{ES_a}{2(1+\nu)D_{eqSA}} \tag{2.67}$$

$$S_a = \frac{4\pi R_a^2}{NB_{ab}} \tag{2.68}$$

where;

S_a: Surface of steel corresponding to the size of the steel element

N_{bAB}: Number of concrete element bonded to it

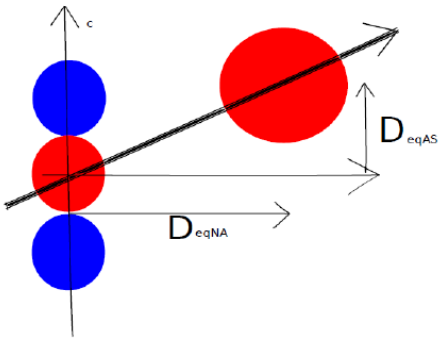

Figure 23: Definition of initial distance

Moreover, Kozicki and Donze, (2008) mentioned that normal stiffness, K_n can be as well computed as a function of elastic modulus of the sphere contact E and the two neighbouring spheres radii R_A and R_B and shear (tangential) stiffness can be computed as a function of elastic modulus and Poisson's ratio ν of the spheres in contact and their corresponding radii R_A and R_B.

$$K_n = E\frac{2R_AR_B}{R_A+R_B} \quad \text{and } K_s = \nu E\frac{2R_AR_B}{R_A+R_B} \tag{2.69}$$

For instance, if two spheres of the same radius (RA=RB=R) are in contact, the stiffness parameters will be equal to $K_n = ER$ and $K_s = \nu ER$. Hence, k_s/k_nwill be equal to ν.

2.6 Theory of fracture mechanics

2.6.1 Cracking in concrete

A crack is termed as a separation by opening or sliding and it is also defined as a discontinuity in the displacement field with a cohesive zone at the tip. Crack can be classified into three classes namely, micro, meso and macro. Micro-cracks are planar discontinuities which are about one to one thousand microns. According to Engelder, (1987), micro-cracks can be subdivided into 'intra-granular cracks' which refers to cracks restricted to one grain, 'grain boundary cracks' which refers to the cracks located at the interface between grains and 'inter-granular cracks' which refers to cracks cutting more grains. Meso-crack is a discontinuity form by a rupture event which spread over a larger number of grains than micro-crack (span approximately one to few millimetres) and subsequently, connects several micro-cracks. However, macro-cracks spans about several millimetres to decimetres and both macro and meso cracks are termed as fracture.

Both Hoagland et al., (1973) and Atkinson, (1987) have described a fracture system to be made of a through-going main separation and the surrounding Fracture Process Zone (FPZ) as illustrated in Figure 24. Figure 24 shows the process zone which comprises of micro-cracks and Meso-cracks which occurs prior fracture. Branching cracks are the cracks that propagate the fracture either through Meso-cracks or macro-cracks. Process zone is defined as an area in front of the fracture tip which is in the state of decohesion where micro-cracks coalesce from the through-going main separation (Broberg, 1999). Besides, the fracture process zone's width relies on the nature of the loading and the grain size (Hoagland et al., 1973; Labuz et al., 1985; Zang et al., 2000; Zhou et al., 2005). Moreover, Hoagland et al., (1973) and Zang et al., (2000) mentioned that the FPZ's size is approximately 5 to 10 times the size of an average grain but Whittaker et al., (1992) has reported values up to 40 time the diameter of a grain size. Figure 25 illustrates the progression of fracture to elucidate the development of micro-, meso- and macro-cracks with the increment in the load applied.

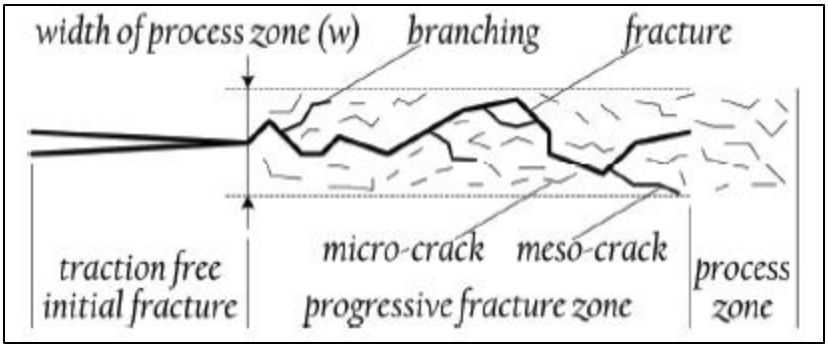

Figure 24: Fracture system (Liu et al., 2000 adapted by Kazerani, 2011)

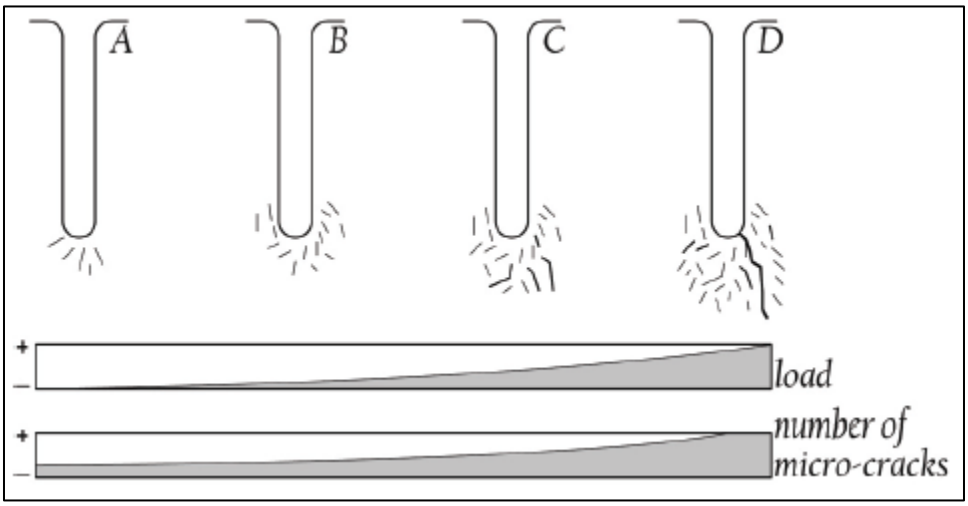

Figure 25: Development of fracture and fracture process zone under tensile load perpendicular to starter notch (Hoagland et al., 1973 adapted by Kazerani, 2011)

2.6.2 Mode of fracturing

Irwin, (1958) mentioned that from a mathematical point of view, cracks or fractures are usually divided into three types namely, Mode-I, Mode-II and Mode-II in fracture mechanics. This division mainly shows the mode of loading, mode of crack propagation or mode of fracturing which is based on the crack tip loading or the crack surface displacement. The mode of loading refers to the applied boundary stresses and the mode of fracturing refers to the mechanical breakdown process which is defined by relative displacement. Rao et al., (2003) mentioned that in most metals, it is appropriate to relate the modes of fracturing to the mode of loading provided the fracture propagates within its own plane. Nevertheless, Kazerani, (2011) mentioned that the mode of loading doesn't relate necessarily to the same mode of fracturing in rock. Likewise, in concrete, the mode of loading doesn't necessarily lead to the same mode of fracturing.

The mode of fracturing that is the crack surface displacement is illustrated in Figure 26. Mode-I is also refered to as tensile mode. The crack tip is subjected to a displacement which is perpendicular to the crack plane and the propagation of the crack is in its plane direction. Thus, there is no shear traction and shear displacement. In Mode-II, the crack propagates perpendicular to the crack front and the crack faces move relatively to each other in the crack plane where shear traction is parallel to the plane of the crack. In Mode-III, the shear displacement is parallel to the front of the crack plane. Moreover, a mixed mode is referred to as those three basic modes combined together. Besides, Atkinson, (1987) mentioned that the principle of superposition could be used in order to describe most cases of crack tip deformation.

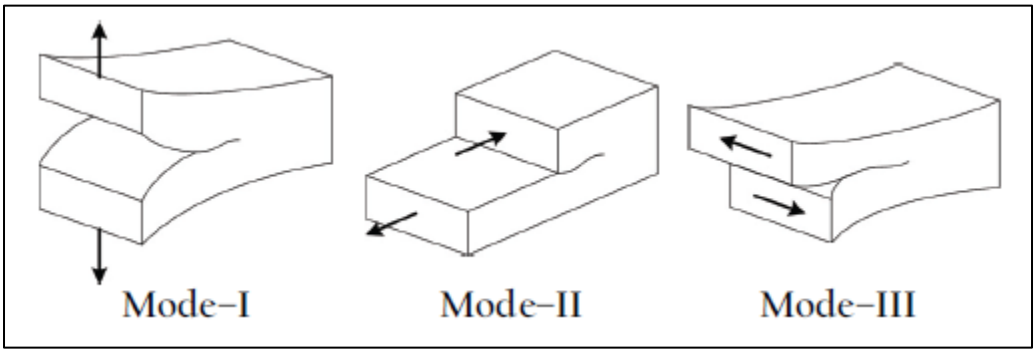

Figure 26: Basic modes of fracturing (Kazerani, (2011))

2.6.3 Stress distribution in the fractured area

Inglis, (1913) proved mathematically that the local stress concentrated at a sharp tip is many times larger than the applied stress. As such, any inhomogeneity or microscopic flaws could be a potential plane of weakness. This stress concentration concept yields are expressed below and this ratio represents the stress concentration factor which depends on the curvature (shape) of the crack.

$$\frac{\sigma_n}{\sigma_f} = \frac{I}{\rho} \tag{2.70}$$

where;

σ_n: Stress at the crack tip

σ_f: Applied stress

ρ: Curvature of the crack tip

Using Westergaard's and Sneddon's stress function, the displacements and stresses at the tip of the existing cracks with a sharp tip, for instance, $\rho \approx 0$ can be computed (Westergaard, 1939, Sneddon, 1946). The stress formulations can be expressed into a simpler form as shown below:

$$\sigma_{ij} = \frac{K_k}{\sqrt{2\pi r}} f_{ij}(\theta) \tag{2.71}$$

where;

σ_{ij}: Stress tensor in the Cartesian coordinates where i and j represent the Cartesian axes

f_{ij}: Geometric stress factor which dependent on angle θ as illustrated in Figure 27

K_k: Multiplier which depends on boundary condition (geometry and loading) where subscript k refers to the corresponding mode

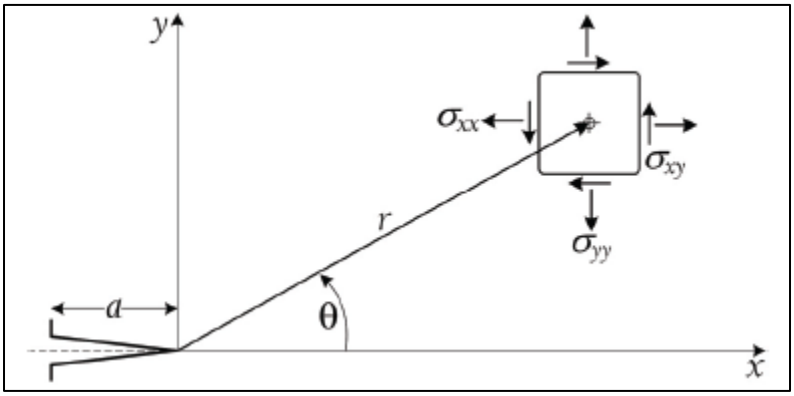

Figure 27: Notation for stress tensor around an edge notch (Kazerani, (2011))

K_k is known as the stress intensity factor in fracture mechanics and it gives the stress concentration at a tip of a notch with given length a and a loading. It is expressed as follows when θ=0,

$$K_k = \sigma_f \sqrt{\pi a} = \sigma_{ij} \sqrt{2\pi r} \tag{2.72}$$

where;

σ_f: Stress

a: Length

Kazerani, (2011) mentioned that it should be noted that this concept is only valid for the case where fracture propagates in its own plan due to corresponding modes of loading. However, any deflection from this plane will result in mixed mode conditions.

2.6.4 Griffith's theory and energy release rate

It is a well-known fact that most materials will yield if the stressed beyond their critical limit. Hence, if the stress intensity factor reaches the critical value which is often referred as fracture toughness, K_{kc}, crack initiation will occur. Griffith, (1921) strives to explain this phenomenon from an energy point of view. As such, he formulated a criterion for the extension of an isolated crack within elastic solids through the introduction of energy theorem of thermodynamic and classical mechanics by modelling crack as a reversible thermodynamic system. The energy-balance concept proposed by Griffith, (1921) is given as follows:

$$\frac{d\Psi}{dr} = 0 \tag{2.73}$$

where;

$d\Psi$: Change in the system energy

dr: Crack extension

Nevertheless, if the equilibrium is not maintained, in regard to whether $\frac{d\Psi}{dr}$ is negative or positive, the crack will extend or retract reversibly.

Griffith's strength relation which defines the failure load is expressed as follow:

$$\sigma_u = \sqrt{\frac{2E'\gamma}{\pi a}} \tag{2.74}$$

where;

$E' = E$ (Plane-stress)

$E' = E/(1 - v^2)$ (Plane-strain)

E: Young's modulus

v: Poisson ratio

γ: crack surface energy

The crack remains stationary if the applied boundary stress, σ_f is lower than σ_u and it starts to propagate unless σ_u is exceeded. Hence, Griffith expressed this idea in term of energy concept tell us that crack extension will occur if the energy release rate, G exceeds the critical energy release rate, G_f.

Hence, rearranging Griffith's strength relation, the following expression is obtained:

$$G_f = 2\gamma = \frac{\pi a \sigma_u^2}{E'} \tag{2.75}$$

Irwin, (1958) mentioned about the equivalence of the stress intensity factor and energy release rate $\left(K_k = K_{kc} \leftrightarrow G = G_f\right)$. As such, the critical energy release rate and the fracture toughness can be linked together. For instance, if $\sigma_f = \sigma_u$ in Mode-I, Equation (2.72) is expressed as follows:

$$K_{IC} = \sigma_u \sqrt{\pi a} \tag{2.76}$$

Merging equation (2.75) and (2.76), the following expression is obtained:

$$G_f = \frac{K_{IC}^2}{E'} \tag{2.77}$$

Applying principle of superposition to this relationship leads:

$$G_f = \frac{K_{IC}^2}{E'} + \frac{K_{IIC}^2}{E'} + \frac{K_{IIIC}^2}{E'}\ (1 + \nu) \tag{2.78}$$

2.6.5 Fracture mechanic in concrete

A significant amount of research has been conducted recently in the area of fracture behaviour of solids, for instance, concrete and rock under impact loading in recent years (Tavarez et al, 2002). For instance, continuum-based methods like finite element method are quite challenging to be applied to concrete which is complex and extremely heterogeneous in nature and loss of the mass due to the erosion of the material may alter the solution for the problem (Tavarez et al, 2002). Fracture is a phenomenon that occurs in concrete material in particular (Bazant and Planas, 1997, Lilliu and Van Mier, 2003, Tejchman and Bobinski, 2012) and it can be really complex to analyse because it consists of main crack which divides into sub-branch, secondary cracks and micro-

cracks (Bazant and Planas, 1997). Micro-cracks arise in the hardening region during fracture on the stress-strain curve and during the material softening, these micro-cracks evolves into dominant distinct macroscopic cracks up to failure. The understanding of fracture is essential because it involves the safety of structure and material behaviour. Nevertheless, the micro-structure of the material has to be taken into consideration since its effects is spread globally on the structure (Tejchman and Bobinski, 2012). Concrete at meso-scale is composed of 4 phases: aggregate, cement matrix macro-voids and interfacial transition zone (ITZs) (Lilliu and Van Mier, 2003, Gitman et al. 2008, Skarzynski and Tejchman, 2010, Beasman and McCuen, 2011 and Skarzynski and Tejchman, 2013).

Moreover, one of the biggest challenges which engineers face when modelling a structure such as beams, plates and shells is the complexity of non-linear behaviour of those structure. This non-linearity is mainly due to material factors such as cracking of concrete, bond-slip interaction between concrete, aggregate interlock of cracked concrete or reinforcement, concrete creep and shrinkage and amongst others. The nonlinear response of concrete is observed through its well-known strain softening response. Despite the fact that, there is great progress in developing numerical model, yet, so far in a recent view, only minor cracking problem with simple geometries have been solved (ACI Report, 1997). ACI Report, 1997 mentioned that in order, to understand the energy dissipation during cracking, the fracture process zone (FPZ) must be modelled properly. Hence, models such a smeared crack model and discrete crack model based on non-linear fracture mechanics should be used rather than linear elastic fracture mechanics as they can predict the crack trajectories and load-displacement responses (Yang and Proverbs, 2003). Nevertheless, due to lack of computational power, both models have been used less frequently to model multiple distributed crack propagation (Abdollahi, 1996, Abdollahi, 1996, ACI Report, 1997). It can be noted according to Yann and Chen, 2005 that discrete crack models have an advantage over smeared model because it can capture details such as crack width, crack spacing and crack path.

There are two different types of failure that occurs for interfacial transition zone (ITZ). They are namely the ITZ-aggregate separation which is related to delamination process and the ITZ-failure which is associated with cracking. Since ITZ is the weakest region in concrete, it is necessary to understand the behaviour and properties of ITZ in order to locate the damage while performing a meso-scale analysis. The behaviour of concrete at meso-scale could be described using continuum finite element (FE) model (Gitman et al., 2008, Skarzynski and Tejchman, 2010, Kim and Al-rub, 2011, Shahbeyk et al., 2011 and Yin et al., 2012) and discrete models (Lilliu and Van

Mier, 2003; Hentz et al., 2004; Kozicki and Tejchman, 2008). The most popular discrete methods used are Lattice method (Lilliu and Van Mier, 2003; Kozicki and Tejchman, 2008; Herrmann et al.1989; Jirasek and Bazant, 1995; Schlangen and Garboczi, 1997; Cusatis and Bazant, 2003 and Bolander and Sukumar, 2005), Classical discrete model (Lilliu and Van Mier, 2003, Hentz et al., 2004 and, Kozicki and Tejchman, 2008) and interface element models with constitutive laws based on non-linear fracture mechanics (Carol et al, 2001 and Caballero et al., 2006).

The concept of cohesive zone trailing proposed by Hillerborg has become popular during past decade (Cedolin et al., 1983, Reinhart et al., 1986, Wecharatana and Shah, 1986, Du et al., 1989) and it is used to model the growing crack in concrete fracture specimen (Hillerborg et al., 1976) to better understand the behaviour of the concrete specimen. Cohesive zone concept is based on postulated fracture process zone (FPZ) which is originated from the idealization of plastic zone that precede the crack tip in a ductile metal where micro cracks form and merge to form a growing traction-free macro crack. A postulated fracture process zone is a region where micro cracks are formed and merged to form a traction-free macro crack. Nevertheless, further studies relate cohesive zone to fracture surface where aggregate bridge the concrete fracture and the grain connecting the fracture of monolithic ceramic in order to inhibit crack. In mode I fracture, the cyclic load and unload test in the strain-softening region of direct tension test provide a resistance that described in term of a crack closure stress (CCS) versus crack opening displacement (COD) relationship (Reinhart et al., 1986, Wecharatana and Shah, 1986). Upon the implementation of the relationship of CCS versus COD in finite element model, it can be used to simulate damage process progressively and also, the overall fracture strength (Du et al., 1989). In most of the studies conducted, an inverse analysis of a postulated CCS versus COD relationship is varied until the measured loading parameters and computed one such load-line displacement and applied load overlapped (Hillerborg et al., 1976, Cedolin et al., 1983 and Reinhart et al., 1986). The direct measurements of crack tip parameters in experiment are limited since it difficult to measure the COD in the vicinity of the crack tip (Cedolin et al., 1983, Miller et al., (1988) and Du et al., 1989) and the CCS cannot be directly measured.

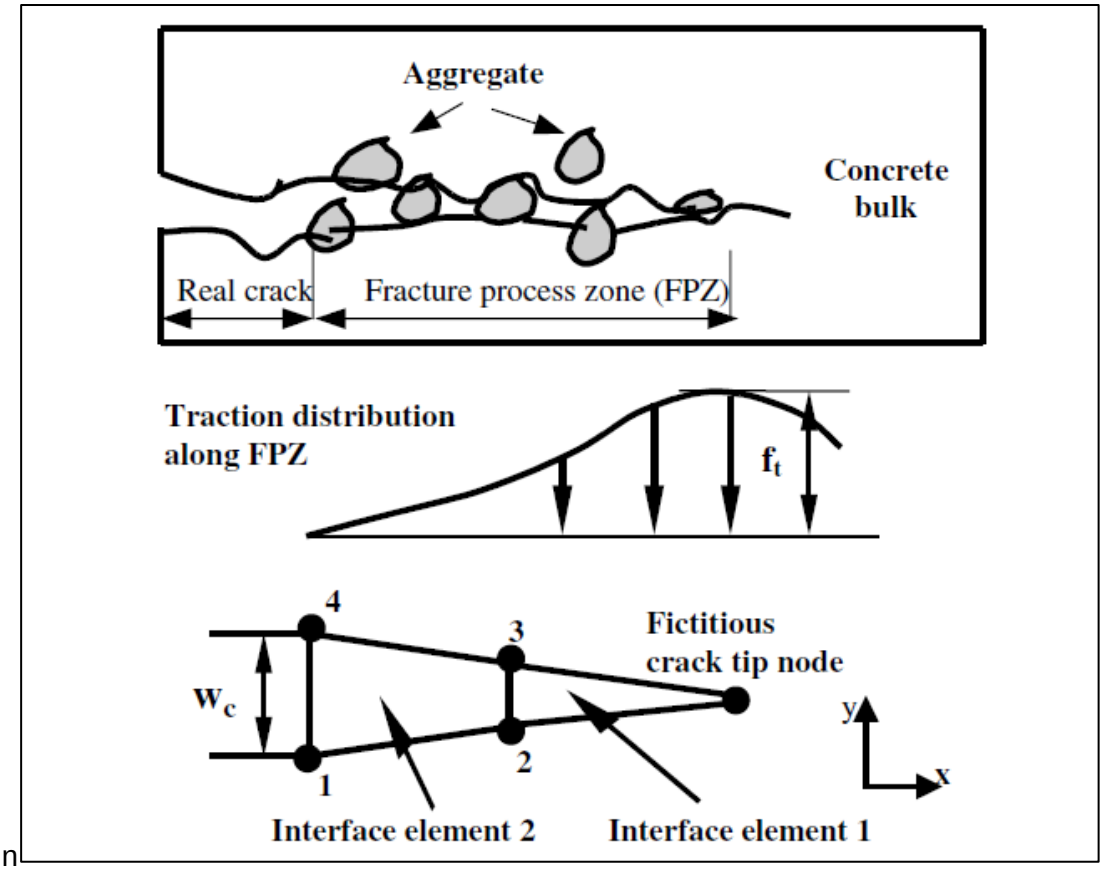

n

Figure 28: Modelling of FPZ with four node interface element (Xie, 1995)

Experimental data show that it is not possible for mixed mode crack extension to form in brittle polymers and metals (Chang.Te et al., 1993). It is possible that the interlocking forces and aggregate bridging in concrete which act on the crack surfaces trailing the crack tip to influence the dominant mode I crack tip state of stress resulting in mixed mode crack extension. The diagonal tension failure is the most common mixed mode type of fracture that occurs in reinforced concrete beam and it induces flexural cracks which are generated by fracture along the tension edge of the beam. The crack propagates initially perpendicularly from the edge of the beam which increases in depth depending on the applied moments and then the cracks kink further extends beyond the reinforcement. The resultant interfacial crack closing and shearing force due to the interlocking and aggregate bridging can influence the crack extension together with kinking angle.

2.6.6 Fracture Process Zone (FPZ)

The mechanisms of fracture toughening of concrete consist of two zones namely the trailing process zone and the frontal process zone. In front of the progressing crack, there is an irreversible energy dissipation that includes multiple micro cracking and crack deflection which occurs in concrete. The zone behind the crack tip whereby there is a force that is transferred by the crack bridging mechanism and aggregate interlocking is called the trailing process zone. Fracture process zone is modelled with the constitutive relationship between the crack opening displacement and the crack closure stress. The behaviour of fracture in concrete in extremely non-linear (Hsu et al., 1963) which is due to the growth of the debonding between cement and aggregates and the propagation of cracking with the matrix. Nevertheless, there is existing microcracks in concrete well before the load is applied because of dry shrinkage of hardened concrete and hydration process.

The load-displacement of a three-point bending test of concrete is shown below in Figure 29. It is difficult to obtain a proper stress-deformation relationship from a direct tension test. This is due because the measured average deformation of the tensile specimen is insignificant in the presence of the localized fracture zone. As illustrated in Figure 29, in contrast to a linear elastic fracture mechanics (LEFM), after reaching the peak load, the load curve drops smoothly. This phenomenon of this non-linear behaviour is referred to as strain softening in contrast to the strain hardening in metal as illustrated in Figure 29. In fact, this term softening could be a misnomer because it is this mechanism which provides toughening to the fracture resistance of the material.

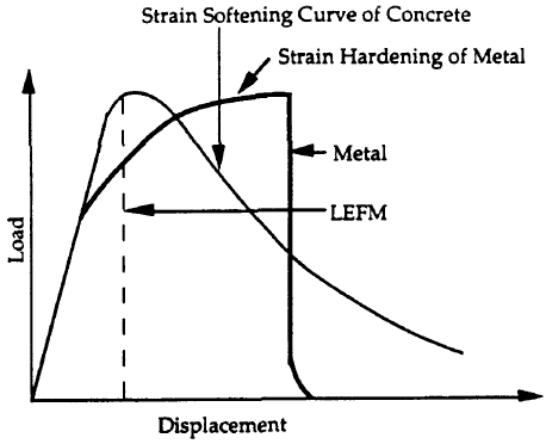

Figure 29: Comparison of the Load-Displacement Curves for a Strain Softening Concrete (fine line), Metal (thicker line, and LEFM (Dashline)

Based on an experimental study of fracture of concrete, Kaplan, (1961) found that the extension force was 12 time larger than that estimated from the surface energy and he recognized this variance of the crack extension force is due to slow the growth of crack before fracture. Moreover, owing to the extension of the work of Kaplan; Glucklick, (1963) attributed the larger magnitude of crack extension force in contrast than that estimated from the surface energy to the fact that concrete fracture is not limited to single crack propagation. In fact, the true fracture surface area was much greater than the actual one due to the fact that a multitude of microcrack was formed in the highly stresses zone. Aggregate acts as crack arrestors in concrete (Glucklick, 1963) because divert the crack under higher energy and increased the energy demand. The slope of fracture energy versus crack length increases until a critical crack length is reached and this shows that the microcracking process zone is fully developed before the unstate crack propagation occurs.

2.7 Microscopic parameters

2.7.1 Coordination number

The coordination number quantifies the number of contacts per particle in the material and it also gives a measure of the packing density at particle scale. Coordination number, Z is expressed as:

$$Z = 2\frac{N_c}{N_p} \tag{2.79}$$

where;

N_c: Total number of contacts
N_p: Number of particles

Moreover, since the contact is shared by two particles, as a result, the number of contacts is multiplied by 2. It is interesting to note that the notation for coordination number varies according to researchers, for instance, Rothenburg and Kruyt, (2004) uses the symbol Γ whereas Thornton, (2000) uses Z as the symbol for coordination number. Coordination number can be determined easily from DEM simulation data and it is the most basic particle-scale measure of material structure. Besides, in the calculation of coordination number, only the engaged contacts are considered not the potential contacts and not transmitting inter-particle force. There are modified

and refined definitions of coordination number that exist, for instance, Thornton, (2000) defined a mechanical coordination number Z_m as follows:

$$Z_m = 2\frac{N_c - N_p^1}{N_p - (N_p^1 + N_p^0)} \tag{2.80}$$

N_p^1: Number of particles with one contact

N_p^0: Number of particles with no contact

The critical mechanical coordination number reflects an underlying stability requirement and corresponds, in statistical physics terminology, to a percolation threshold. Thornton, (1994) showed that local instability occurs if there is a drop of the mechanical coordination below the critical value which results in the formation of shear bands and strain localization in the presences of boundaries.

2.7.2 Stress tensor

Bardet, (1998) mentioned that stress calculation in a discrete element system is well profound. The average stress tensor could be acquired by the following formula below (Love, 1927; Weber, 1966; Christoffersen et al., 1981 and Cambou et al., 1995).

$$\bar{\bar{\sigma}} = \frac{1}{V}\sum_{c} \underline{F}^{(c)} \otimes \underline{l}^{(c)} \tag{2.81}$$

where;

$\underline{l}^{(c)}$: vector relating the centre of the two particles which are in contact at contact (c)

$\underline{F}^{(c)}$: Vector contact forces in (c) where the sum covers all the contacts in the volume (V)

This relationship was first proposed by love, (1927) and later on, many authors proved this relationship in many ways, for instance, Thornton and Barnes, (1986) proposed a relationship which was adopted by PFC 2D, (1997).

The average stress tensor for the volume V^p occupied by a single particle could be expressed as:

$$\bar{\sigma}_{ij}^{p} = \frac{1}{V^{(p)}} \int_{V^{(p)}} \sigma_{ij}^{(p)} dV^{p} \tag{2.82}$$

By applying Gauss theorem integral:

$$\bar{\sigma}_{ij}^{p} = \frac{1}{V^{(p)}} \int_{V^{(p)}} x_i t_i{}^{(p)} dV^{p} \text{ (2.2)} \tag{2.83}$$

If we consider the tractions to consist solely of discrete forces acting at discrete contact point contacts defined by the coordinates (referenced to the particle centre) then the Gauss theorem integral in Equation 2.83 may be replaced by a summation over the contacts for the particles:

$$\bar{\sigma}_{ij}^{p} = -\frac{1}{V^{(p)}} \sum_{N_c} x_i^{(c)} F_j^{(c)} \tag{2.84}$$

The minus sign is introduced for convention purpose that is compressive forces produces negative average stresses and tensile forces produce positive average stresses.

The average stress tensor in a volume V containing a large assembly of particles is expressed as:

$$\overline{\sigma_{ij}} = \frac{1}{V} \int_{V} \sigma_{ij}\, dV \tag{2.85}$$

The integral can be substituted by a summation over the N_p particle contained within volume, V since σ_{ij}=0.

$$\bar{\sigma}_{ij} = \frac{1}{V} \sum_{N_p} \bar{\sigma}_{ij}^{(p)} V^{(p)} \tag{2.86}$$

Substituting (2.84) into (2.86) we define the macroscopic stress tensor as:

$$\bar{\sigma}_{ij} = -\frac{1}{V}\sum_{N_p}\sum_{N_c} x_i^{(c)} F_j^{(c)} \tag{2.87}$$

A correction factor is introduced in the computation of the average stress tensor since the measurement are conducted in circles and only the particles with centroid within the field of measurement are taken into consideration. Hence, the correction factor will cater for the neglected additional area. As a result, the following equation which represents the assembly of a large and finite number of particles in equilibrium:

$$\bar{\sigma}_{ij} = 1\left[\frac{1-n}{\sum_{N_p} V^{(p)}}\right]\sum_{N_p}\sum_{N_c}\left|x_i^{(c)} - x_i^{(p)}\right| n_i^{(c,p)} F_j^{(c)} \tag{2.88}$$

The summations are taken over $N_p$discs with centroids contained within the measurement circle in the specimen and over the $N_c$contacts between discs.

$\bar{\sigma}_{ij}$: Average stress components

n: Porosity within the measurement circle

$V^{(p)}$: Volume of particle (p*)*, taken to be equal to the area of particle (p*)* times a unit-thickness;

$x_i^{(p)}$ and $x_i^{(c)}$: are the locations of a particle centroid and its point of contact, respectively;

$n_i^{(c,p)}$: Unit normal vector directed from a particle centroid to its contact location;

$F_j^{(c)}$: force acting at contact (*c*)

Bathurst and Rothenburg, (1988) mentioned that equation (2.88) is a good approximation for stress tensor and it can be used in continuum mechanic for granular assemblies comprising of a large and finite number of particles in a circular area.

Moreover, there are other definitions and forms of average stress tensor that were derived by Rothenburg, (1982), Christoffersen et al., (1981), Rothenburg and Selvadurai, (1981), Mehrabadi et al., (1982), Cundall and Strack, (1983), Thornton and Barnes, (1986b), Rothenburg and Bathurst, (1989), Bagi, (1996) and Kruyt and Rothenburg, (1996).

2.7.3 Strain tensor

Catherine et al., (2003) mentioned that the calculation of stress tensor in a discrete system is well defined; however, that's not the case for stain tensor. Ammeri et al., (2009) mentioned that in order to define strain tensor, many methods were developed to link DEM and continuum medium approaches. These methods can be classified into two group namely kinematic homogenization methods and energy-based method.

Kinematic homogenization methods are based on spatial discretization that involves the use of nodal displacement field's interpolation functions, which based on the sphere centroidal coordinates, a graph or a nodal network method is constructed. With the assumption that there is a linear variation of displacement values between adjacent nodes and considering the relative increment of displacement along each edge of the graph, the incremental displacement gradient is calculated. However, problems that involve strain localizations cannot be analysed using the spatial discretization approaches because these interpolation techniques cannot account for the particle rotation except some methods proposed by Liao et al., (1997) and Dedecker et al., (2000). According to Calvetti et al., (1997), the second method that is an energy-based method, the strain energy in the equivalent continuum is equated to the energy stored in the contacts of discrete elements and Ammeri et al., (2009) mentioned these approaches seems to yield inaccurate estimation of strain. Nevertheless, Ammeri et al., (2009) have adopted the best-fit approach proposed by Liao et al., (1997) to define local strain and it is based on the translation of individual sphere, u_i^p.

The predictable translation of particles assuming that they all would translate in respect to a deformation gradient tensor α_{ij} is expressed as follows:

$$\bar{u}_i^{(p)} = \alpha_{ij} x_j^{(p)} \tag{2.89}$$

where;

$\bar{u}_i^{(p)}$: Translation of individual particle

$x_j^{(p)}$: Difference of the particle position from the average position of all particles present in the measurement circle

This predicted value measurement is expressed below:

$$e = u_i^{(p)} - \bar{u}_i^{(p)} \tag{2.90}$$

Then the α_{ij} that makes the square-sum of these errors the least is calculated as follows:

$$F(\alpha_{ij}) = \sum_{N_p} \left| u_i^{(p)} - \alpha_{ij} x_j^{(p)} \right|^2 \tag{2.91}$$

The condition of the minimum error can be written as:

$$\frac{\delta F}{\delta \alpha_{ij}} = 0 \tag{2.92}$$

Substitute equation (2.91) into (2.92)and differentiate the optimum α_{ij} is obtained as follows:

$$\begin{bmatrix} \sum_{N_p} x_1^{(p)} x_1^{(p)} & \sum_{N_p} x_2^{(p)} x_1^{(p)} \\ \sum_{N_p} x_1^{(p)} x_2^{(p)} & \sum_{N_p} x_2^{(p)} x_2^{(p)} \end{bmatrix} \begin{Bmatrix} \alpha_{i1} \\ \alpha_{i2} \end{Bmatrix} = \begin{Bmatrix} \sum_{N_p} u_i^{(p)} x_1^{(p)} \\ \sum_{N_p} u_i^{(p)} x_2^{(p)} \end{Bmatrix}, i = 1,2 \tag{2.93}$$

These four equations have to be solved by performing a single LU-decomposition and the average strain which corresponds to the symmetric part of α_{ij} can be obtained.

Fracture mechanism can be established with the measurement of the crack evolution under loading of a particular test specimen. It comprises and can be distinguished in two stages namely visualization and quantification. The first stage is not that straightforward and it is rather demanding when it comes to heterogeneous materials where it is difficult to distinguish cracks from grain boundaries and interfaces which are at submicron scale. It is commonly seen that crack at mm-scale opening particularly in high-performance fibre-reinforced cement-based composites is often accompanied by many µm-scale micro-cracks. Hence, it is essential to combine a large field of view with a very high resolution. Besides, quantifying cracks in term of the crack length, crack area, crack density and crack roughness can be equally demanding.

These parameters need to be related to the material behaviour of concrete. Over the years, many crack-detecting techniques have been developed and they can be distinguished under two categories namely visualization and quantifications. Visualization of cracks can be done either under naked eye or with the aid of optical means (light and electron-microscope, atomic force microscope, x-ray tomography and others).

2.7 Technique proposed to study cracking

2.7.1 X-ray computed tomography

X-ray computed tomography system consists of dual-focus 420 KV continuous x-ray sources and a digital detector. The detector consists of 512 channels linear array $CdWO_4$ detector elements and the nominal spatial resolution of the image is 0.250mm.

X-ray computed tomography is a non-destructive technique for visualizing features in the interior solid objects in order to obtain the digital information on their 3-D geometry and topology. In this instrument, directing planar X-rays are passed through the specimen in several sequences of paths in various directions which produce a set of CT images. The measurement of intensity of X-ray is measured before it enters the specimen and after it passes through it. After collecting the intensity measurement for the full rotation of the specimen, the scanning of the slice is completed. Finally, the specimen is shifted vertically by a fixed amount and the entire procedure is repeated to produce additional slices. The Figure 30 illustrates the major steps involved in image analysis technique and figure shows a schematic drawing of an x-ray computed tomography.

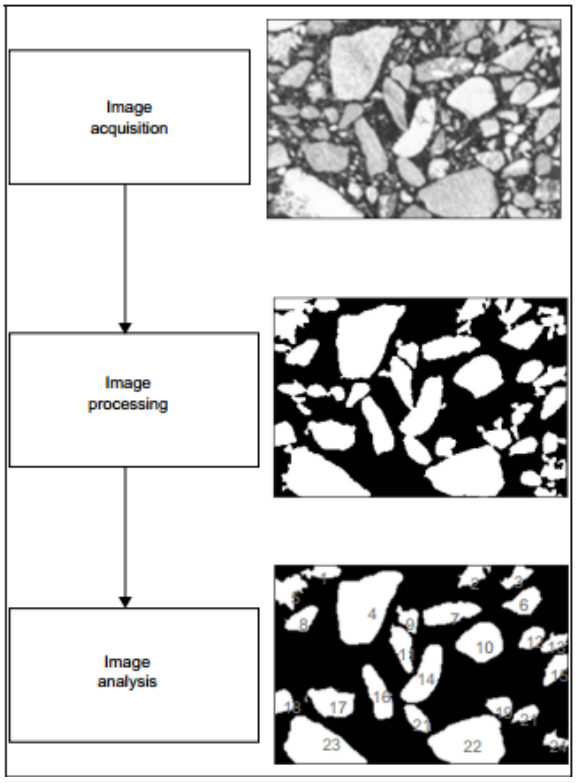

Figure 30: Major step involved in image analysis technique (Gopalakrishnan et al., 2007).

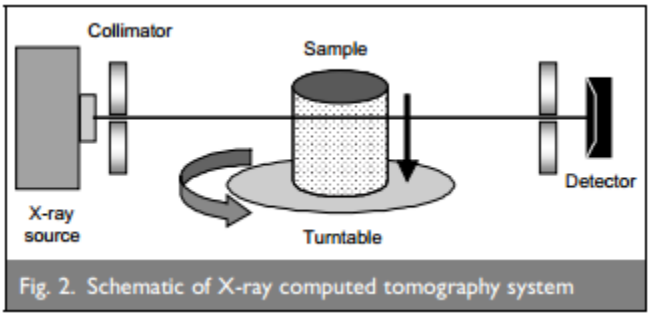

Figure 31: Schematic of an X-ray computed tomography (Gopalakrishnan et al., 2007)

2.7.2 Visual inspection

Visual inspection refers to phenomena visible to human eye and it provides information, for instance, effect of grain boundaries on crack path, crack orientation influence of individual lugs and among others. This method is likely to be qualitative in nature and it is less likely to be

quantitative. Besides, visual inspection is necessary before the implementation of more sophisticated evaluation methods.

2.7.3 Scanning electron microscope (SEM)

The scanning electron microscope (SEM) is one of the most powerful and versatile tools available to study and analyses microstructural characteristics of cement and concrete. Le Chattelier, (1882) was the first pioneer to apply it in order to study cementitious materials. Although several researchers used this tool to study concrete, yet none studied cracks until Diamond and Mindess, (1980) used it with a magnification from 35× to 450× to observe the growth of surface cracks during loading.

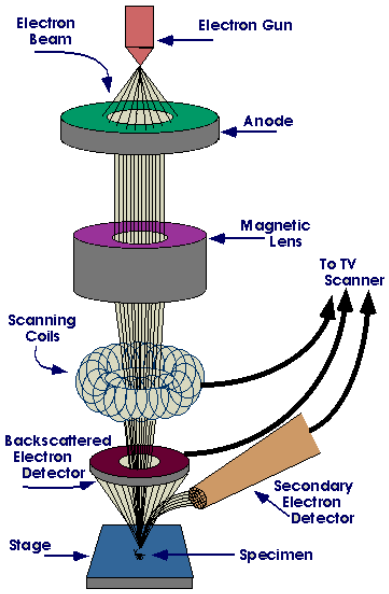

Figure 32: Scanning Electron Microscope (Carlesso, 2008)

Moreover, in order, to preserve the microstructure of stress-induced microcracks in concrete, the application of liquid phase material namely Wood's metal which has a melting point range from 70 ℃ to 88 ℃. For the past few years, this alloy was used to study the microstructure of different material (Chang et al. 1996, Nemati, 1994, Pyrak, 1988, Yadev et al. 1984 and Zheng, 1989).

Chapter 3. Methodology

3.1 Numerical analysis

Several micromechanical parameters are necessary to simulate a specific material in Discrete Element Method (DEM). For instance, Oda and Iwashita, (1999) and O'Sullivan, (2011) mentioned the predominant parameters that govern the stress-strain behaviour of a material is the stiffness of particle contacts (Kn and Ks) and the friction coefficient (μ).

3.1.1 Numerical Sample preparation

It is important to mock test specimen in laboratory in order to generate a synthetic specimen. The procedure to prepare a synthetic sample in order to simulate the laboratory test using PFC3D will be illustrated in this chapter. It is a well-known fact that the mechanical behaviour of numerical sample, in particular, DEM depends on parameters such as the strength of contacts, particle size distribution, porosity and stiffness. Since one of the objectives is to replicate the specimens tested in laboratory, a concrete of strength 30Mpa is chosen to achieve this aim. The volumetric proportion is based on the design code of Eurocode (BS EN 1992-1-1:2004):

Table 1: Mix Design quantity of concrete

Constituents	Quantity Per trial mix
Cement	43.6 kg
Water	20.7 kg
Fine Aggregate	68.8 kg
Coarse Aggregate (10 mm)	84.9 kg

The quantity of cement, water, fine aggregate and coarse required to produce a concrete of characteristic strength of 30MPa are tabulated in Table 1.

3.1.2 Particle generation and Boundary

In numerical simulation of a system, the assembly of particles needs to be generated within a set of confining boundaries. Hence, wall in PFC3D is used to generate the boundary which defines the confinement of the spheres (balls in PFC3D) which is generated after the confinement has been created. The boundary (finite wall) as illustrated in Figure 33 is a set of confining planes that has arbitrarily defined contact properties and it acts as a boundary constraint to restrict the

movement of sphere beyond the boundaries. Besides, the contact force is calculated by the force-displacement law for both the sphere to boundary contact and sphere to sphere contact.

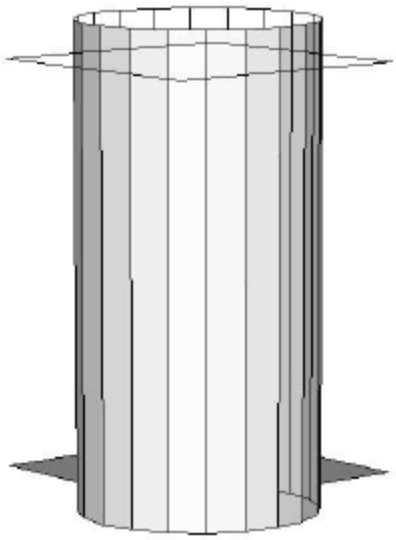

Figure 33: Boundaries created from PFC3D

The number of particles to be generated into the available space is computed using the following equation:

$$N = \frac{3V(1-n)}{4\pi\bar{R}^3} \tag{3.1}$$

where;

n: Target number of particle to be generated

V: Total volume of given space

N: Desired porosity

$\bar{R}$: Mean Radius

3.1.3 Preparation of bonded sphere network

In DEM simulation, the packing of the particle is one of the most important issues for generating the model. Packing density is the basic parameter defined as the ratio of the volume of particles

to the total volume they occupy that relate an array of particles. Scott, (1960) defines a dense random packing as the upper limit whose density is 0.63 based on his experiment work. Besides, he further added that it is unlikely that the packing of balls being significantly influenced by friction. Nevertheless, this claimed was further supported by Sohn and Moreland, (1968) investigate the effect of particle size distribution on packing density through a series of laboratory investigation of sands. Adam and Matheson (1972)'s works using numerical investigation comply as well with the claim of Scott, (1960) and Sohn and Moreland, (1968).

For a PFC3D, a high coordination number is defined as the average number of contacts per particle that is necessary to create a good contact bond network. For instance, if the particles have no real contact with the non-zero overlap, a contact bond cannot be formed. The contact between particles determines the topological connectivity of the system of the sphere and forces transferred (Bezrukov et al., 2011). Rothenburg et al., (1992) mentioned that a particle assembly requires at least four contacts per particle on average to carry a load. Besides, Collop et al, (2004) wrote that in order to model an internal contact structure, at least 4 contacts per spheres on average in the particle assembly is required. Nevertheless, it should be noted that Bezrukov et al., (2011) used a special static approach and observed that a dense random packing sphere requires at least 6 contacts number on average and Bernal and Mason, (1960) observed an average contact number of 6.4.

However, this research will create a sample with a good contact system that comprises at least with a minimum of four contacts with its neighbouring particles and with a packing density of 0.63. This will be achieved by scanning every contact in the system in order to detect sphere with less than four contacts for example, Figure 34 shows particles with less than four contacts. Then the spheres are allowed to expand about less than 1% in order to create additional contacts with neighbouring particles. Lee, (2006) showed from a numerical sample generation procedure in PFC3D 5 to 8% of the total particles in the system are with less than four contacts. Moreover, during the simulation, the sphere will be allowed to re-orient them in order to reach an isotropic equilibrium state within the sample.

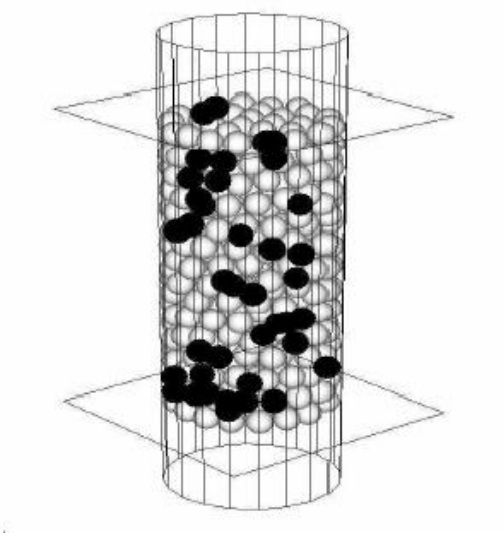

Figure 34: Schematic drawing of a compressive test showing spheres with less than 4 contacts

Hence, after completing the above procedure, a numerical sample with low isotropic internal stress and a minimum of four contacts per sphere will be created. The normal and shear contact bonds will be added to all contact in the system as shown in Figure 35. Moreover, new contact bond will continuously form as new contacts are formed in the system during simulations.

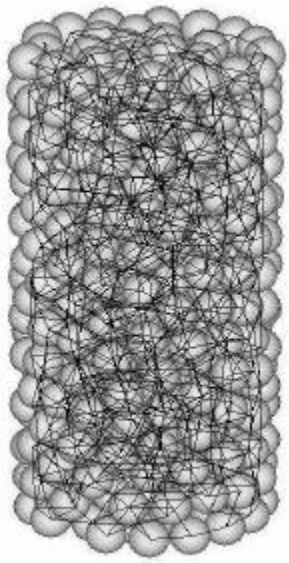

Figure 35: Schematic drawing of a compressive test with a contact bond (normal and shear bonds)

3.1.1.4 Achieving an Isotropic equilibrium state

The numerical sample generated to model concrete needs to be initially isotropic and free of internal force. However, upon expansion of the sphere to achieve desired radii, there is a large amount of overlap at contact point which results in a non-uniform distribution of contact forces within the system. Hence, to achieve an isotropic equilibrium state, a pre-load cycling within the PFC program is conducted whereby the spheres are allowed to re-orient themselves. This will allow the particles to 'settle' to equilibrium so that the contact forces of the sphere are uniformly distributed. Nevertheless, it should be noted that the friction coefficient between the wall and the particle is set to zero during pre-loading in order to facilitate the re-orientation of the sphere.

ITASCA, (2003) suggested that the isotropic stress needs to be reduced to less than 1% of the uniaxial compressive strength. A sample needs to have a low internal stress prior testing and this can be achieved by reducing the particles' radii which in turn decrease the magnitude of overlapping between particles, hence, causing a reduction in contact force within the system. In summary, the particles' radii are reduced and cycle to an equilibrium state in order to have a low internal stress. Figure 36 illustrates the effect of the reduction of radii on the isotropic stress

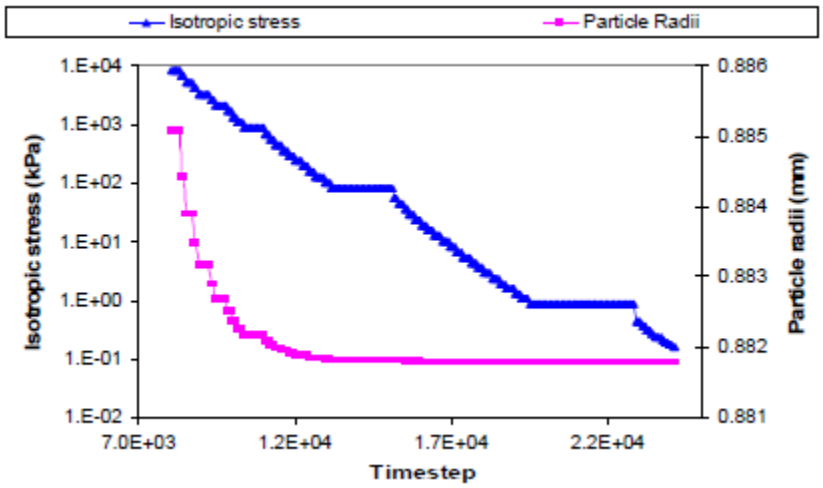

Figure 36: Effect of reducing the particle's radii on isotropic stress (Wu, 2009)

Figure 37 illustrates the contact force distribution under isotropic equilibrium state whereby the line represents compressive force and the thickness corresponds to its magnitude. It can be

clearly seen that the contact forces are uniformly distributed as expected under an isotropic equilibrium state.

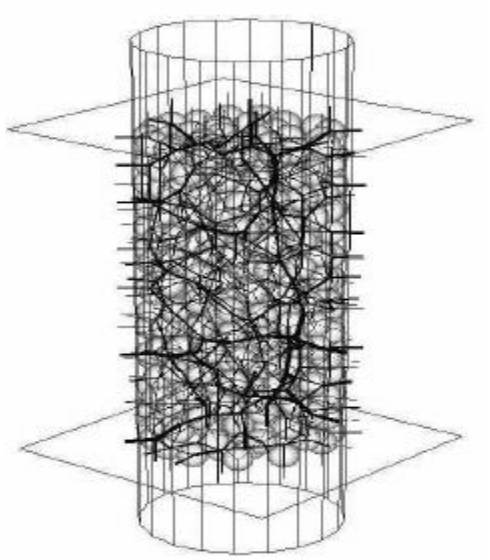

Figure 37: Schematic drawing of Contact force distribution under isotropic stress

3.2 Method of measurement

3.2.1 Measurement sphere

A measurement sphere is defined as a specific volume of space in PFC3D that can be used to measure the main properties of a numerical sample, for instance, stress, strain, porosity or coordination number. This specified a 3D volume of space typically a sphere which is also referred to as “measurement sphere” with a specific radius which can be installed within a different part of the sample. This method will be applied to this research to generate the stress and strain within the particular sample tested as illustrated in Figure 38.

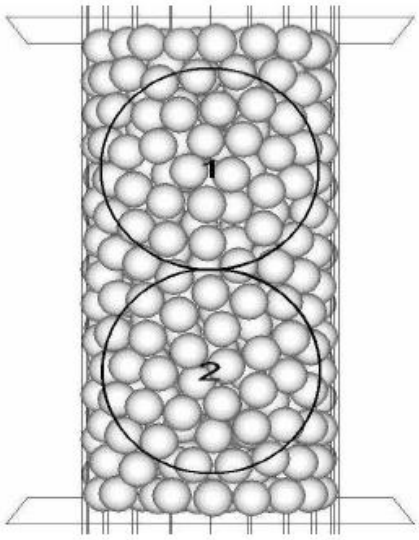

Figure 38: Schematic drawing of measurement sphere technique in a compressive test

3.2.2 Measurement of axial stress and strain

Before testing, the original coordinates of the top and bottom platens will be recorded in the computer memory. Then, the coordinates of the platen are updated at each time step through the simulation. Hence, the axial strain of the sample is computed based on the change of the position of the loading platen before and after the simulation. Moreover, the magnitude of overlapping between the wall and adjacent balls is small in contrast to the axial displacement of the sample, as such, it is considered to be negligible.

The axial stress also referred as the nominal stress will be computed from the contact forces between the particles in contact with the loading platens divided by the area of the platen which is constant.

3.3 Experimental analysis

3.3.1 Mixing and sampling of fresh concrete in the laboratory

The material should be stored in a separate airtight container of appropriate size in a dry place. In order to ensure there is a greater uniformity in the material, it should be stirred thoroughly either with a hand tool or a suitable mixer. The aggregate's moisture content should be determined according to BS 812: Part 109.

The aggregates shall be in one of the following conditions:

- Oven dried as described in BS 812: Part 100.

- Air dried at (25 ± 5) °C.
- Saturated surface dry as described in BS 812: Part 100.
- Saturated by soaking in water for at least 24 hours.

The temperature of the material should be around (25 ±5) ℃ before mixing. During batching, the quantity of concrete in each batch should be at least 10 % more than that necessary for the test. If the aggregate during mixing is dry, it needs to be soaked with some of the mixing water before mixing other material. Besides, the concrete should be mixed in such a way preferably with a machine in order to minimize loss of water or materials. Upon mixing, the mixer should be charged with about one half of coarse aggregate, then with fine aggregate, then with cement and finally with the remaining coarse aggregate. Water should be added during the first 30 seconds and then the mixing should continue for at least 2 minutes until all the concrete seems to be uniform and homogeneous. The preparation of the specimens for the tests on fresh concrete or hardened concrete should be carried during a period of not more than one hour from the addition of water to the cement.

3.3.2 Flexural test (Four-point flexural test and Three-point flexural test)

The most practical method to characterize the strength and ductility of concrete is called flexural tests. The test is performed either on a prism subjected to a centre-point loading (Three-point flexural test) or a symmetrical two-point loading (Four-point flexural test). This method is much popular because a larger percentage of the span is subjected to the maximum bending moment and as such, there is a greater possibility for the weakest part of the element to be subjected to a maximum stress.

The three-point flexural test could be performed in accordance with as per BS 1881: Part 118: 1983 whereby a simple plain concrete beam is loaded at one-third span point and the span of the beam is 3 times its depth. If fracture takes place outside the middle one-third, then according to BS 1881: Part 118: 1983, the test result should be discarded. The four-point flexural test procedure will be in accordance with AASHTO T 97.

The most common flexural strength measured in plain concrete beam is the modulus of rupture ($f_{fl,ult}$) and it is calculated using ordinary elastic theory from the maximum bending moment allowed by the beam. The modulus of rupture is often referred as an indirect measure of tensile strength of concrete but in reality, it is greater than the tensile strength because it is close to failure

(Neville et al, 1983). The modulus of rupture is for a prism under a symmetrical four point bending test is given as follows:

The flexural strength σ_f is given as follows:

1. Four-point flexural test where loading span is $1/2$ of the support span

$$\sigma_f = \frac{3}{4}\frac{FL}{bd^2} \tag{3.2}$$

2. Four-point flexural test where loading span is $1/3$ of the support span

$$\sigma_f = \frac{FL}{bd^2} \tag{3.3}$$

3. Three-point flexural test

$$\sigma_f = \frac{3}{2}\frac{FL}{bd^2} \tag{3.4}$$

where;

F: maximum total load on the beam

L: span of the beam

b: width of the beam

d: depth of the beam

3.3.3 Splitting tension test

It is the most popular indirect method used to measure tensile strength of plain concrete. It consists of applying a load to a cylinder along two opposite generatrices. As such, this subjects the element to a vertical compressive stress along the loading plane and horizontal tensile stress normal to this plane. A loading strip of a width of about a tenth of the diameter of the cylinder is interposed between the cylinder and platen in order to reduce the localized compressive stress applied directly under the load.

The maximum tensile stress is constant over 80% of the diameter (Nanni, 1988) and the maximum tensile stress at the centre of the cylinder is expressed as follows:

$$f_{ct,sp} = \frac{2P}{\pi lD} \quad (3.5)$$

where;

P: compressive load on the cylinder

l: length of the cylinder

D: diameter of the cylinder

The test could be performed on cubes or prism. Neville, (1981) mentioned that it is less reliable than cylinder because of its uneven stress distribution. Besides, Hansen, (1996) mentioned that cubes give higher splitting strength than cylinders with the same cross-sectional dimension and also argues that cubes shouldn't be used as they will overestimate the tensile strength.

3.3.4 Compression test

The compression strength test shows the capacity of a material or structure to withstand load which can be tested either destructively or non-destructively. In compression test, BS EN 12390, (2009) is followed for the testing of 150×150×150 mm cubes and 150 (diameter) × 300 (height) cylinders.

The specimens that are stored in water need to be tested within one hour of removal whilst they are still wet. Surface water and grit on the cube shall be wiped off and projecting fins removed.

The load shall be applied steadily and without shock such that the stress is increased at a rate within the range (0.6±0.2) MPa/s until no greater load can sustain.

The compressive strength is given as

$$f_{ct,sp} = \frac{P}{A} \quad (3.6)$$

P: compressive load on the cylinder

A: specimen cross-sectional area

The mode of failure in concrete cylinder is shown below:

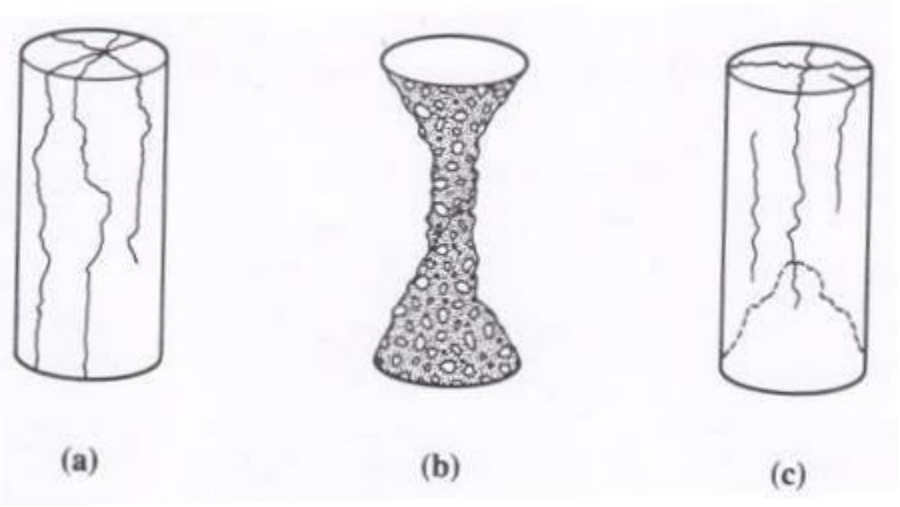

Figure 39: Failure patterns of cylinder (Neville and Brooks, 1987)

Chapter 4. Discrete Element Models developed

4.1 Introduction

This Chapter will lay emphasis on the models created in order to understand the behaviour of concrete. PFC 3D was used to develop three models namely: 3-point flexural test, 4-point flexural test, and Compressive test.

4.2 Uniaxial Compressive test

4.2.1 Three-dimensional Sample Assembly

It is very important to mock the test specimen in order to generate a synthetic specimen. In this present study, the uniaxial compression test of a concrete cylinder with diameter 150mm and height 300 mm was modelled numerically with PFC 3D program. The coding of the model was developed using Fish programming language (refer to **Appendix A.1**) and run using the program PFC 3D. This model will be used to simulate the failure behaviour through discrete element modelling simulation. A number of 44339 discrete spherical elements are used to model concrete as illustrated in Figure 40. The loading platen for the uniaxial compressive test is simulated by the top and bottom walls which act as boundary conditions. The system is loaded in a displacement-controlled way. ITASCA, (2003) mentioned that the walls which are intersecting each other are not an issue because the wall interacts only with the balls, not with one another.

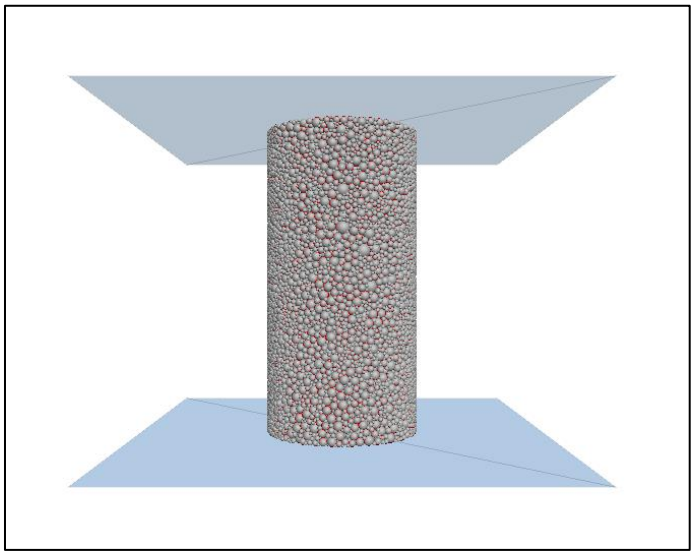

Figure 40: Particle assembly with contact bonds and Parallel Bond

The size of aggregate used in this numerical model of a uniaxial compressive test is based on the actual particle size distribution obtained from the sieve analysis test conducted in the laboratory. An algorithm coded using fish programming was developed in order to represent the realistic particles size distribution as illustrated in Figure 41. As such, this numerical model mimics the realistic particle size distribution based on result from the sieve analysis. Figure 41 illustrates the gradation of the particles in the experiment (green line) and gradation of the particles in numerical model (red line). The developed algorithm tries different configurations to place the spheres into the cylinder until it matches the correct gradation of the particles based on the laboratory result. However, due to the limitation of the computational power of the workstation available, this model doesn't encompass fine aggregates and is limited to coarse aggregates only.

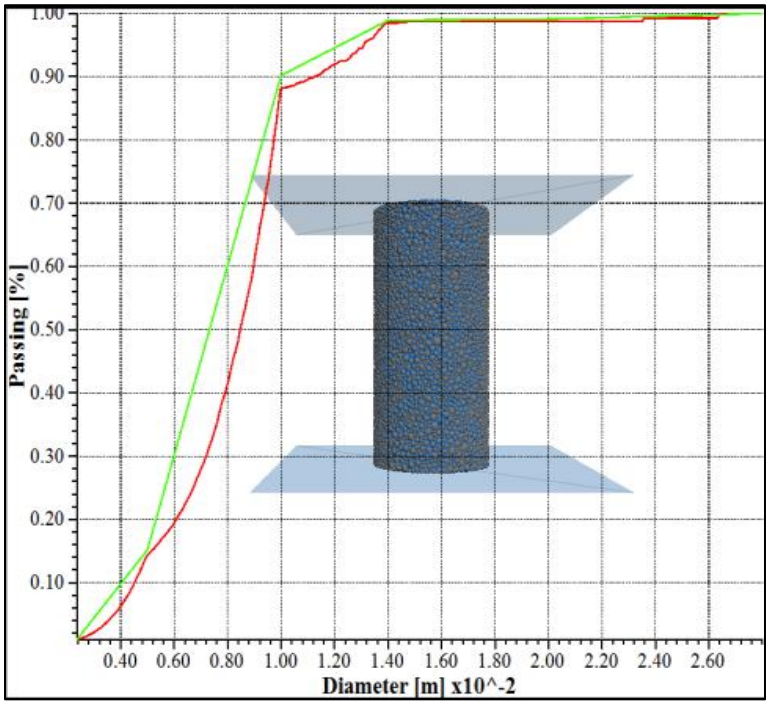

Figure 41: Gradation of particles in uniaxial compressive test

4.2.2 Calibration of parameters

The elastic macroscopic properties for instance Young's modulus, E and Poisson's ratio, υ are the input parameters for the model. The local stiffnesses that are derived from the macroscopic properties are given by the 'Micro-Macro' relationship. These 'Micro-Macro' relationship developed by Liao et al. (1997) which linked those local stiffness are used for homogenized model in regular assemblies; however, they have been modified to represent the disordered assemblies

(see equation 4.1 and 4.2). The input parameters for the uniaxial compressive test are tabulated in Table 2.

$$E = \frac{D_{eq}}{S_{int}} k_n \frac{\left(\beta + \gamma \frac{k_s}{k_n}\right)}{\left(\alpha + \frac{k_s}{k_n}\right)} \tag{4.1}$$

$$\upsilon = \frac{\left(\beta + \gamma \frac{k_s}{k_n}\right)}{\left(\alpha + \frac{k_s}{k_n}\right)} \tag{4.2}$$

where;

D_{eq}: Initial distance between particles

$S_{inter} = \min\left(\pi R_a^2, \pi R_b^2\right)$

α, β, γ: Parameters related to the radius of interaction between particles (Rousseau, 2009)

Table 2: Uniaxial compressive test model's Parameters

Parameters	values
Young's Modulus, E (GPa)	30
Poisson's ratio, υ	0.2
Tensile Strength, f_t (MPa)	5.3
Cohesion Strength, C_0 (MPa)	15
Friction Angle (°)	20
Density (Kg/m^3)	2500

4.2.3 Experimental setup of uniaxial compressive test

A uniaxial compressive test was carried in the laboratory of XJTLU using similar dimensions employed in the numerical development of the model. The real compressive strength of the reference concrete was determined using an Alpha 3-3000 S type Universal test machine as illustrated in Figure 42. Four standard concrete cylinders were casted and cured for 28 days. The results obtained from the test are illustrated in Figure 43.

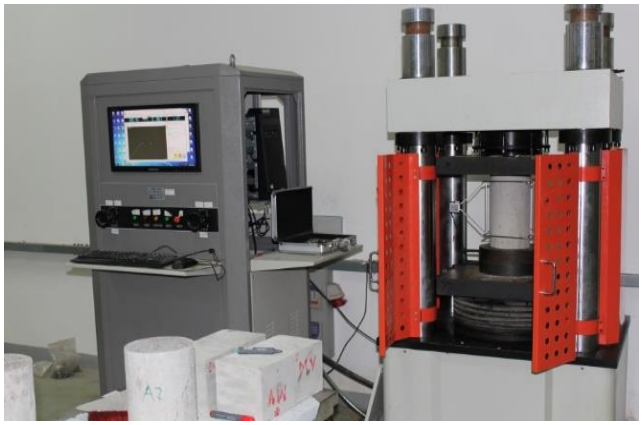

Figure 42: Uniaxial compressive test in XJTLU lab

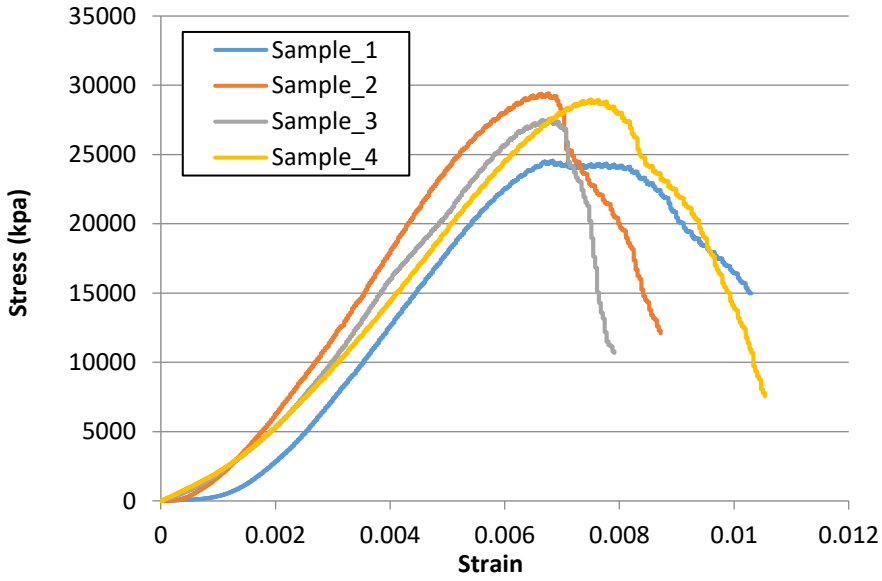

Figure 43: Uniaxial compressive test experimental result

4.2.4 Result and Discussion

4.2.4.1 Stress-strain curves observation

The validation process of the model will be carried as illustrated Figure 44. The validation was achieved after several iterations steps in order to calibrate the parameters as illustrated in Figure 45. Although not all the 4 samples in the experiment (in particular series 1) have reached the target compressive strength of 30 MPa unlike the DEM simulation. However, series 2, 3 and 4 are almost closed to the target strength. Beckmann et al., (2012) mentioned that two specimens produced and tested under the same conditions will never be absolutely identical in real life and this is akin to the observation made in this research.

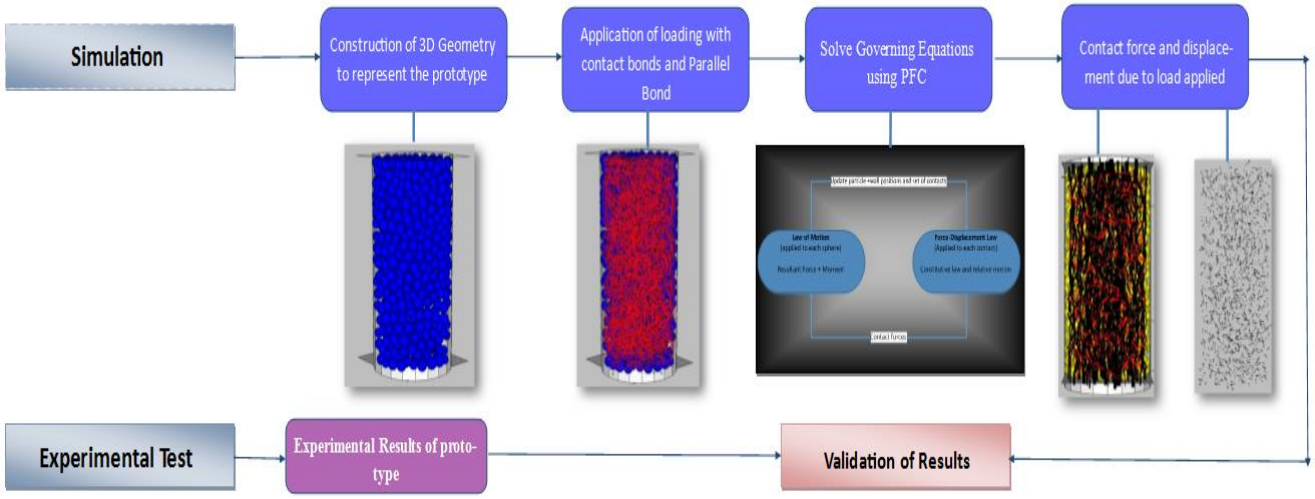

Figure 44: Overview of the Validation process for uniaxial compressive test

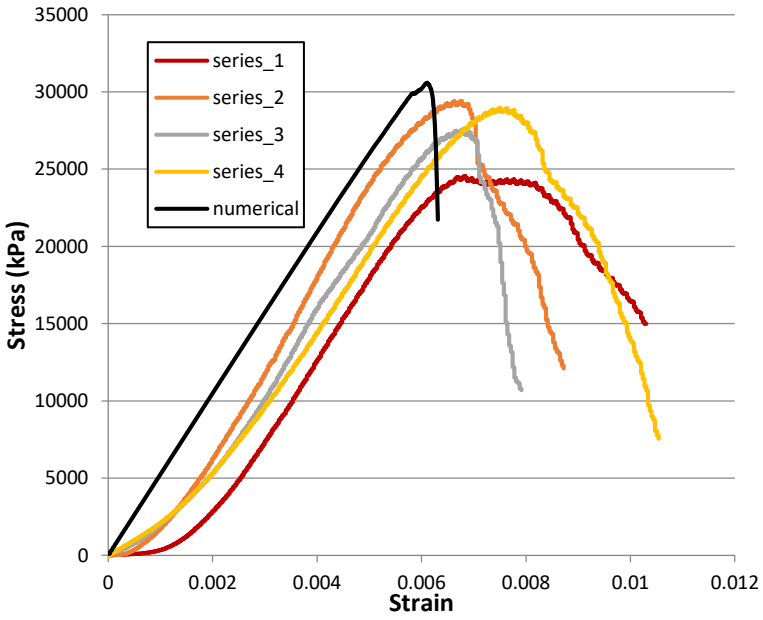

Figure 45: Validation of Numerical Simulation against experimental result of uniaxial test

Moreover, it is observed as illustrated in Figure 45 that the stress-strain result obtained from the numerical simulation is almost similar to the experimental result in particular series 2, 3 and 4. This observation is in line with the conclusion made by several researchers (Iturrioz et al., 2013; Nitka and Tejchman, 2015; Gyurkó et al., 2014; Suchorzewski et al., 2017; Abbasnia and Aslami, 2014; Hentz et al., 2002; Beckmann et al., 2012; Hentz et al., 2004) which states that DEM is capable of simulating a suitable approximation of concrete behaviour under uniaxial compression

test. However, unlike the observation made by (Iturrioz et al., 2013; Nitka and Tejchman, 2015; Suchorzewski et al., 2017) for 3D simulation, the 3D model developed in this research is capable of simulating concrete and the validation result obtained are relative good. It should be noted those researchers (Iturrioz et al., 2013; Nitka and Tejchman, 2015; Suchorzewski et al., 2017) used a number of spheres lesser than 5000 which doesn't represent the actual scenario unlike this model used in this research which distributes the number of particles according to the grading of the aggregate

Besides, it can be observed that the numerical model yields a bit earlier than the experiment. Hentz et al., (2002) mentioned that it is important that the element rotation is inhibited in order to allow the ratio of the compressive over tensile strength to be equal to 10. In addition to, Hentz et al., (2009) also mentioned that due to low softening, free rotations of the sphere are induced and this makes the model yield earlier. As such, inhibiting the free rotation will make the numerical model yield similar to the experimental result. In future work, the code can be modified to tackle this issue. Nevertheless, it is really difficult to match perfectly the numerical result with experimental results as the aggregates distribution varies from sample to sample. Besides, the number of spheres used to build the numerical model is 44339, unlike other researchers which mainly restrict the number of particles below 5000. As such, this increases the complexity of the validation of the numerical model.

4.2.4.2 Crack pattern observation

The particular advantage of using DEM is that no crack elements are required to observe the evolution of cracking because they are discontinuous features which are an inherent part of this method. In other words, this means that a disruption of the bond between the spheres automatically induced a crack. Figure 46 illustrates the fracture behaviour of the concrete cylinder under loading. It is clearly observed that the cracking pattern is similar to the one of the experimental result. Propagation of cracks and deformation pattern can be observed on the top surface in both numerical and experimental result. Micro-cracks are observed in the lower surface of the numerical model which will eventually change into macroscopic cracks later. However, it is hard to observed micro-cracks in experimental result with naked eyes. As such DEM is a great tool to study the initiation and propagation of micro-cracks which eventually coalesce to form macro-cracks. In addition to, it is possible for DEM to observe the crack propagation within the sample which shows that it is a non-destructive technique.

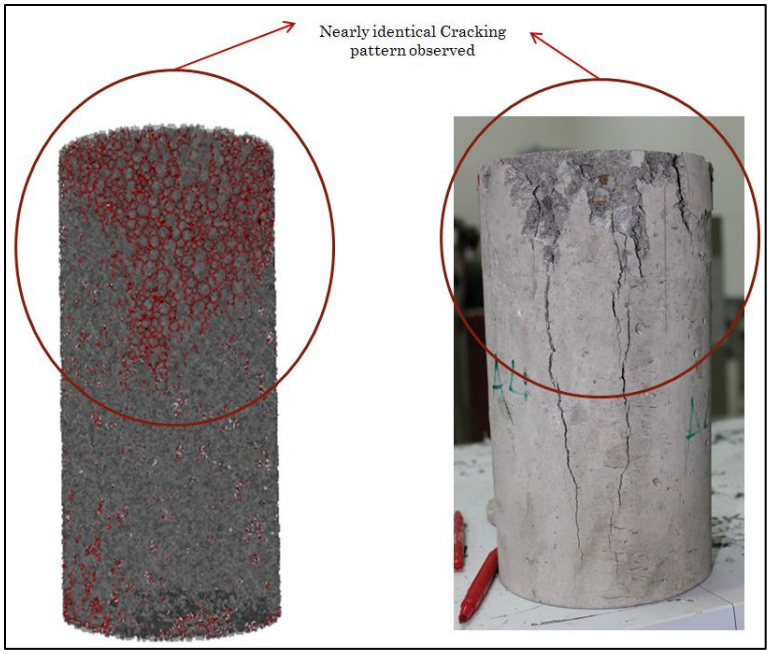

Figure 46: Crack pattern of DEM result from Experimental result (uniaxial compression test)

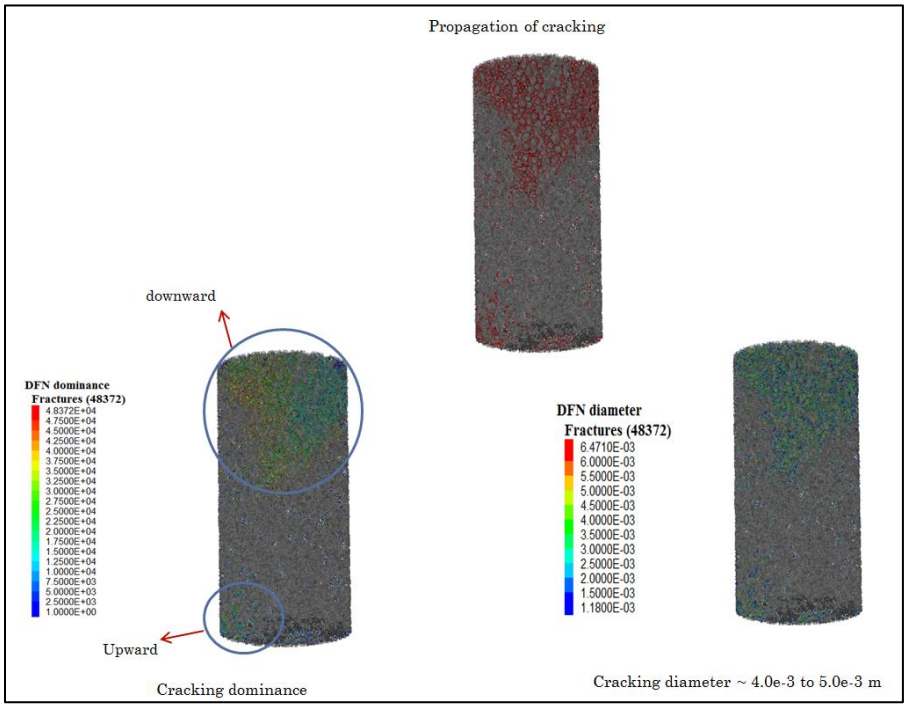

Figure 47: Cracking dominance and cracking diameter

Discrete fracture networks (DFN) illustrates the cracking dominance. The cracking dominance is the path where the cracks are more prone to undertake on a scale where blue being less dominant and red being most dominant (see Figure 47). As mentioned above, the macro-cracks are more

dominant on the upper part of the cylinder. As such, it can be observed that cracks in the upper part are propagating toward the centre of the cylinder in a downward direction according to the DFN scale which is becoming yellowish. On the other hand, the cracks from the lower part of the cylinder are moving in an upward direction. Hence, it can be concluded the crack evolution is akin to the observation made in the laboratory experiment. With DEM, it is also possible to measure the cracking opening diameter which is difficult to obtain in the laboratory. It was observed that the cracking opening diameter that is formed in the cylinder is between 4.0 mm to 5.0 mm.

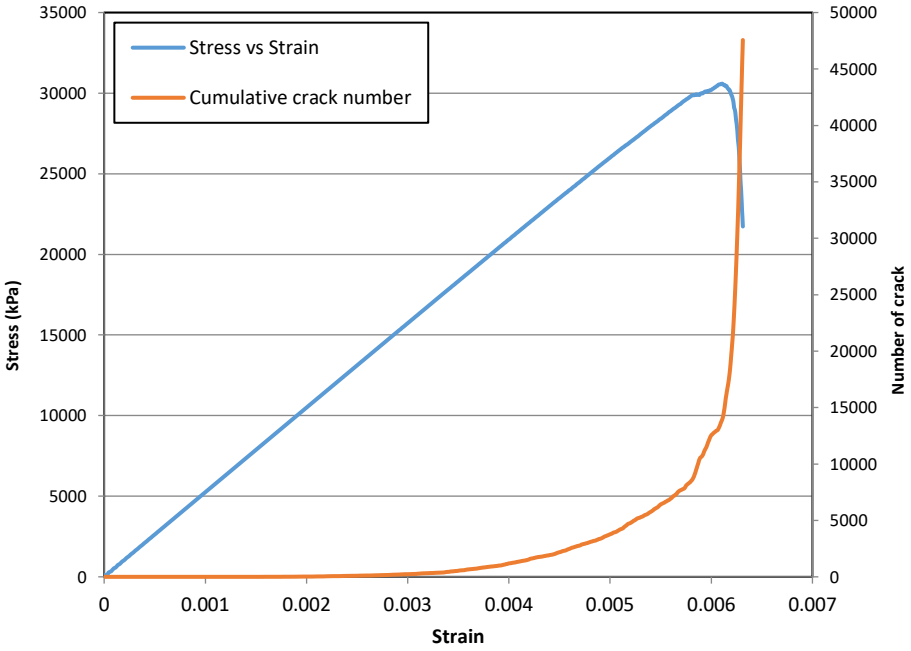

Figure 48: The progression of cumulative cracking number with stress vs strain (uniaxial compressive test)

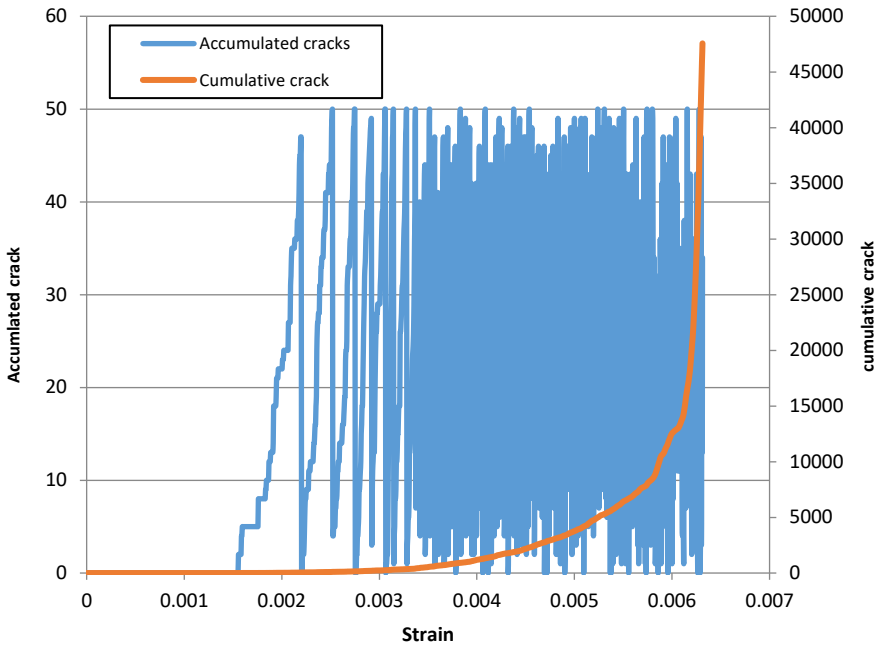

Figure 49: Accumulated crack and Cumulative crack

It must be noted that particles which were not in contact before at the beginning can come into contact at later phase during the on-going damaging process. This can be a challenging process to identify the bond breakages which are leading to the initiation of crack. Hence, to solve this issue, the model consists of algorithms namely contact detection (see William and O'Conner, 1999) and discrete fracture network (DFN) which are implemented in the programming code and this will help identify the formation of crack due bond breakage between the spheres. The model starts to analyse if there is any crack appearance due to bond breakage between the spheres right from the moment the load is applied as illustrated in Figure 49. Figure 48 illustrates the progression of the cumulative micro-cracks which are referred as the number of bond broken that will lead to an emergence of macroscopic crack. It is observed that crack number (bond broken) starts to increase around the strain 0.003. This is in line with the observation made by Tejchman, J. and Bobiński, (2013) where it was observed that the first micro cracks appear in hardening region before the peak. Beyond the strain 0.005, the rate of crack number starts to increase gradually. However, once the strain of 0.006 is hit, the material yield and there is a sharp increase in crack number. It was at this point where visible macroscopic cracks spread and coalesce to cause failure of the concrete cylinder. Hence, it can be concluded that this DEM model can capture crack evolution and failure at microscopic scale.

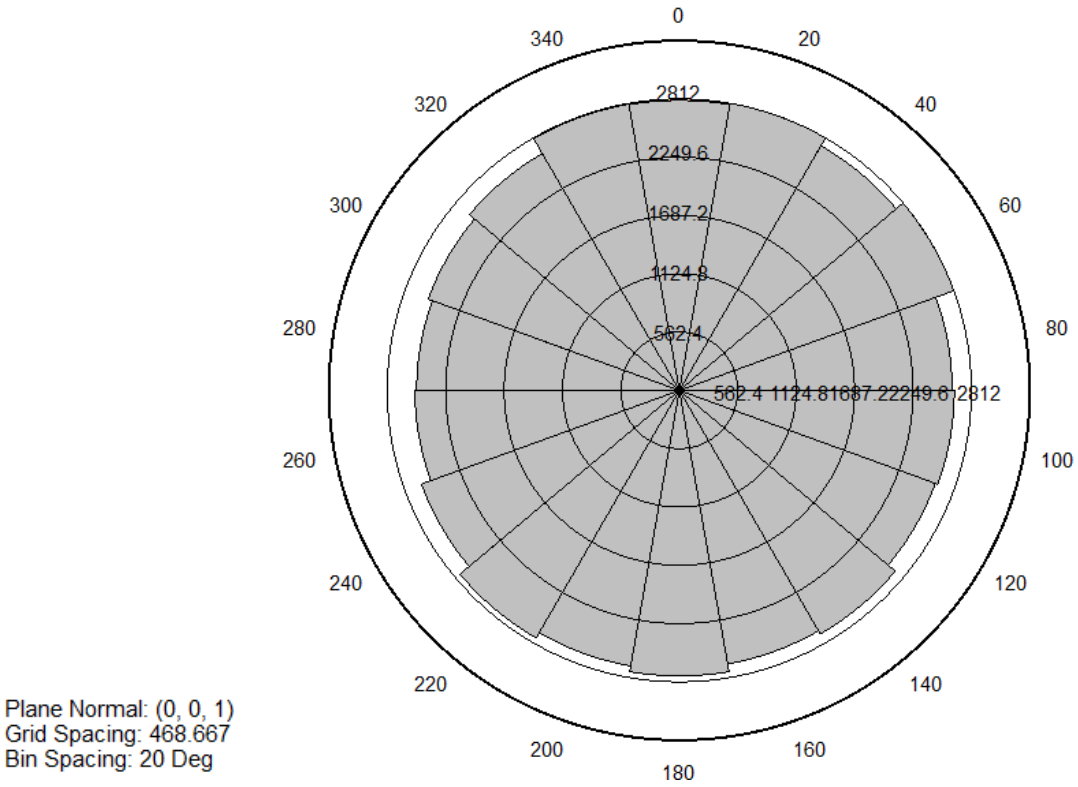

Figure 50: Rosette plots showing the number of crack and orientations in different bearings

One of the important features with DEM which cannot be observed in the laboratory is the orientation of the propagation of the cracks. In this research, a rosette plot is used to display the orientation of cracks and the number of cracks at each particular angle respectively as illustrated in Figure 50. This will help to identity which plane of the concrete requires much attention particularly useful in building where it is difficult to predict the initiation and propagation of cracks. It is observed in Figure 50 that at 0°, 20°, 60° and 340° with a number of crack number of 2812; these particular directions in the x-z plane accounts for the larger number of crack which induced larger macro crack that can possibly lead to failure. Hence, this feature of DEM can help to improve the understanding of the relationship between the microscopic and macroscopic occurrences during failure which will be beneficial in designing concrete safety structure.

4.2.4.3 Energy Input and dissipation behaviour

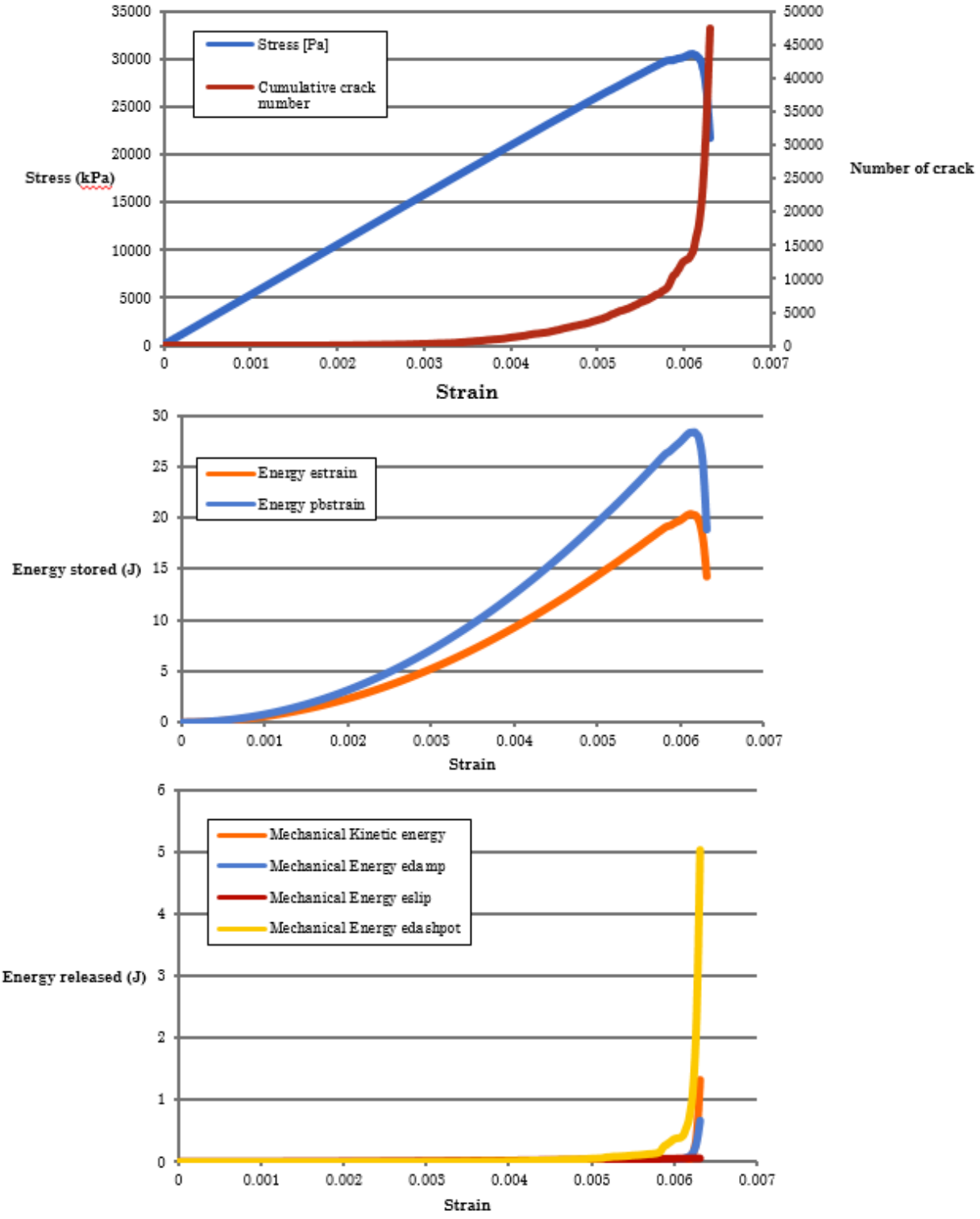

Figure 51: Energy stored and dissipated in the system

DEM models unlike in the laboratory experiments can be used to investigate the evolution of energy input or dissipation behaviour throughout the on-going damage process. In this research, the mechanical response will be studied in term of energy form in order to better understand the response of the discrete particles in the model. This will help to show that DEM can indeed capture the micromechanics of concrete. The energy form that will be studied in this model is strain energy stored in all linear contact spring and all parallel bond spring, kinetic energy of all entities in the assembly, frictional slip energy, energy of dashpot and local damping dissipation. The accumulated strain energy stored in both linear contact and parallel bond will be dissipated once the bonds between the particles are broken and the source of energy input to the system is the wall which provides the boundary condition.

Figure 51 illustrates the energy stored and released during the loading process whereby the evolution of various increment energy forms against the axial strain is plotted. It is observed that as the cracking number is increasing, the strain energy in both the parallel bond and linear contact bond is continuously building up due to elastic compression at the particle contacts. Upon reaching a strain of 0.006, overall maximum strain energy that linear contact springs can store is 21 J and the overall maximum strain energy that the Parallel bond springs can stored is 28J. Beyond the strain of 0.006, the stress decreases sharply and the strain energy stored in the linear contact and parallel bond also decreases. In addition with, it is also observed that there is a high dissipation of energy in the form of kinetic energy, frictional slip energy, Energy of dashpot, local damping. This energy dissipation coincides with the bond breakage events whereby there is a significant increase in crack number. This confirms that there is a strong relationship between the energy dissipation and bond failure.

4.2.5 Summary

The model was coded using fish programming language and run into the program PFC3D. The distribution of the particle was set according to the sieve analysis test and the model was validated through laboratory experiment. It was observed that comparison of the stress-strain response of numerical compared to the experimental result is relatively good. In addition with, the cracks patterns observed in the numerical result is similar to the experimental result. It is concluded from the observation obtained that 3D model of Discrete element modelling can be used to study cracking in concrete as the results obtained have a strong correlation with the laboratory observation. Since cracks are an inherent property of DEM, the 3D model was used to identify and visualize the evolution of micro cracks which was not possible in laboratory. These Micro cracks are formed due to the disruption of the bond between the spheres which subsequently

leads to the initiation of macroscopic cracks as observed in the result obtained. Moreover, with DEM unlike laboratory experiment, it is possible to study energy evolution and dissipation during the on-going damage process until the material yield. This could be used in the future to study fracture energy. The numerical model can be repeated several times in order to have a better grasp of the material random behaviour in term of failure process and cracking development. As such DEM is really efficient in investigating the fracture process and the initiation of cracks.

4.3 Three-point Unreinforced Flexural test

4.3.1 Three-dimensional Sample Assembly

In numerical studies, it is important to mock the test specimen in order to study its behaviour. Thus, in this present research, a three-point flexural test of a square cross-section beam with a height of 150mm, width 150 mm and length 500 was modelled numerically with discrete element method and validated through laboratory experiments. The coding of the model was developed using Fish programming language (refer to **Appendix A.2**) and run using the program PFC 3D. A number of 30789 discrete spherical elements are used to model concrete as illustrated in Figure 52. Three cylinders are used to apply the boundary conditions. The top cylinder is used to apply the loading condition whilst the other two cylinders act as supports. However, ITASCA, (2003) mentioned that the walls which are intersecting each other are not an issue because the wall interacts only with the balls, not with one another.

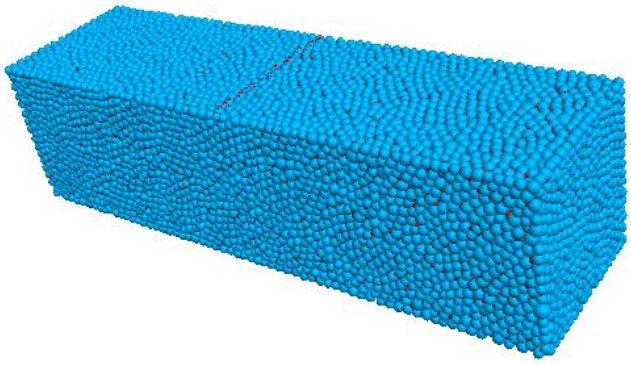

Figure 52: Particle assembly with contact bonds and Parallel Bond in Flexural test

Moreover, the size of aggregate used in this numerical model of a three-point flexural test is based on the actual particle size distribution obtained from the sieve analysis test conducted in the

laboratory. An algorithm coded using fish programming was developed in order to represent the realistic particles size distribution as illustrated Figure 53. As such, this numerical model mimics the realistic particle size distribution based on the result from the sieve analysis. Figure 53 illustrates the gradation of the particles in the experiment (green line) and gradation of the particles in numerical model (red line). The developed algorithm tries different configurations to place the spheres into the cylinder until it matches the correct gradation of the particles based on the laboratory result. However, due to the limitation of the computational power of the workstation available, this model does not encompass fine aggregates and is limited to coarse aggregates only.

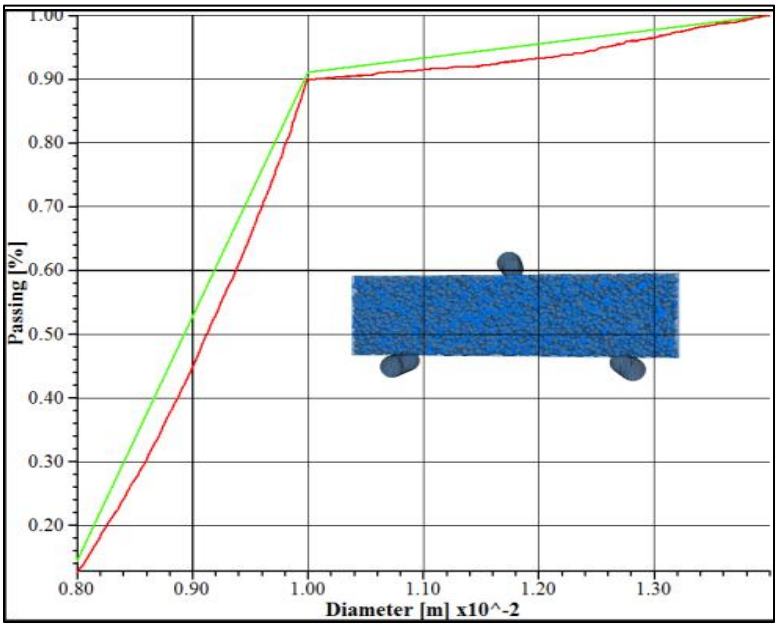

Figure 53: Gradation of particles in 3-point flexural test

4.3.2 Calibration of parameters

The elastic macroscopic properties for instance Young's modulus, E and Poisson's ratio, υ are the input parameters for the model. The local stiffnesses that are derived from the macroscopic properties are given by the 'Micro-Macro' relationship. These 'Micro-Macro' relationship developed by Liao et al., (1997) which linked those local stiffness are given by homogenized models used for homogenized model in regular assemblies; however, they have been modified to represent the disordered assemblies (see equation 3.3 and 3.4). The input parameters for the uniaxial compressive test are tabulated in Table 3.

$$E = \frac{D_{eq}}{S_{int}} k_n \frac{\left(\beta + \gamma \frac{k_s}{k_n}\right)}{\left(\alpha + \frac{k_s}{k_n}\right)} \tag{3.3}$$

$$\upsilon = \frac{\left(\beta + \gamma \frac{k_s}{k_n}\right)}{\left(\alpha + \frac{k_s}{k_n}\right)} \tag{3.4}$$

where;

D_{eq}: Initial distance between particles

$S_{inter} = \min\left(\pi R_a^2, \pi R_b^2\right)$

α, β, γ: Parameters related to the radius of interaction between particles (Rousseau, 2009)

Table 3: Three-point Flexural test model's Parameters

Parameters	values
Young's Modulus, E (GPa)	30
Poisson's ratio, υ	0.2
Tensile Strength, f_t (MPa)	5.3
Cohesion Strength, C_0 (MPa)	15
Friction Angle (°)	20
Density (Kg/m^3)	2500

4.3.3 Experimental setup of three-point flexural test

Three point flexural tests were carried out in the laboratory of XJTLU with similar dimension used in the numerical model as illustrated in Figure 54. The loading type employed in the experiment was displacement controlled and the results in term force versus jack displacement were recorded. Four standard concrete beams were casted and cured for 28 days. The results obtained from the tests are plotted in Figure 55.

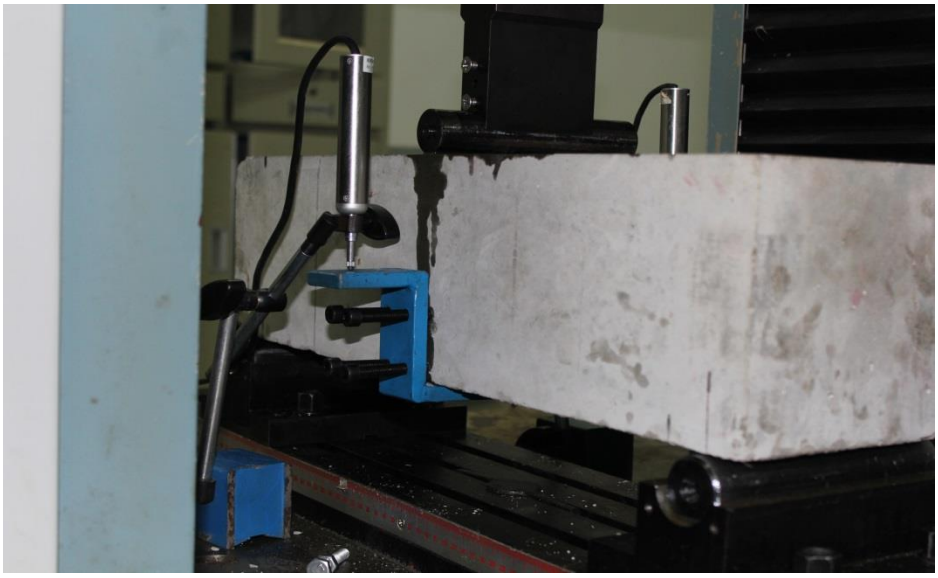

Figure 54: Three-point Flexural test in XJTLU lab

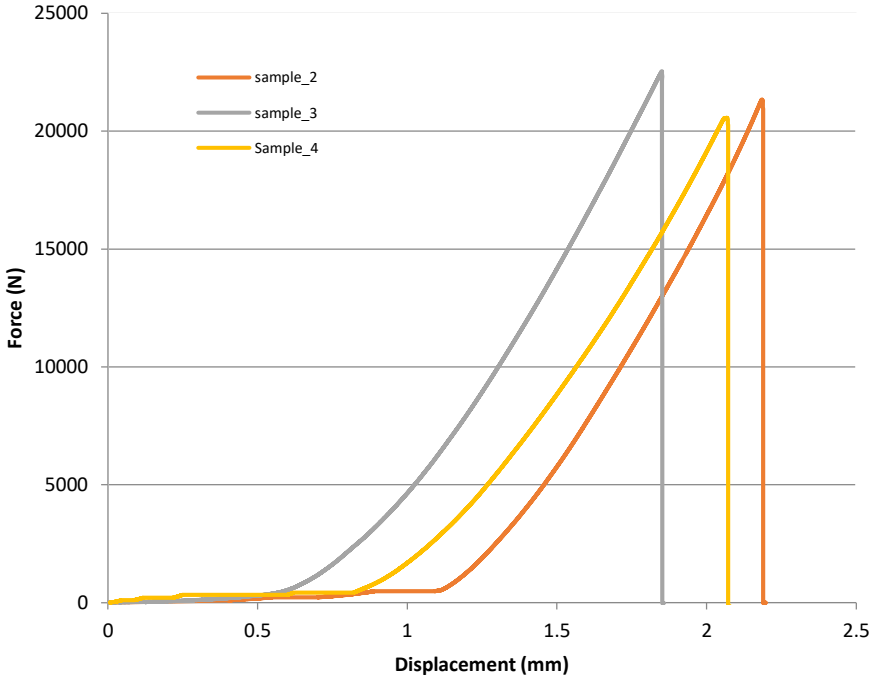

Figure 55: Three-point flexural test experimental result

4.3.4 Result and Discussion

4.3.4.1 Load versus Displacement

The validation process of the model will be carried as illustrated in Figure 56. The validation was achieved after several iterations steps in order to calibrate the parameters. The result obtained from both experiment and numerical results are validated as illustrated in Figure 57. Although, not all the results obtained from experimental samples (2, 3, and 4) are exactly identical. Yet, maximum force reached is almost the same for all those three samples. As Beckmann et al., (2012) mentioned, no two specimens produced and tested under the same conditions will be absolutely identical in real life and this is akin to the observation made in this research.

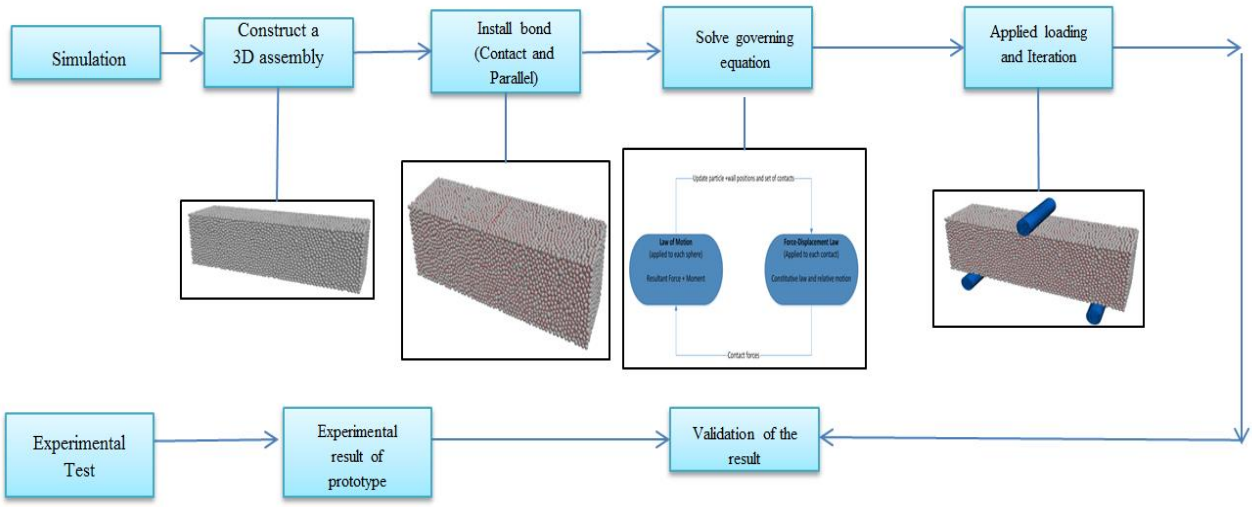

Figure 56: Overview of the validation of three-point flexural test

It is observed from the numerical result obtained in term of force versus jack displacement is almost similar to the one obtained from the experimental results. With a maximum force of 22 kN achieved at a displacement of 2.2 mm, it is almost similar to the results of sample 2 and 4. In the beginning phase, the graph of the numerical model has a less sharp gradient unlike the experimental result. This could due to the fact that the stiffness of the model is lower than the experimental one. This can be overcome by using lower local softening in model to counterbalance the free rotations of sphere. Hentz et al., (2009) mentioned that this will also retard the cracking of concrete. In addition with, Hentz et al., (2002) also mentioned that it is important that the element rotation is inhibited in order to allow the ratio of the compressive over tensile strength to be equal to 10. Hence, as future work, the effect of inhibiting the free rotation

of the sphere can be studied by modifying the existing programming code created. Another, explanation which can justify this discrepancy with the experimental result is that unlike other researchers (refer to the literature review), this model comprises of a large number of spheres (30789 discrete spherical elements) which can increase its complexity. Besides, the shape of the aggregates used in PFC 3D is spherical unlike in the real scenario which could be another reason of discrepancy between the two results (Numerical and Experimental). It is an undeniable fact that it is hard to mimic the behaviour of concrete in order to match perfectly the real scenario. Yet, in this research, DEM has proved that it can simulate a three-dimensional model of a flexural test of concrete whereby the result obtained is quite satisfactory.

A measurement sphere was created around the crack propagation region using fish programming language in order to study the stress tensors evolution in the xx, yy and zz plane. The result obtained is illustrated in Figure 58. It is observed that the stress developed in the zz plane is higher than the other planes. This observation predicts that the number of bonds broken in the zz plane will be higher. As such, this will eventually lead to the formation of macroscopic cracks which will coalesce to cause yielding of the concrete beam. Thus, by studying this microscopic parameter, it will contribute to a better understanding on the initiation and propagation of cracks in term of which plane; cracks are more prone to propagate due to the stress induced. This is one the major advantage which DEM has over laboratory experiment because it is nearly difficult to compute the stress tensors in the laboratory.

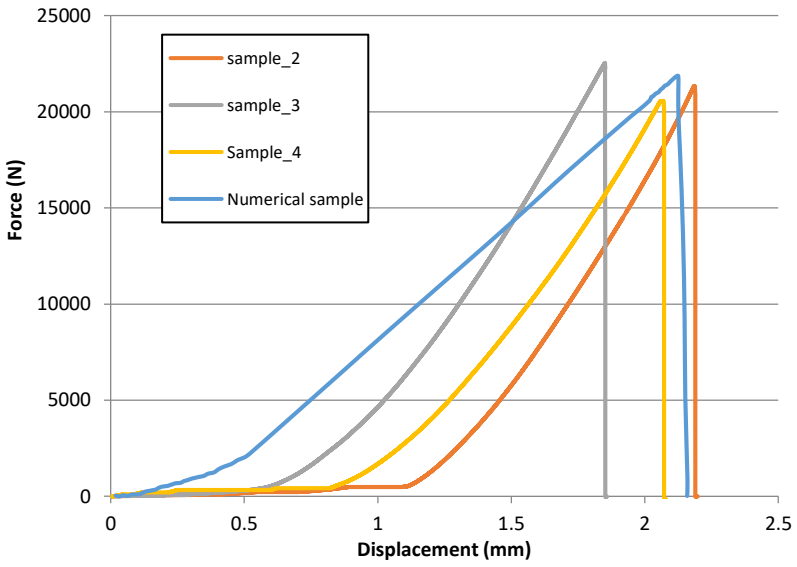

Figure 57: Validation of Numerical Simulation against experimental result of flexural test

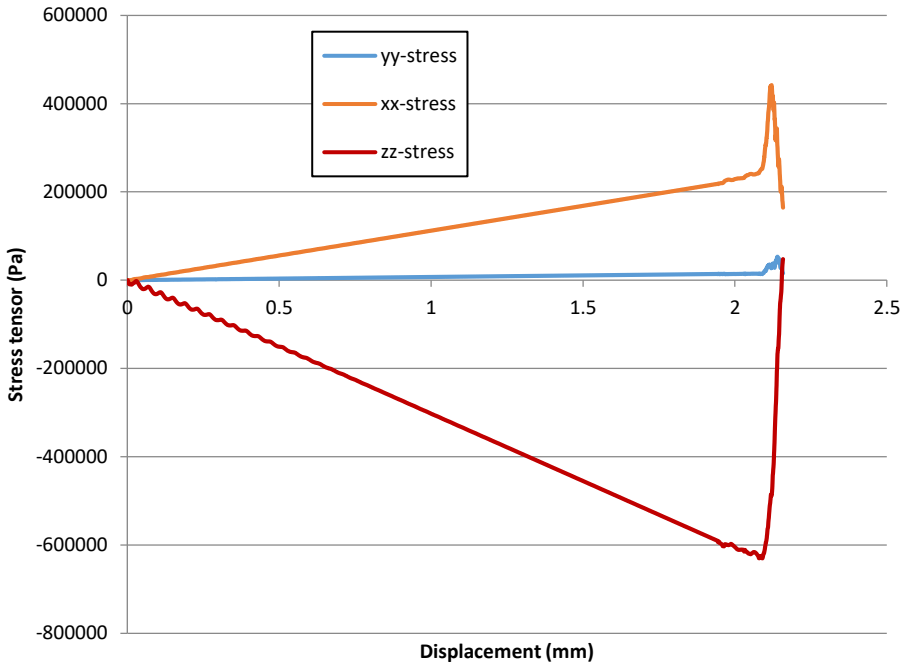

Figure 58: Stress tensor in xx, yy and zz direction

4.3.4.2 Crack pattern observation

The particular advantage of using DEM is that no crack elements are required to observe the evolution of cracking because they are discontinuous features which are an inherent part of this method. In other words, this means that a disruption of the bond between the spheres automatically induced a crack. Figure 59 and Figure 60 illustrate the fracture behaviour of the concrete beam in a three-point flexural test. It is clearly observed that that the cracking pattern is similar to the one observed in the laboratory. The crack starts to propagate as a line in the middle of the beam in an upward direction until the beam fails. This behaviour was observed in all the 3 samples of the experiment result which supports the numerical observation. However, it is hard to observed micro-cracks in experimental result with naked eyes. As such DEM is a great tool to study the initiation and propagation of micro-cracks which eventually coalesce to form macro-cracks. In addition to, it is possible for DEM to observe the crack propagation within the sample which shows that it is a non-destructive technique.

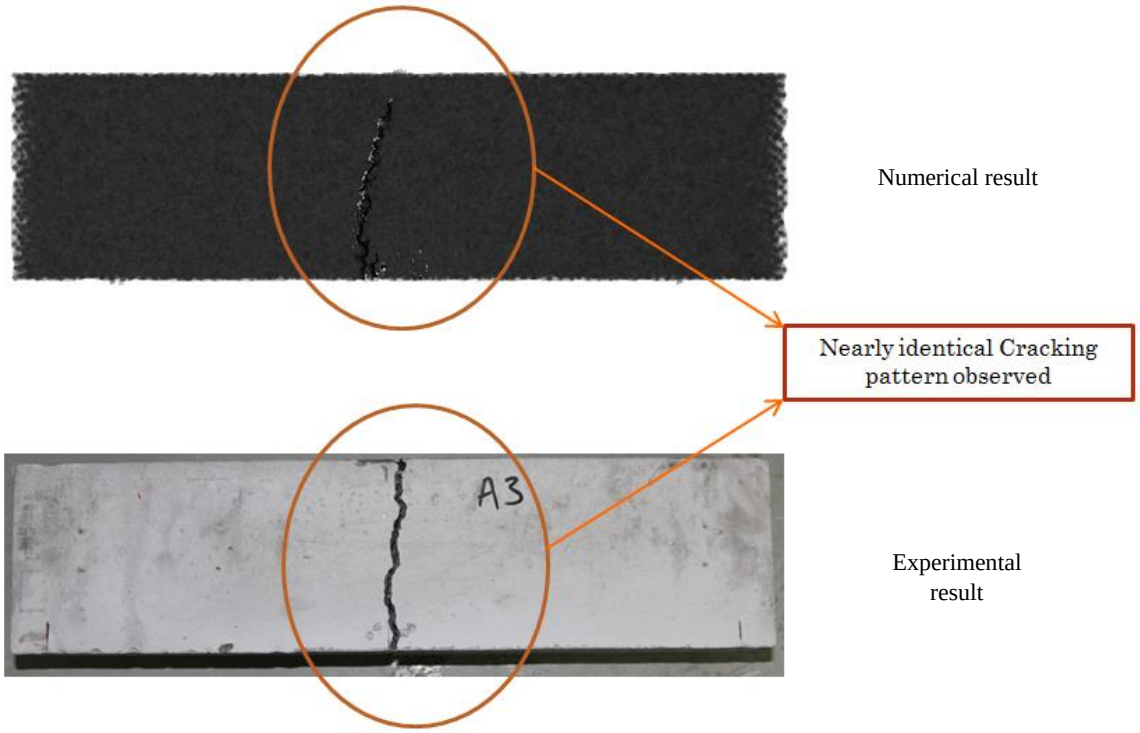

Figure 59: Crack pattern of DEM result from Experimental result (unreinforced Flexural test)

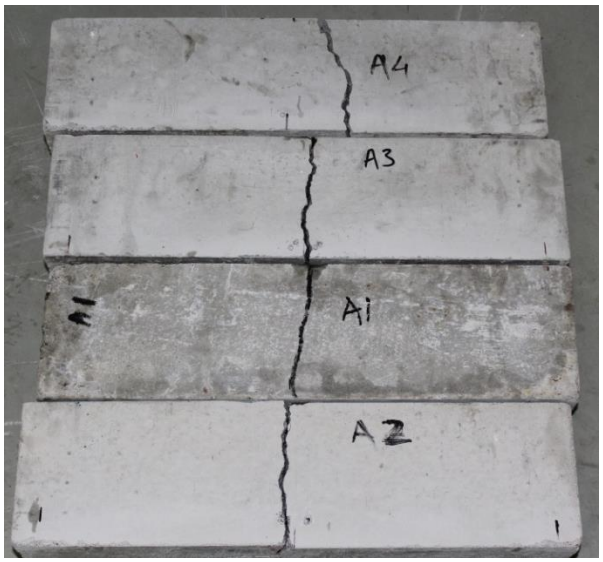

Experimental samples

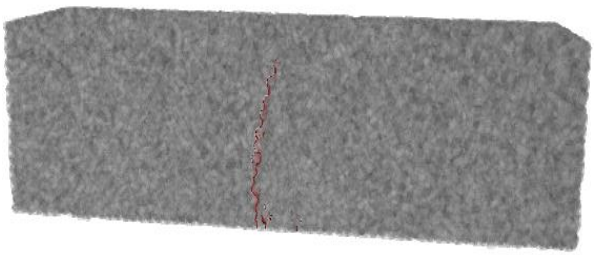

Numerical sample

Figure 60: Experimental result (all samples) and the numerical result (unreinforced flexural test)

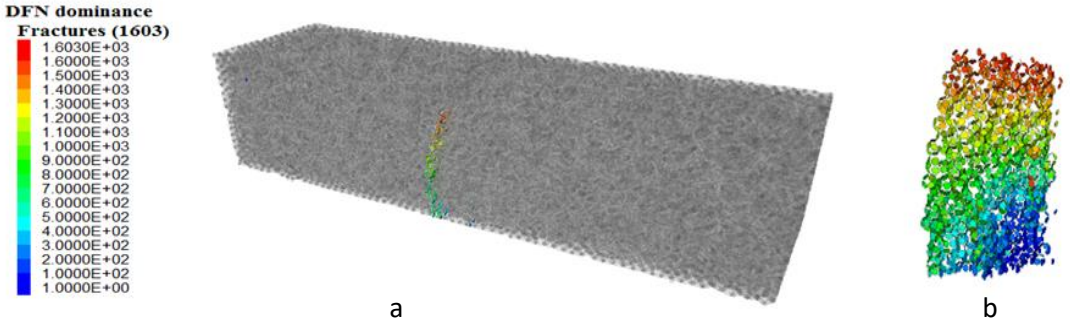

Figure 61: Crack dominance in flexural test (a) and Crack dominance within the sample (b)

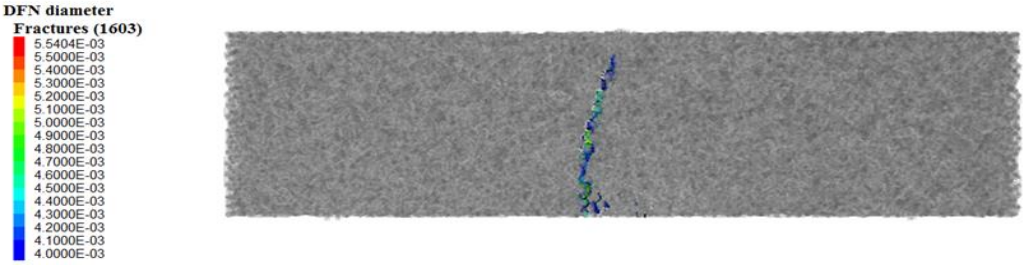

Figure 62: Crack Diameter in Flexural test

Discrete fracture networks (DFN) illustrates the cracking dominance. The cracking dominance is the path where the cracks are more prone to undertake on a scale where blue being less dominant and red being most dominant (see Figure 61a). The DFN cracking dominance scale clearly illustrates that cracking is propagating in an upward direction in the middle of the beam. Hence, it can be concluded the crack evolution observed in the numerical model is akin to the observation made in the laboratory experiment. Besides, in DEM, unlike laboratory experiment, it is difficult to observe the propagation of the crack within the sample without destroying the material. However, in DEM, it is possible to analyse the cracks propagation within the sample without damaging the whole structure as illustrated in Figure 61b. As such, it is possible to analyse which part of the concrete is more prone to the initiation of cracking. This is really an advantage in analysing the failure of complex building whereby the initiation of cracking which lead to disaster cannot be predicted. Moreover, under DFN, it is possible to measure the cracking opening diameter which

is difficult to obtain in the laboratory. It was observed as illustrated in Figure 62 that the cracking opening diameter that is formed in the unreinforced beam is between 4.0 mm to 5.1 mm.

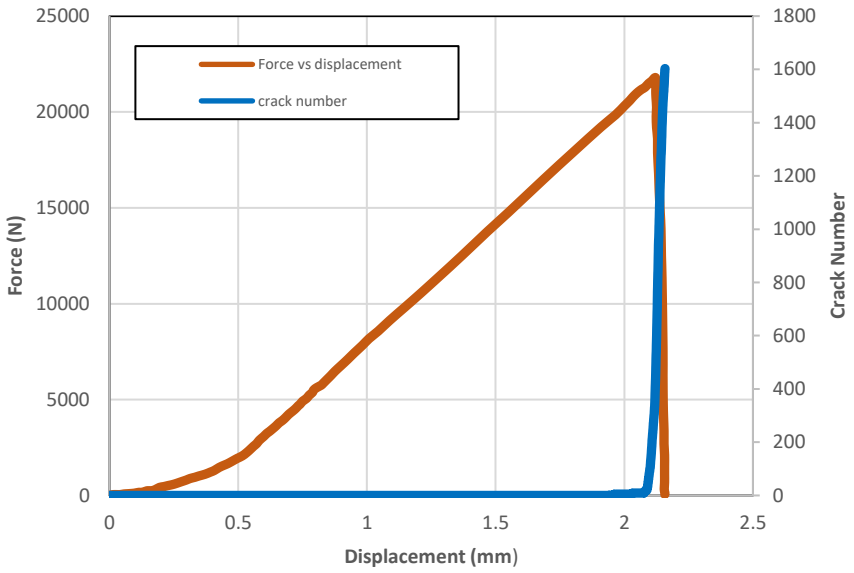

Figure 63: The progression of cumulative cracking number with force versus displacement (Flexural test)

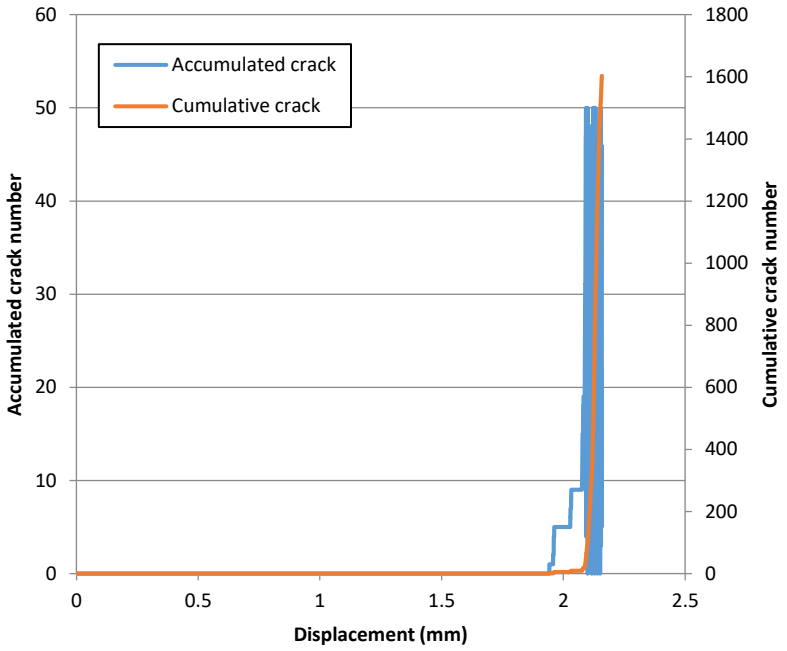

Figure 64: Accumulated crack and Cumulative crack

One thing about DEM is that particles which were not in contact before at the beginning can come into contact at later phase during the on-going damaging process. This can be a challenging process to identify the bond breakages which are leading to the initiation of crack. Hence, to solve this issue, the model consists of algorithms namely contact detection (see William and O'Conner, 1999) and discrete fracture network (DFN) which help to identify the formation of crack due bond breakage between the spheres was implemented in the programming code. The model starts analysing if there is any crack appearance due to bond breakage between the spheres right from the moment the load is applied as illustrated in Figure 64. Figure 63 illustrates the progression of the cumulative micro-cracks which are referred as the number of bond broken that will lead to an emergence of macroscopic crack. It is illustrated in Figure 63 that there is no crack initiated from the range of displacement 0 to 1.94 mm. However, beyond this displacement, as the beam is reaching its yielding phase cracks started to occur. At the yielding point, the crack number increases drastically and as the beam continues to fail, the cracks increase sharply. It is observed that there is a sharp increase in crack number and large crack accumulation beyond the displacement of 2.2 mm as illustrated in Figure 64. It was at this point where visible macroscopic cracks spread and coalesce to cause failure of the concrete beam. Hence, it can

be concluded that this DEM model can capture crack evolution and failure at microscopic scale in the study of a concrete in a three-point flexural test.

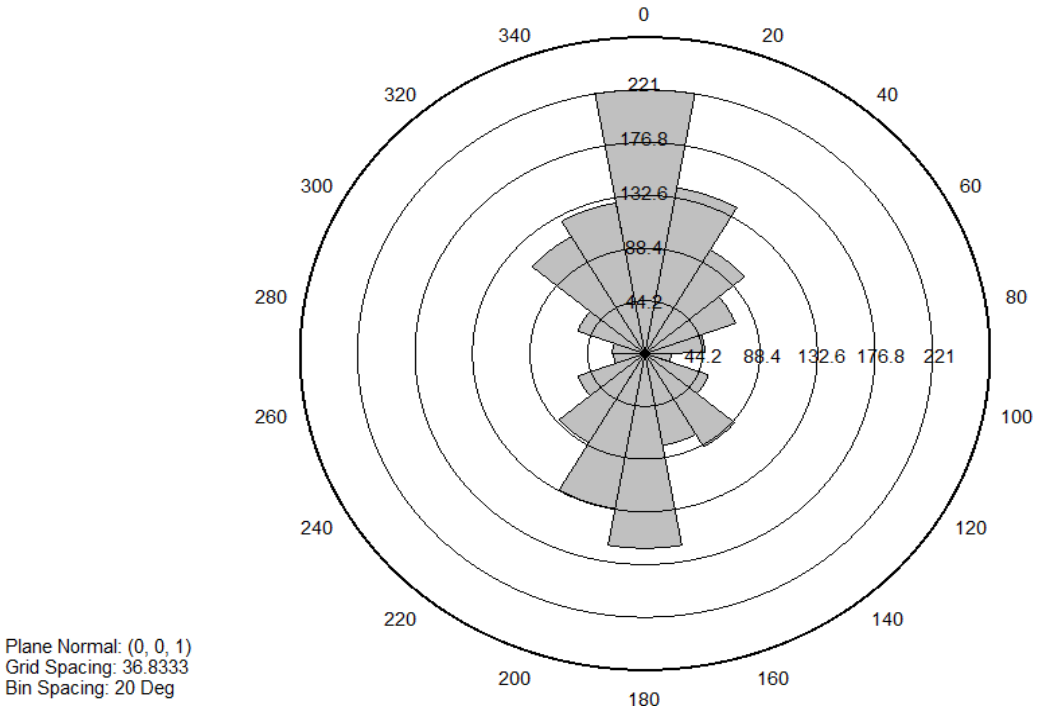

Figure 65: rosette plot shows the orientation of the cracks in a 3 point flexural test.

One of the important features with DEM which cannot be observed in the laboratory is the orientation of the propagation of the cracks. In this research, a rosette plot is used to display the orientation of cracks and the number of cracks at each particular angle respectively as illustrated Figure 65. This will help to identity which plane of the concrete requires much attention particularly useful in building where it is difficult to predict the initiation and propagation of cracks. It is observed in Figure 65 that the rosette plot shows the largest number of crack approximately 221, 141, 168 about $0°, 20°, 180°$ directions respectively in the x-z plane. Hence, the orientation in which the largest number of crack are 0° and $180°$. This matches the observation made in DFN whereby the cracks propagate as a line in an upward directly. Hence, this feature of DEM can help to improve the understanding of the relationship between the microscopic and macroscopic occurrences during failure which will be beneficial in designing concrete safety structure.

4.3.4.3 Energy Input and dissipation behaviour

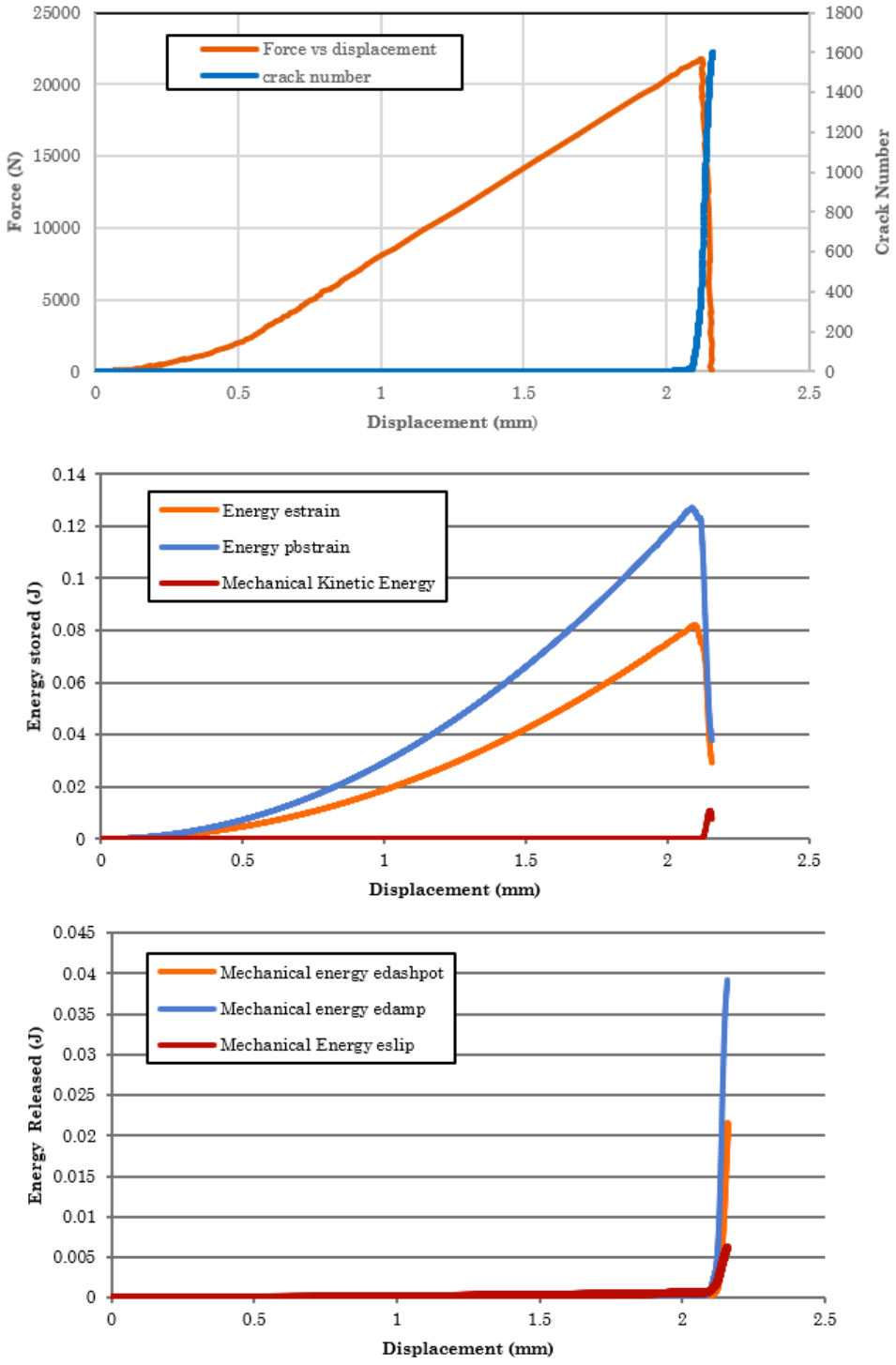

Figure 66: Energy stored and released into the system (flexural test)

DEM models unlike in the laboratory experiments can be used to investigate the evolution of energy input or dissipation behaviour throughout the on-going damage process. In this research, the mechanical response will be studied in term of energy form in order to better understand the salient response of the discrete particles in the model. This will help to show that DEM can indeed capture the micromechanics of concrete. The energy form that will be studied in this models is strain energy stored in all linear contact spring and parallel bond spring, kinetic energy of all entities in the assembly, frictional slip energy, energy of dashpot and local damping dissipation. The accumulated strain energy stored in both linear contact and parallel bond will be dissipated once the bonds between the particles are broken and the source of energy input to the system is the wall which provides the boundary condition.

Figure 66 illustrates the energy stored and released during the loading process whereby the evolution of various increment energy forms against the jack displacement is plotted. It is observed that the strain energy in term of the parallel bond and linear contact bond is increasing continuously due to the building up of elastic compression at the particles contacts caused by the increment of jack load. Upon reaching a displacement of 2.1 mm, the maximum strain energy that the linear contact spring can store is 0.081J and the maximum strain energy that the parallel contact spring can store is 0.122 J. Beyond the displacement of 2.1 mm after reaching a force of 20 KN, the strain energy stored in the parallel bond and linear contact bond decreases. This decrease in strain energy is due to the fact that energy is being dissipated in the form of kinetic energy, frictional slip energy, energy of the dashpot and local damping dissipation. This energy dissipation coincides with the bond breakage events whereby there is a significant increase in crack number. This confirms that there is a strong relationship between the energy dissipation and bond failure.

4.3.5 Summary

A three-point flexural test of unreinforced concrete beam was coded in three dimensional and it was modelled using discrete element method. The distribution of the particle in the numerical model was set according to the sieve analysis test but limited to coarse aggregate only due to limited computational power. The model was validated with the laboratory experiment. Upon validating the load versus displacement response of numerical result with the experimental result, it was observed there is a strong correlation between them. The comparison of both results is relatively good and the beam behaviour is well reproduced in DEM. However, further investigation is required Using a measurement sphere, it was possible to identify the stress tensor in xx, yy and zz plane. It is noted that in DEM, no crack elements are required to observe the evolution of

cracking because they are discontinuous features which are inherent part of this method. Also, this numerical model comprises of algorithms namely contact detection (see William and O'Conner, 1999) and discrete fracture network (DFN) which help to identify the formation of crack due bond breakage between the spheres and they were both implemented in the programming code. As such, upon comparing the cracking pattern in the numerical result against the experimental result, it was observed that they both are similar. With DEM model unlike laboratory experiment, it is possible to observe the path where the crack will propagate in term of cracking dominance. It is also possible to observe the cracking orientation that will help to identity which plane of the concrete requires much attention and this is particularly useful in building where it is difficult to predict the initiation and propagation of cracks.

Besides, the crack opening diameters can be also obtained from this DEM model. In this model crack opening diameters were between 4.0 mm to 5.1 mm. In laboratory, it is difficult to observe cracking propagation within the sample without destroying the sample itself. However, with DEM, the plane of cracking does not need to be specified and the formation of microcracking within the sample can be investigated without any inconvenience. It is also possible to observe at which displacement, the number of microcrack increases. This number of microcrack corresponds to the number of bond being broken. Also, the maximum strain energy stored which corresponds to the bond strength can be measured with DEM. Upon yielding which correspond to the largest number of cracks (bond broken) recorded, the energy is being dissipated in the form of kinetic energy, frictional slip energy, energy of the dashpot and local damping dissipation. In the future work, the programming code can be modified to compute fracture energy.

Thus, it can be concluded that the micromechanics information obtained from a DEM model can be really useful in complex building whereby it is difficult to predict the initiation and propagation of macro-cracking that will lead to failure. It is an undeniable fact that it is hard to mimic the behaviour of concrete in order to match perfectly the real scenario. Yet, in this research, DEM has proved that it can simulate a three-dimensional model of a flexural test of concrete whereby the results obtained are quite promising.

4.4 Steel reinforced four-point flexural test

4.4.1 Three-dimensional sample assembly

It is very important to mock the test specimen in order to accurately model its salient behaviour. A three-dimensional sample, unlike a two-dimensional sample, can model the global behaviour of the beam. As such, a four-point steel reinforced flexural test is represented as an assembly of spherical particles confined in a cuboid system whereby linear contact bond together with parallel bond is installed within the system as illustrated in Figure 67. The coding of the model was developed using Fish programming language (refer to **Appendix A.3**) and run using the program PFC 3D. The model was built with a height of 120 mm, width 60 mm and length 1600 mm. Steel reinforcement was modelled using lines of spheres of diameter equal to Main Steel bars: 8mm, Top Steel bars: 6mm and Stirrup: 6 mm. The steel reinforcement is bonded using the linear contact bond. A number of 67172 discrete spherical elements are used to model the concrete steel reinforced beam. Four cylinders are used to apply the boundary conditions. The top two cylinders are used to apply the loading condition whilst the other two cylinders act as support. However, ITASCA, (2003) mentioned that the walls which are intersecting each other are not an issue because the wall interacts only with the balls, not with one another.

The integration of the steel rebar into the matrix of the sample requires three interactions to be defined namely concrete spheres' interaction, steel spheres' interaction and steel-concrete spheres' interaction. The calibration of the parameter and concrete spheres' interaction follows the same behaviour as defined in the unreinforced flexural test. The steel is calibrated so that they exhibit an elastic-perfectly plastic behaviour. The concrete-steel interaction according to Hentz et al., (2009) is identical to steel ones which are consistent with pull-out observations. The parameters used to conduct this numerical analysis are tabulated in Table 4.

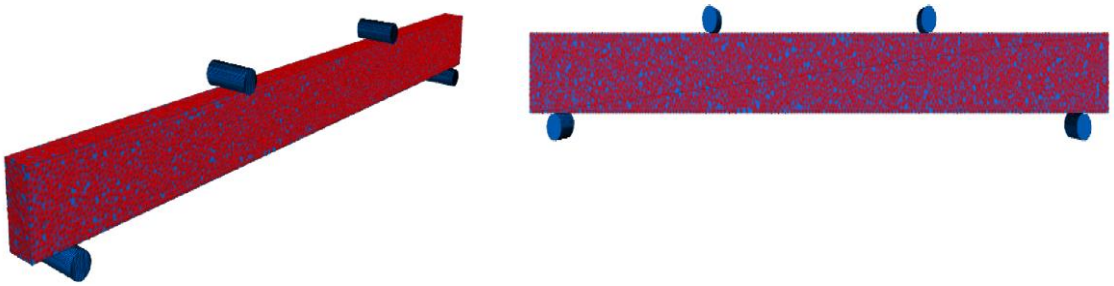

Figure 67: Particle assembly with linear contact bonds and Parallel Bond (Steel reinforced flexural test)

Moreover, the size of aggregate used in this numerical model of a four-point steel reinforced flexural test is based on the actual particle size distribution obtained from the sieve analysis test conducted in the laboratory. An algorithm coded using fish programming was developed in order to represent the realistic particles size distribution as illustrated Figure 68. As such, this numerical model mimics the realistic particle size distribution based on result from the sieve analysis. Figure 68 illustrates the gradation of the particles in the experiment (green line) and gradation of the particles in numerical model (red line). The developed algorithm tries different configurations to place the spheres into the cylinder until it matches the correct gradation of the particles based on the laboratory result. However, due to the limitation of the computational power of the workstation available, this model doesn't encompass fine aggregates and is limited to coarse aggregates only.

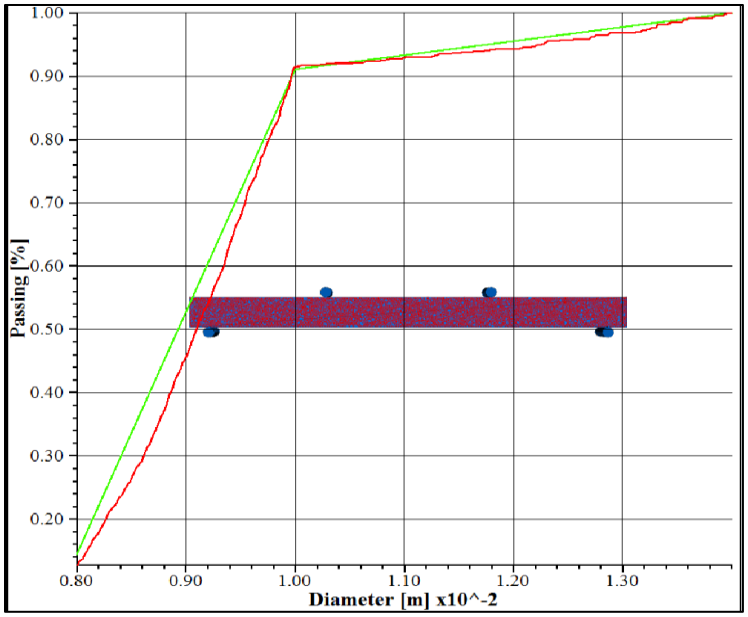

Figure 68: Gradation of particles in steel reinforced flexural test

4.4.2 Calibration of parameters

It is necessary to calibrate the model parameters in order to adjust the material properties in the assembly of discrete particles. The elastic macroscopic properties for instance Young's modulus, E and Poisson's ratio, υ are the input parameters for the model. The local stiffnesses that are derived from the macroscopic properties are given by the 'Micro-Macro' relationship. These 'Micro-Macro' relationship developed by Liao et al. (1997) which linked those local stiffness are given by homogenized models used for homogenized model in regular assemblies; however, they have been modified to represent the disordered assemblies (see equation 1 and 2).

$$E = \frac{D_{eq}}{S_{int}} k_n \frac{\left(\beta + \gamma \frac{k_s}{k_n}\right)}{\left(\alpha + \frac{k_s}{k_n}\right)} \tag{3.5}$$

$$\upsilon = \frac{\left(\beta + \gamma \frac{k_s}{k_n}\right)}{\left(\alpha + \frac{k_s}{k_n}\right)} \tag{3.6}$$

where;

D_{eq}: Initial distance between particles

$S_{inter} = \min(\pi R_a^2, \pi R_b^2)$

α, β, γ: Parameters related to the radius of interaction between particles (Rousseau, 2009)

The integration of the steel rebar into the matrix of the sample requires three interactions to be defined namely concrete spheres' interaction, steel spheres' interaction and steel-concrete spheres' interaction. The calibration of the parameter and concrete spheres' interaction follows the same behaviour as defined in the unreinforced flexural test. The steel is calibrated so that they exhibit an elastic-perfectly plastic behaviour. In addition to, the concrete-steel interaction according to Hentz et al., (2009) is identical to steel ones which are consistent with pull-out observations. The input parameters for the steel reinforced flexural test are tabulated in Table 4.

Table 4: Parameters for steel reinforced flexural test

Parameter	E (Gpa)	ν	C(Mpa)	T(Mpa)	Φ	Density (kg/m3)
Concrete	30	0.2	10.5	3	20	2500
Steel	210	0.25	33.4	500	0	8050

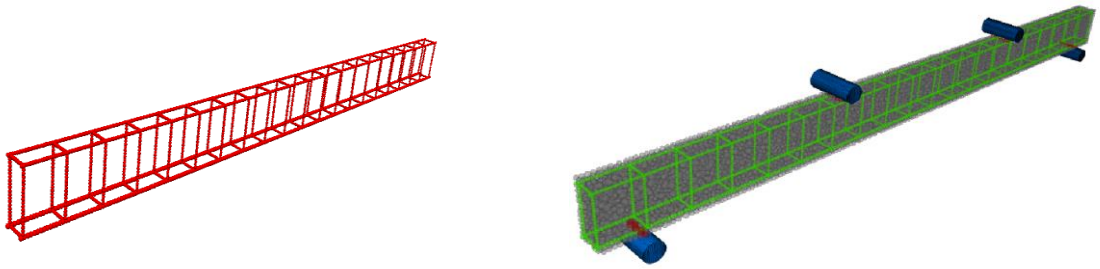

Figure 69: Steel rebar installed in the beam

4.4.3 Result and Discussion

The laboratory experiment was not conducted due to time constraint in the timeframe of the MPhil. However, the laboratory experiment of Hentz et al., (2009) was used to validate the numerical result. The validation was achieved after several iterations steps in order to calibrate the

parameters. The result obtained from both experiment and numerical results are validated as illustrated in Figure 70. It is observed from the numerical result obtained in term of force versus jack displacement is almost similar to the one obtained from the experimental results. The elastic phase of the numerical result matches those of the experimental result. It is observed that the numerical yield slightly before the experimental result. This could due to the fact that the stiffness of the model is high due to low softening. This can be overcome by using high local softening in the model to counterbalance the free rotations of the sphere and thus, which will retard the yielding concrete. This discrepancy with the experimental result unlike in other researchers' work for instance, (Hentz et al., 2009, Rousseau et al., 2007, Shui et al., 2009 and Azeyedo et al., 2006) is that this model comprises of a large number of spheres (67172 discrete spherical elements) which can increase its complexity. Besides, the shape of the aggregates used in PFC 3D is spherical unlike in the real scenario which could be another reason for discrepancy between the two results (Numerical and Experimental). However, due to the limitation of the computation power available in XJTLU, it was not possible to use discrete fracture network (DFN) to record cracking. Nevertheless, based on the result obtained, it can be concluded that discrete element modelling can be used to study steel reinforced concrete under a flexural test.

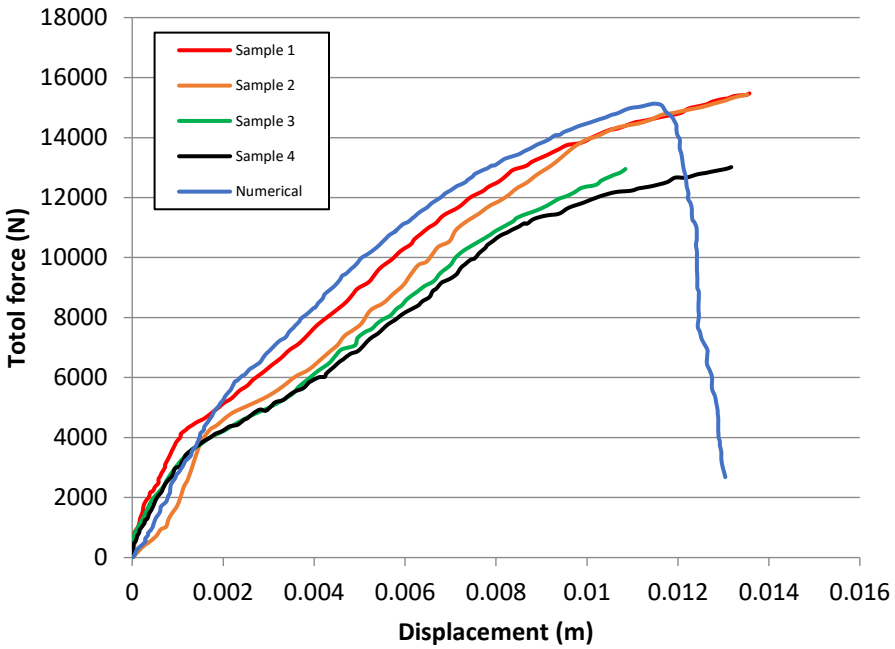

Figure 70: Force versus displacement (Steel reinforced concrete)

4.4.4 Summary

In this model, a concrete beam was modelled together with the introduction of reinforcement (main bar, top bar and stirrup). The distribution of the particle was set according to the sieve analysis test and the model was validated by the laboratory experiment. It was observed that the numerical result obtained shows a strong correlation with the experiment result. However, due to the limited computational power of the workstation available, it was not possible to observe the cracking pattern. Nevertheless, in the future, with better computational power, DEM can help us to study the inner damage. Yet, it can be concluded that DEM is still capable of simulating the behaviour of steel reinforced concrete under a four-point flexural test.

Chapter 5. Conclusions

In this study, three-dimensional numerical models were programmed using fish programming language to study the mechanical behaviour of concrete. The numerical models coded are namely, a uniaxial compressive test of concrete cylinder, three-point flexural test of unreinforced concrete beam and four-point flexural test of steel reinforced concrete beam. The codes were run on a computer program namely PFC3D. This chapter will sum up the main conclusions derived from this thesis and also provides recommendation for future work in this research area.

All the numerical modelling, for instance, discrete element modelling which is used in this project are developed from mathematical models which are based on the assumptions to an approximate reality. Thus, these assumptions made for mathematical simplicity compromise on the precision to represent the real scenario of the material behaviour. For instance, in DEM, a sphere is assumed to be non-deformable and this is not the case at high stresses. Thus, it is important to understand that numerical simulations are meant for the understanding of real scenario.

The main findings of this research are summarised below:

- The stress-strain response of the uniaxial compressive test shows good correlation with the laboratory experiment which confirms the model is good enough to simulate the behaviour of concrete.
- The force-displacement response of the three-point flexural test of unreinforced concrete is relatively good in contrast with the experimental result. A measurement sphere was created around the crack propagation region using fish programming language in order to study the stress tensors evolution in the xx, yy and zz planes. It should be noted that stress tensor cannot be measured directly in the laboratory. From the result obtained, it was observed that the stress developed in the zz plane is higher than the other planes; thus, predicting that this plane will account for higher number of crack. From the laboratory result, it was deduced that this prediction made from the model was indeed correct. Hence, this proves the validity and efficiency of DEM model.
- Also, the cracking pattern (in term of the initiation and propagation) observed in both numerical result (Uniaxial compressive test and the flexural test of plain concrete) is similar to the one observed in the laboratory test. One distinct feature of this model is that the formation of micro crack can be observed within the sample without destroying it and this

not possible in the laboratory. It is concluded that the qualitative analysis observed from 3D numerical models have a strong correlation with the laboratory observation.

- The models consist of algorithms namely contact detection (see William and O'Conner, 1999) and discrete fracture network (DFN) which help to identify the formation of crack due bond breakage between the spheres was implemented in the programming code. The model starts analysing if there is any crack appearance due to bond breakage between the spheres right from the moment the load is applied. Hence, it can be concluded that this DEM model can capture crack evolution and failure at microscopic scale in the study of a concrete
- DEM can illustrate cracking dominance which is the path where the cracks are more prone to undertake on a scale (blue being less dominant and red being most dominant). This help to track the path the cracks are undertaking. It is also possible to measure the average cracking opening diameter which was 4.0 mm to 5.1 mm (unreinforced concrete flexural test) and 4.0 mm to 5.0 mm (uniaxial compressive test). It is also possible to generate a rosette plot which displays the orientation of cracks and the number of cracks at each particular angle respectively. This will help to identity which plane of the concrete requires much attention particularly useful in building where it is difficult to predict the initiation and propagation of cracks.
- Fracture could be studied from an energy point of view in DEM. DEM models unlike in the laboratory experiments can be used to investigate the evolution of energy input or dissipation behaviour throughout the on-going damage process. For instance, it is possible to measure the overall strain energy in the linear contact bond and parallel bond. Upon yielding, this stored energy is released in the form of kinetic energy, frictional slip energy, Energy of dashpot, local damping. As such, DEM can be used to compute fracture energy in the future.
- The steel reinforced concrete under four-point flexural test was modelled. The main reinforcement bars, top bars and the stirrup were all made with discrete element particles connected by linear contact bond. The numerical result was validated with the experimental result conducted by Hentz et al., (2009). It was observed that force-displacement response obtained from the numerical result shows a strong correlation with the laboratory result. However, due to the limitation of the computational power of the workstation available, it was not possible to observe the crack initiation and propagation.
- It was concluded that DEM is capable of representing the qualitative and quantitative behaviour of concrete which is heterogeneous in nature.

Further works

It should be noted that the shape of the particle used in this research is only spherical and the real aggregate shape is much more complex. Thus, clumps which also a feature of DEM should be used to bond more particles together in order to create more realistic shape of the aggregate. As future works, the influence of concrete behaviour with different aggregates shapes at different angularity should be studied. Also, the effect of different cement types with different specimen's geometries should be addressed in the future. Moreover, DEM assumes that the spheres are non-deformable but at high stresses deformation in term of crushing, may occur. Thus, as future works, the numerical model should take into consideration the crushing effects of the discrete particles.

XJTLU Civil engineering lab is not fully equipped with sophisticated equipment, for instance, X-ray tomography, digital image correlation and infrared thermography. These equipment will provide a better understanding and observation which can be compared and validated with the DEM models. For instance, Digital image correlation (DIC) coupled with a digital single lens reflex (DSLR) camera will help to analyse the full-field fracture behaviour. Also, infrared thermography can be used to measure the energy released during fracture and this can be validated with the DEM model from an energy point of view. As such, in the future, these equipment could be coupled with the numerical models created to gain a profound understanding of fracture behaviour.

The steel reinforced beam model created could be used in the future to model the behaviour of steel reinforced concrete beam under an impact load. Also, this model could also be modified to integrate steel fibre in order to study the fracture behaviour of steel fibre reinforced concrete. Moreover, the concrete cylindrical model under uniaxial load created could be modified to study the behaviour of concrete filled steel tube.

References Cited

1. "Particle Flow Code in Three Dimensions, Theory and Background." Minnesota: Itasca Consulting Group Inc. 2003.
2. "Particle Flow Code in Three Dimensions, User's Guide", Minnesota: Itasca Consulting Group Inc. 2003.
3. Aassved Hansen, E., 1995. Determination of the Tensile Strength of Concrete. *NORDIC CONCRETE RESEARCH-PUBLICATIONS-*, *17*, pp.1-17.
4. Abbasnia, R. and Aslami, M., 2015. Numerical simulation of concrete fracture under compression by explicit discrete element method. *International Journal of Civil Engineering*, *13*(3), pp.245-254.
5. Abdollahi, A. "Investigation of objectivity in the application of the FEM to RC structures—II." *Computers & structures* 58.6 (1996): 1183-1211.
6. Abdollahi, A., 1996. Numerical strategies in the application of the FEM to RC structures—I. *Computers & structures*, *58*(6), pp.1171-1182.
7. ACI Report 446.3 R-97.,(1997). Finite element analysis of fracture in concrete structures: state-of-the-art, reported by ACI Committee 446.
8. Adams, D.J. and Matheson, A.J., 1972. Computation of dense random packings of hard spheres. The Journal of Chemical Physics, 56(5), pp.1989-1994.
9. Allen, M.P. and Tildesley, D.J., 1989. Computer simulation of liquids. Oxford university press.
10. Ammeri, A., Jamei, M., Bouassida, M., Ple, O., Villard, P. and Gourc, J.P., 2009. Numerical study of bending test on compacted clay by discrete element method: tensile strength determination. *International Journal of Computer Applications in Technology*, *34*(1), pp.13-22.
11. Atkinson, B.K., 1987. Introduction to fracture mechanics and its geophysical applications. Fracture mechanics of rock, pp.1-26.
12. Azevedo, N.M., de Lemos, J.V. and de Almeida, J.R., 2006. A Discrete Element Model For The Fracture Analysis of Reinforced Concrete. In *III European Conference on Computational Mechanics* (pp. 104-104). Springer, Dordrecht.
13. Bagi, K.: Stress and strain in granular assemblies. Mech. Mater. 22(3), 165–177 (1996)
14. Bardet J-P. (1998) 'Introduction to computational granular mechanics', in *Behaviour of granular materials*, Cambou B.(ed.), No. 385 in CISM Courses and Lectures. Springer: Wien, New York, pp.99-170.
15. Bathe, K.J. and Wilson, E.L., 1976. Numerical methods in finite element analysis.
16. Bathurst R.J. and Rothenburg L. (1988), 'Micromechanical aspects of isotropic granular assemblies with linear contact interaction', *Journal of Applied Mechanics*, vol. 55, pp. 17-23.
17. Bazant, Z.P. and Planas, J., 1997. *Fracture and size effect in concrete and other quasibrittle materials* (Vol. 16). CRC press.
18. Bazant, Z.P., Jirasek, M., 1994. Nonlocal model based on crack interactions: a localization study. Journal of Engineering Materials and Technology ASME 116, pp.256–259.
19. Beasman, L.E. and McCuen, R.H., 2011. Estimating the distribution of air voids in concrete. *Civil Engineering Dimension*, *13*(1), pp.15-20
20. Beckmann, B., Schicktanz, K., Reischl, D. and Curbach, M., 2012. DEM simulation of concrete fracture and crack evolution. *Structural Concrete*, *13*(4), pp.213-220.
21. Bezrukov, A., Stoyan, D. and Bargiel, M., 2001. Spatial statistics for simulated packings of spheres. Image Anal. Stereol, 20, pp.203-206.
22. Blumenfeld, S. M., & Glover, G. (1981). Spatial resolution in computed tomography. Radiology of the Skull and Brain, 5, pp.3918-3940.
23. Bolander, J.E. and Sukumar, N., 2005. Irregular lattice model for quasistatic crack propagation. *Physical Review B*, *71*(9), p.094106.

24. Bolander, J.E., Saito, S., 1997. Discrete modeling of short-fiber reinforcement in cementitious composites. Advanced Cement Based Materials 6, pp.76–86.
25. Bossi, R. H., Cooprider, K. K., & Georgeson, G. E. (1990). X-ray computed tomography of composites. BOEING AEROSPACE AND ELECTRONICS CO SEATTLE WA.
26. Broberg, K.B., 1999. Cracks and fracture. Academic Press
27. BS 812: Part 109, 1990. Methods for determination of moisture content. British Standards Institution, London, United Kingdom.
28. Caballero, A., Carol, I. and Lopez, C.M., 2006, March. New results in 3d meso-mechanical analysis of concrete specimens using interface elements. In *Computational Modelling of Concrete Structures, EURO-C* (pp. 43-52).
29. Calvetti F., Combe G. and Lanier J. (1997), 'Experimental micromechanical analysis of a 2D granular material: relation between structure evolution and loading path', *Mechanics of Cohesive–Frictional Materials*, n°2, pp.121-163.
30. Calvetti, F., R. Nova, and R. Castellanza (2004). Modelling the subsidence induced by degradation of abandoned mines. In Continuous and discontinuous modelling of cohesive frictional materials, Number 137148. Taylor and Francis Group.
31. Cambou B., Dubujet P., Emeriault F. and Sidoroff F. (1995) 'Homogenization for granular materials', *Eur. J. Mech., A/Solids*, vol. 14, n°2, pp. 255-276.
32. Carlesso, M.V., 2008. The Foaming Behavior of Alkane Emulsified Ceramic Suspension: From LAPES to HAPES. *Engineering of Materials*.
33. Carol, I., López, C.M. and Roa, O., 2001. Micromechanical analysis of quasi-brittle materials using fracture-based interface elements. *International Journal for Numerical Methods in Engineering*, *52*(1-2), pp.193-215
34. Catherine O.S., Jonathan D. B. and Shaofan L. (2003), 'A new approach for calculating strain for particulate media', *Int. J. Numer. Anal. Meth. Geomech.*, n° 27, pp. 859–877.
35. Chang, C.S., Wang, T.K., Sluys, L.J., van Mier, J.G.M., 2002. Fracture modeling using a micro-structural mechanics approach – part I: theory and formulation. Engineering Fracture Mechanics 69, pp.1941–1958.
36. Chang, C.T., Monteiro, P., Nemati, K. and Shyu, K., 1996. Behavior of marble under compression. *Journal of materials in civil engineering*, *8*(3), pp.157-170.
37. Chang, F.H., Drake, T.E., Osterkamp, M.A., Prowant, R.S., Monchalin, J.P., Heon, R., Bouchard, P., Padioleau, C., Froom, D.A., Frazier, W. and Barton, J.P., 1993. Laser ultrasonic inspection of honeycomb aircraft structures. In *Review of Progress in Quantitative Nondestructive Evaluation* (pp. 611-616). Springer, Boston, MA.
38. Chen, J., Wang, L.B. and Huang, X.M., 2012. Micromechanical modeling of asphalt concrete fracture using a user-defined three-dimensional discrete element method. *Journal of Central South University*, *19*(12), pp.3595-3602.
39. Chen, Y.-C and H.Hung (1991). Evolution of shear modulus and fabric during shear deformation. Soils and Foundations 31 (4), 148-160.
40. Chen, Y.-C and I. Ishibashi (1990). Dynamic shear modulus and evolution of fabric of granular materials. Soils and Foundations 30(3), 1-10.
41. Cheung, G. (2010). Micromechanics of sand production in oil wells. Ph.D. Thesis, Imperial College London.
42. Cho, N. A., Martin, C. D., & Sego, D. C. (2007). A clumped particle model for rock. *International Journal of Rock Mechanics and Mining Sciences*, *44*(7), pp.997-1010.
43. Christensen, R.M., Lo, K.H., 1979. Solutions for effective shear properties in three phase sphere and cylinder models. Journal of Mechanics in Physics and Solids 27, pp.315–330.
44. Christoffersen, J., Mehrabadi, M.M. and Nemat-Nasser, S., 1981. A micromechanical description of granular material behavior. Journal of Applied Mechanics, 48(2), pp.339-344.

45. Code, E., 2004. 2, Design of concrete structures-Part 1-1: General rules and rules for buildings, BS EN 1992-1-1: 2004. British Standards (BSi).
46. Colliat-Dangus, J. L., Desrues, J., & Foray, P. (1988). Triaxial testing of granular soil under elevated cell pressure. In Advanced triaxial testing of soil and rock. ASTM International.
47. Collop, Andy, G. R. McDowell, and Y. Lee. "Modelling the behaviour of an idealised asphalt mixture using the distinct element method." (2004).
48. Constantinides G, Ulm FJ (2004) The effect of two types of C–S–H on the elasticity of cement-based materials: Results from nanoindentation and micromechanical modeling. Cem Concr Res 34:67–80.
49. Constantinides G, Ulm FJ, Vliet KV (2003) On the use of nanoindentation for cementitious materials. Mater Struct 36:191–196.
50. Cundall P. A. (1971). "A computer model for simulating progressive large scale movements in blocky rock systems." Proc. Symp. Int. Soc. for Rock Mech.
51. Cundall, P. A. and Strack, O. D. L.(1983). Modeling of microscopic mechanisms in granular material. Micromechanics of granular materials: New Models and Constitutive Relations, Jenkins and Satake (Eds), Elsevier Science Publishers, Amsterdam, Netherlands, 137-149.
52. Cundall, P. and O.Stacks (1979a). A discrete numerical model for granular assemblies. Geotechnique 29(1), 47-65.
53. Cundall, P.A. and Hart, R.D., 1992. Numerical modelling of discontinua. Engineering computations, 9(2), pp.101-113.
54. Cundall, P.A. and Strack, O.D.L. (1978) The Distinct Element Method as a Tool for Research in Granular Media, Report to the National Science Foundation Concerning NSF Grant ENG76-20711, Part I
55. Cundall, P.A. and Strack, O.D.L. (1979b) The Distinct Element Method as a Tool for Research in Granular Media, Report to the National Science Foundation Concerning NSF Grant ENG76-20711, Part II
56. Cusatis, G., Bazant, Z.P. and Cedolin, L., 2003. Confinement-shear lattice model for concrete damage in tension and compression: II. Computation and validation. *Journal of Engineering Mechanics*, *129*(12), pp.1449-1458.
57. DAI Q L, YOU Z P. (2007) Prediction of creep stiffness of asphalt mixture with micromechanical finite-element and discrete-element models [J]. Journal of Engineering Mechanics, 2007, 133(2): 163−169.
58. Dedecker F., Chaze M., Dubujet P. and Cambou B. (2000), 'Specific features of strain in granular materials', *Mechanics of Cohesive-Frictional Materials*, n° 5, pp. 173-193.
59. Delaney, G., S. Inagaki, and T.Aste (2007). Fine tuning DEM simulations to perform virtual experiments with three dimensional granular packings. In Y. Ate, T.Di Matteo, and A. Tordesillas (Eds.), Granular and Complex Materials, pp. 141-168. World Scientific.
60. Desrues, J., Chambon, R., Mokni, M., & Mazerolle, F. (1996). Void ratio evolution inside shear bands in triaxial sand specimens studied by computed tomography. Géotechnique, 46(3), pp.529-546.
61. Diamond S (2004) The microstructure of cement paste and concrete—a visual primer. Cem Concr Compos 26:919–933.
62. Döge, G., 2001. Perfect simulation for random sequential adsorption of d-dimensional spheres with random radii. Journal of Statistical Computation and Simulation, 69(2), pp.141-156.
63. Duran, J. (2000). Sands, powders and grains: An introduction to the physics of granular materials. New York: Springer.
64. Einstein, A., 1911. Eine neue bestimmung der molekuldimensionen. Annalen der Physik 34, pp. 591–592.
65. Elkadi, A.S. and Van Mier, J.G.M., 2006. Experimental investigation of size effect in concrete fracture under multiaxial compression. *International journal of fracture*, *140*(1-4), p.55.
66. EN, B., 2009. 12390-6 (2009) "Testing Hardened Concrete. Tensile Splitting Strength of Test Specimens". *British Standard Institution, London*.
67. Engelder, T., 1987. Joints and shear fractures in rock. Fracture mechanics of rock, pp.27-69.
68. Fakhimi, A., J. Riedel, and J.F. Labuz (2006). Shear banding in sandstone: Physical and numerical studies. International Journal of Geomechanics 6(3), 185-194.

69. Gitman, I.M., Askes, H. and Sluys, L.J., 2008. Coupled-volume multi-scale modelling of quasi-brittle material. *European Journal of Mechanics-A/Solids*, *27*(3), pp.302-327.
70. Gitman, I.M., Askes, H. and Sluys, L.J., 2008. Coupled-volume multi-scale modelling of quasi-brittle material. *European Journal of Mechanics-A/Solids*, *27*(3), pp.302-327.
71. Gopalakrishnan, K., Ceylan, H. and Inanc, F., 2007. Using X-ray computed tomography to study paving materials. *Construction Materials*, *160*(1), pp.15-23.
72. Griffith, A.A., 1921. The phenomena of rupture and flow in solids. Philosophical transactions of the royal society of london. Series A, containing papers of a mathematical or physical character, 221, pp.163-198.
73. Griffith, A.A., 1921. The phenomena of rupture and flow in solids. Philosophical transactions of the royal society of london. Series A, containing papers of a mathematical or physical character, 221, pp.163-198.
74. Gutierrez, G.A. (2007). Influence of late cementation on the behavior of reservoir sands. Ph.D. thesis, Imperial College London.
75. GYURKÓ, Z., BAGI, K. & BOROSNYÓI, A. 2014. Discrete element modelling of uniaxial compression test of hardened concrete. *Építöanyag (Online)***,** 113.
76. Haeri, H., & Sarfarazi, V. (2016). Numerical simulation of tensile failure of concrete using Particle Flow Code (PFC). *Computers and Concrete*, *18*(1), pp.39-51.
77. Hashin, Z., 1965. Viscoelastic behaviour of heterogeneous media. Journal of Applied Mechanics ASME 9, pp.630–636.
78. Hemalatha, T., Ramaswamy, A. and Kishen, J.C., 2015. Micromechanical analysis of self compacting concrete. Materials and Structures, 48(11), pp.3719-3734.
79. Hentz, S., Daudeville, L. and Donzé, F., 2003, July. Modeling of reinforced concrete structures subjected to impacts by the discrete element method. In *Proc. 16th ASCE Engineering Mechanics Conference*.
80. Hentz, S., Daudeville, L. and Donzé, F.V., 2004. Identification and validation of a discrete element model for concrete. *Journal of engineering mechanics*,*130*(6), pp.709-719.
81. Hentz, S., Daudeville, L., & Donzé, F. V. (2009). Discrete Element Modeling of a Reinforced Concrete Structure. *Journal of the Mechanical Behavior of Materials*, *19*(4), pp.249-258
82. Hentz, S., Donzé, F.V. and Daudeville, L., 2005. Discrete elements modeling of a reinforced concrete structure submitted to a rock impact. *Italian Geotechnical Journal*, *39*(4), pp.83-94.
83. Hentz, S., Daudeville, L. and Donzé, F., 2002, June. Discrete element modelling of concrete and identification of the constitutive behaviour. In *The 15th Engineering Mechanics Division Conference*.
84. Herrmann H. J., "Intermittency and self-similarity in granular media", Powders & Grains 97, Balkema, Rotterdam, 1997.
85. Herrmann, H.J., Hansen, A. and Roux, S., 1989. Fracture of disordered, elastic lattices in two dimensions. *Physical Review B*, *39*(1), p.637.
86. Hillerborg, A., Modéer, M. and Petersson, P.E., 1976. Analysis of crack formation and crack growth in concrete by means of fracture mechanics and finite elements. Cement and concrete research, 6(6), pp.773-781.
87. Hinrichsen H., Wolf D. E. (2004), The Physics of Granular Media, Wiley VCH, Weinheim, Germany, 2004.
88. Hirsh, T.J., 1962. Modulus of elasticity of concrete affected by elastic modulus of cement paste matrix and aggregate. Journal of the American Concrete Institute 59 (3), pp.427–452.
89. Hoagland, R.G., Hahn, G.T. and Rosenfield, A.R., 1973. Influence of microstructure on fracture propagation in rock. Rock Mechanics and Rock Engineering, 5(2), pp.77-106.
90. Igarashi S, Bentur A, Mindess S (1996) Microhardness testing of cementitious materials. Adv Cem Based Mater 4:48–57
91. Irwin, G.R. (1958). Fracture. In: Handbuch der Physik. Springer Verlag, Berlin, Vol. 6.
92. Itasca (2004). PFC2D 3.10 Particle Flow Code in Two Dimensions, Theory and Background volume (Third ed.). Minneapolis, Minnesota.

93. *Itasca Consulting Group, Inc.,2005.* ***FLAC (Fast Lagrangian Analysis of Continua)****, Version* 5.0. Minneapolis: ICG.
94. ITURRIOZ, I., LACIDOGNA, G. & CARPINTERI, A. 2013. Experimental analysis and truss-like discrete element model simulation of concrete specimens under uniaxial compression. *Engineering Fracture Mechanics,* 110**,** 81-98
95. J. Glucklich, "Fracture of Plain Concrete," *Engineering Mechanics Division Journal,* ASCE, Vol. 89, No. EM6, December 1963, pp. 127-138.
96. J.J. Du, A.S. Kobayashi, and N.M. Hawkins, "FEM Dynamic Fracture Analysis of Concrete Beams," *Journal of Engineering Mechanics,* Vol. 115, No. 10, October, 1989.
97. Jirásek, M. and Bazant, Z.P., 1995. Particle model for quasibrittle fracture and application to sea ice. *Journal of engineering mechanics*, *121*(9), pp.1016-1025.
98. Johnson, K. (1985). Contact Mechanics. Cambridge University Press
99. Kalyan, T. S., & Kishen, J. C (2013). Experimental Evaluation of Cracks in Concrete by Ultrasonic Pulse Velocity.
100. Katsaga, T. (2010). *Geophysical imaging and numerical modelling of fractures in concrete* (Doctoral dissertation, University of Toronto).
101. Kazerani, T., 2011. *Micromechanical study of rock fracture and fragmentation under dynamic loads using discrete element method* (Doctoral dissertation, ÉCOLE POLYTECHNIQUE FÉDÉRALE DE LAUSANNE).
102. Khan, A. S. and Huang, S. (1995). Continuum theory of plasticity. John Wiley & Sons, New York.
103. Kim, S.M. and Al-Rub, R.K.A., 2011. Meso-scale computational modeling of the plastic-damage response of cementitious composites. *Cement and Concrete Research*, *41*(3), pp.339-358.
104. Kim, Y.R., Baek, C., Underwood, B.S., Subramanian, V., Guddati, M.N. and Lee, K., 2008. Application of viscoelastic continuum damage model based finite element analysis to predict the fatigue performance of asphalt pavements. *KSCE Journal of Civil Engineering*, *12*(2), pp.109-120.
105. Kirkwood J. G., Buff F. P., Green M. S. (1949), "The statistical mechanical theory of transport processes", J. Chem. Phys., vol. 17, n° 10, p. 988, 1949.
106. Kishino Y. (ed.), Powders & Grains 2001, Balkema, Rotterdam, 2001.
107. Kishino, Y. (1988). Disc model analysis of granular media. Micromechanics of granular materials, Satake and Jenkins (eds), Elsevier Science Publishers, Amsterdam, Netherlands, 143-152.
108. Konagai, K., Rangelow, P., & Sato, T. (1994). Real-time observation of dynamic changes in the fabric of granular material structures through laser-aided tomography. In Proceedings of the 10th European Conference on Earthquake Engineering (pp. 459-466). AA Balkema/CRC Press, Boca Raton, FL.
109. Konagai, K., Tamura, C., Rangelow, P., & Matsushima, T. (1992). Laser-aided tomography: a tool for visualization of changes in the fabric of granular assemblage. Structural Engineering/Earthquake Engineering, 9(3), pp.193s-201s.
110. KOZICKI, J. & DONZÉ, F. 2008. A new open-source software developed for numerical simulations using discrete modeling methods. *Computer Methods in Applied Mechanics and Engineering*, 197**,** 4429-4443.
111. Kozicki, J. and Tejchman, J., 2008. Modelling of fracture process in concrete using a novel lattice model. *Granular Matter*, *10*(5), pp.377-388.
112. Kruyt, N.P., Rothenburg, L.: Micromechanical definition of the strain tensor for granular materials. J. Appl.Mech. 63(3), 706–711 (1996).
113. L. Cedolin, S. Dei Poli and I. Iori, "Experimental Determination of the Stress-Strain Curve and Fracture Energy for Concrete in Tension," *Proceedings of International Conference on Constitutive Laws for Engineering Materials,* University of Arizona, 1983, pp. 393-398.
114. Labuz, J.F., Shah, S.P. and Dowding, C.H., 1985, April. Experimental analysis of crack propagation in granite. In International Journal of Rock Mechanics and Mining Sciences & Geomechanics Abstracts (Vol. 22, No. 2, pp. 85-98). Pergamon

115. Latiere, H. J., & Mazerolle, F. (1987). The X-ray scanner. A tool for the examination of the intravoluminal crystalline state of aluminum. Engineering Fracture Mechanics, 27(4), pp.413-463.
116. Latzel, M., S.Luding, and H. Herrmann (2000). Macroscopic material properties from quasi-static, microscopic simulations of a two-dimensional shear cell. Granular matter 2, 123-135.
117. Le Chatelier, H., 1882. Recherches expérimentales sur la constitution des ciments et la théorie de leur prise. *Paris Acad. Sci. Compt. Rend*, *94*, pp.867-869.
118. Lee, X. (1994). An experimental study of granular packing structure changes under load. STUDIES IN APPLIED MECHANICS, 35, pp.101-101.
119. Lee, York Wei. Discrete element modelling of idealised asphalt mixture. Diss. University of Nottingham, 2006.
120. Liao C., Chang T., Young D., and Chang C. (1997), 'Stress-strain relationships for granular materials based on the hypothesis of best fit', *International Journal of Solids and Structures*, n°34, pp. 4087-4100.
121. Liao C., Chang T., Young D., and Chang C. (1997), 'Stress-strain relationships for granular materials based on the hypothesis of best fit', *International Journal of Solids and Structures*, n°34, pp. 4087-4100.
122. Lilliu, G. and van Mier, J.G., 2003. 3D lattice type fracture model for concrete. *Engineering Fracture Mechanics*, *70*(7), pp.927-941.
123. Lin, X. and T.-T. Ng (1997). A three-dimensional discrete element model using arrays of ellipsoids. Geotechnique 47 (2), 319-329.
124. Lorig, L., Gibson, W., Alvial, J. and Cuevas, J., 1995. Gravity flow simulations with the particle flow code (PFC). *ISRM News J*, *3*(1), pp.18-24.
125. Love A. E. H. (1927) 'A treatise on the mathematical theory of elasticity'.
126. Luding, S., 2008. Introduction to discrete element methods: basic of contact force models and how to perform the micro-macro transition to continuum theory. European Journal of Environmental and Civil Engineering, 12(7-8), pp.785-826.
127. Luxmoore, A. (1973). Holographic detection of cracks in concrete. Non-Destructive Testing, 6(5), pp.258-263.
128. M. Wecharatana and W.J. Chiou, "Fracture Energy and the Complete Tensile Softening Response of Concrete," *Proceedings of the 1986 SEM Spring Conference on Experimental Mechanics*, New Orleans, pp. 23-30.
129. M.F. Kaplan, "Crack Propagation and Fracture of Concrete," ***ACI** Journal*, Vol. 58, No. 5, November 1961, pp. 591-610.
130. Ma, T., Zhang, Y., Zhao, Y. and Huang, X., 2015. Simulation of four-point bending beam fatigue test of asphalt mixture using PFC3D. In *CICTP 2015* (pp. 1016-1027).
131. Malvern, L. (1969). Introduction to the mechanics of a continuous medium. Prentice-Hall, Inc., Englewood Cliffs, New Jersey.
132. Mason, J. and Bernal, J.D., 1960. Co-ordination of randomly packed spheres. Nature, 188, pp.42-43.
133. Mehrabadi, M.M., Nemat-Nasser, S. and Oda, M., 1982. On statistical description of stress and fabric in granular materials. International Journal for Numerical and Analytical Methods in Geomechanics, 6(1), pp.95-108.
134. Mehrabadi, M.M., Nemat-Nasser, S. and Oda, M., 1982. On statistical description of stress and fabric in granular materials. *International Journal for Numerical and Analytical Methods in Geomechanics*, *6*(1), pp.95-108.
135. Mindess, S. and Diamond, S., 1980. A preliminary SEM study of crack propagation in mortar. *Cement and Concrete Research*, *10*(4), pp.509-519.
136. Mindlin, R.D. and Deresiewicz, H., 1953. *Timoshenko's shear coefficient for flexural vibrations of beams* (No. TR-10). COLUMBIA UNIV NEW YORK.
137. Mohamed, A.R., Hansen, W., 1999. Micromechanical modeling of concrete response under static loading – part I: model development and validation. ACI Material 96 (2), pp.196–203.

138. Moukarzel, C., and H. J. Herrmann. "A vectorizable random lattice." *Journal of Statistical Physics* 68, no. 5-6 (1992): 911-923.
139. Nanni, A., 1988. SPLITTING-TENSION TEST FOR FIBER REINFORCED CONCRETE. *ACI Materials Journal*, *85*(4), pp.229-233. Naval Archit.; 55: 219–230.
140. Nemati, K. (1997). Fracture analysis of concrete using scanning electron microscopy. SCANNING-NEW YORK AND BADEN BADEN THEN MAHWAH-, 19, pp.426-430.
141. Nemati, K.M., 1994. *Generation and interaction of compressive stress-induced microcracks in concrete*. Department of Civil Engineering, University of California.
142. Nemat-Nasser, S.: A micromechanically-based constitutive model for frictional deformation of granular materials. J. Mech. Phys. Solids 48(6), 1541–1563 (2000).
143. Neville, A.M. (1981) Properties of Concrete (Third Edition) Longman Group Ltd. London, UK.
144. Neville, A.M. and Brooks, J.J., 1987. *Concrete technology.*
145. Neville, A.M., Dilger, W.H. and Brooks, J.J., 1983. *Creep of plain and structural concrete*. Construction press.
146. NITKA, M. & TEJCHMAN, J. 2015. Modelling of concrete behaviour in uniaxial compression and tension with DEM. *Granular Matter,* 17**,** 145-164.
147. O'Sullivan, C., 2011. Particle-based discrete element modeling: geomechanics perspective. *International Journal of Geomechanics*, *11*(6), pp.449-464.
148. O'Sullivan, C., J.D Bray, and M.F. Riemer (2002). The influence of particle shape and surface friction variability on macroscopic frictional strength of rod-shaped particulate media.
149. Oda, M., Iwashita, K.: Mechanics of Granular Materials. A. A. Balkema, Rotterdam (1999).
150. Opara NK (1993) Fracture process zone presence and behavior in mortar specimens. ACI Mater J 90:618–626.
151. Ortiz M (1988) Microcrack coalescence and macroscopic crack growth initiation in brittle solids. Int J Solid Struct 24:231–250.
152. Owen, C. K. V. (1976). Capacitance Strain Gauges for Monitoring Cracks. In Welding Institute Conf. on the Detection and Measurement of Cracks, Abington, Cambridge, 1976, pp.2-6.
153. Paul, B., 1960. Prediction of elastic constants of multiphase materials. Transactions of the Metallurgical Society of AIME 218, pp.35–41.
154. PFC^{2D} user manual, release 3.00 (1997). Itasca Consulting Group, Inc., Minneapolis.
155. Pöschel T., Luding S. (eds), Granular Gases, Springer, Berlin, 2001. Lecture Notes in Physics 564.
156. Poschel, T. and T Schwager (2005). Computational Granular Dynamics. Springer-Verlag.
157. Potyondy, D.O. and P.A Cundall (2004). A bonded-particle model for rock. International Journal of Rock Mechanics and Mining Sciences 41(8), 1329-1364.
158. Pyrak, L.J., 1988. *Seismic visibility of fractures*. California Univ., Berkeley, CA (USA).
159. R. A. Miller, S. P. Shah, and H. I. Bjelkhagen, "Crack Profiles in Mortar Measured by Holographic Interferometry," *Experimental Mechanics*, 28 (4), 388-394 (1988).
160. R. Jones. (1962). Non destructive testing of concrete. University Press.
161. Rangelow, P. & Konagai, K. 1995. The effect of vertical loading rate on the bearing capacity of footings. Proc. 1st Int. Conf. Earthquake Geotechnical Engineering 2: pp.797-802.
162. Rao, Q., Sun, Z., Stephansson, O., Li, C. and Stillborg, B., 2003. Shear fracture (Mode II) of brittle rock. International Journal of Rock Mechanics and Mining Sciences, 40(3), pp.355-375.
163. Rapaport, D.C., 2004. The art of molecular dynamics simulation. Cambridge university press.
164. Raynaud, S., Fabre, D., Mazerolle, F., Geraud, Y., & Latière, H. J. (1989). Analysis of the internal structure of rocks and characterization of mechanical deformation by a non-destructive method: X-ray tomodensitometry. Tectonophysics, 159(1), pp.149-159.
165. Reinhardt, H.W., Cornelissen, H.A. and Hordijk, D.A., 1986. Tensile tests and failure analysis of concrete. *Journal of structural engineering*, *112*(11), pp.2462-2477.

166. Reuss, A., 1929. Zeitschrift fur angewandte mathematic und mechanic. Verlag des Vereines Deutscher Igenieure 9, Berlin, Germany.
167. Richardson I (1999) The nature of C–S–H in hardened cements. Cem Concr Res 29:1131–1147.
168. Rothenburg, L. and N. Kruyt (2004). Critical state and evolution of coordination number in simulated granular materials. International journal of solids and structures 41, 5763-5774.
169. Rothenburg, L. and Selvadurai, A.P.S., 1981. A micromechanical definition of the cauchy stress tensor for particulate media.
170. Rothenburg, L., 1982. Micromechanics of idealized granular systems. National Library of Canada
171. *Rothenburg, L., Bathurst, R. J. (1989). Analytical study of induced anisotropy in idealized granular materials. Geotechnique, **39**(4), 601-614.*
172. Rothenburg, L., Bogobowicz, A., Hass, R., 1992. Micromechanical modeling of asphalt concrete in connection with pavement rutting problems. Seventh International Conference on Asphalt Pavements 1, pp.230–245.
173. Rothenburg, L., Bogobowicz, A., Hass, R., 1992. Micromechanical modeling of asphalt concrete in connection with pavement rutting problems. Seventh International Conference on Asphalt Pavements 1, pp.230–245.
174. Rousseau, J., Marin, P. and Daudeville, L., 2007. Discrete element modeling of reinforced concrete with a particular steel-concrete interface. *Discrete Element Group for Hazard Mitigation*.
175. Rousseau, J., Marin, P., Daudeville, L. and Potapov, S., 2009. Coupling discrete elements with shell finite elements to simulate impacts on reinforced concrete structures. In *DYMAT-International Conference on the Mechanical and Physical Behaviour of Materials under Dynamic Loading* (Vol. 2, pp. 1479-1483). EDP Sciences.
176. SADD M H, DAI Q L. (2005) A comparison of micro-mechanical modeling of asphalt materials using finite elements and doublet mechanics [J]. Mechanics of Materials, 2005, 37(6): 641−662.
177. Sadd, M.H., Dai, q., Parameswaran, V., Shukla, A., 2004. Microstructural simulation of asphalt materials: modeling and experimental studies. Journal of Materials in Civil Engineering 16, pp.107–115.
178. Schlangen, E. and Garboczi, E.J., 1997. Fracture simulations of concrete using lattice models: computational aspects. *Engineering fracture mechanics*, *57*(2), pp.319-332.
179. Schlangen, E., van Mier, J.G.M., 1992. Experimental and numerical analysis of the micro-mechanisms of fracture of cement-based composites. Journal of Cement and Concrete Composites 14 (2), pp.105–118.
180. Scott, G.D., 1960. Packing of spheres: packing of equal spheres. Nature, 188(4754), pp.908-909.
181. Shahbeyk, S., Hosseini, M. and Yaghoobi, M., 2011. Mesoscale finite element prediction of concrete failure. *Computational Materials Science*, *50* (7), pp.1973-1990.
182. Shiu, W., Donze, F.V. and Daudeville, L., 2009. Discrete element modelling of missile impacts on a reinforced concrete target. *International Journal of Computer Applications in Technology*, *34*(1), pp.33-41.
183. Shiu, W.J., Donzé, F. and Daudeville, L., 2005. Missile impact on a concrete slab: a 3D discrete element study.
184. Sinaie, S., 2017. Application of the discrete element method for the simulation of size effects in concrete samples. *International Journal of Solids and Structures*, *108*, pp.244-253.
185. Sitharam, T., J. Vinod, and B.Ravishankar 2008. Evaluation of undrained response from drained triaxial shear tests: DEM simulations and experiments. Geotechnique 58(7), 605-608.
186. Skarżyński, L. Tejchman, J., 2010. Calculations of fracture process zones on meso-scale in notched concrete beams subjected to three-point bending. *European Journal of Mechanics-A/Solids*, *29*(4), pp.746-760.
187. Skarżyński, Ł., and J. Tejchman. Modelling the effect of composition on the tensile properties of concrete. In: Weerheijm, J. ed., 2013. Understanding the tensile properties of concrete. Woodhead Publishing Limited; 2013. p. 52–97.

188. Skarżyński, L., Nitka, M. and Tejchman, J., 2015. Modelling of concrete fracture at aggregate level using FEM and DEM based on X-ray μCT images of internal structure. Engineering Fracture Mechanics, 147, pp.13-35.

189. ŠMILAUER, V. & CHAREYRE, B. 2010. Yade dem formulation. *Yade Documentation*.

190. Sneddon, I., 1946, October. The distribution of stress in the neighbourhood of a crack in an elastic solid. In *Proc. R. Soc. Lond. A* (Vol. 187, No. 1009, pp. 229-260). The Royal Society.

191. Sohn, H.Y. and Moreland, C., 1968. The effect of particle size distribution on packing density. The Canadian Journal of Chemical Engineering, 46(3), pp.162-167.

192. Sokolovsky, A., Gueraud, R., Dulac, J. and Labrot, R., 1977. *Local behavior of reinforced concrete walls under missile impact* (No. CEA-CONF--4062). CEA Centre d'Etudes Nucleaires de Saclay.

193. Sorelli L, Constantinides G, Ulm FJ, Toutlemonde F (2008) The nano-mechanical signature of ultra high performance concrete by statistical nanoindentation techniques. Cem Concr Res 38:1447–1456.

194. Su, J., Zhang, L. and Zhao, Y., 2017, April. Numerical simulation of fracture process of concrete under uniaxial compression via PFC2D. In *IOP Conference Series: Earth and Environmental Science* (Vol. 61, No. 1, p. 012069). IOP Publishing.

195. SUCHORZEWSKI, J., TEJCHMAN, J. & NITKA, M. 2017. Discrete element method simulations of fracture in concrete under uniaxial compression based on its real internal structure. *International Journal of Damage Mechanics***,** 1056789517690915.

196. Szilágyi, K., 2009. DEM modelling of the Brinell-testing of concrete. *Micromechanics of granular media–Manuscript*.

197. T.C. Hsu, F.O. Slate, and G.M. Sturman, "Microcracking of Plain Concrete and Shape of the Stress-Strain Curve," *Journal of the American Concrete Institute,* Vol. 60, 1963, pp. 209-224.

198. Tavarez, F.A., Plesha, M.E. and Bank, L.C., 2002. Discrete element method (DEM) for modeling solid and particulate media. In *Discrete Element Methods: Numerical Modeling of Discontinua* (pp. 155-160).

199. Tejchman, J. and Bobiński, J., 2012. *Continuous and discontinuous modelling of fracture in concrete using FEM*. Springer Science & Business Media.

200. Thornton C., Barnes D.J. (1986b) 'Computer simulated deformation of compact granular assemblies', *Acta Mechanica*, n°64, pp 45-61.

201. Thornton, C. and S. Antony (2000). Quasi-static shear deformation of a soft particle system. Powder Technology 109, 179-191.

202. Tran, V.T., Donzé, F.V. and Marin, P., 2011. A discrete element model of concrete under high triaxial loading. *Cement and Concrete Composites*, *33*(9), pp.936-948.

203. Trtik P, Munch B, Lura P (2009) A critical examination of statistical nanoindentation on model materials and hardened cement pastes based on virtual experiments. Cem Concr Compos 31:705–714.

204. Trtik P, Reeves C, Bartos PJM (2000) Use of focused ion beam (FIB) for advanced interpretation of microindentation test results applied to cementitious composites. Mater Struct 33:189–193

205. Ulm F, Constantinides G, Heukamp FH (2004) Is concrete a poromechanics material? A multiscale investigation of poroelastic properties. Mater Struct 37:43–58.

206. Vermeer P. A., Diebels S., Ehlers W., Herrmann H. J., Luding S., Ramm E. (2001) (eds), Continuous and Discontinuous Modelling of Cohesive Frictional Materials, Springer, Berlin, 2001. Lecture Notes in Physics 568

207. Voigt, W., 1889. A unified micromechanical approach. Mechanics of Composite Materials, pp.12–21

208. Wang, C., D. Tannant, and P. Lilly (2003). Numerical analysis of the stability of heavily jointed rock slopes using pfc2D. International Journal of Rock Mechanics and Mining Sciences 40, 415-424.

209. Weber J. (1966) 'Recherches concernant les contraintes intergranulaires dans les milieux pulvérulents. Application à la rhéologie de ces milieux', *Cahiers du G.F.R.*, n°3, pp.161-170.
210. Westergaard, H., (1939). Bearing Pressures and Crack. *Journal of applied mechanics*, *18*.
211. Whittaker, B.N., Singh, R.N. and Sun, G., 1992. *Rock fracture mechanics*. Elsevier.
212. Williams, J.R. and O'Connor, R., 1999. Discrete element simulation and the contact problem. *Archives of Computational Methods in Engineering*, *6*(4), pp.279-304.
213. Wu, J., 2009. *Discrete Element Modelling of Compression Tests for an Idealised Asphalt Mixture* (Doctoral dissertation, PhD Thesis, University of Nottingham).
214. Yadav, G.D., Dullien, F.A.L., Chatzis, I. and Macdonald, I.F., 1987. Microscopic distribution of wetting and nonwetting phases in sandstones during immiscible displacements. *SPE Reservoir Engineering*, *2*(02), pp.137-147
215. Yang, Z.J. and Proverbs, D., 2004. A comparative study of numerical solutions to non-linear discrete crack modelling of concrete beams involving sharp snap-back. *Engineering fracture mechanics*, *71*(1), pp.81-105
216. Yimsiri, S. and K.Soga (2010). DEM analysis of soil fabric effects on behavior of sand. Geotechnique 60(6), 483-495.
217. Yin, A., Yang, X., Gao, H. and Zhu, H., 2012. Tensile fracture simulation of random heterogeneous asphalt mixture with cohesive crack model. *Engineering Fracture Mechanics*, *92*, pp.40-55.
218. Zhang, X., Lu, M. and Wegner, J.L., 2000. A 2-D meshless model for jointed rock structures. International Journal for Numerical Methods in Engineering, 47(10), pp.1649-1661.
219. Zheng, Z., 1989. *Compressive stress-induced microcracks in rocks and applications to seismic anisotropy and borehole stability*. University of California, Berkeley.
220. Zhou, F., Molinari, J.F. and Shioya, T., 2005. A rate-dependent cohesive model for simulating dynamic crack propagation in brittle materials. Engineering Fracture Mechanics, 72(9), pp.1383-1410.
221. Zhou, S., Zhu, H., Yan, Z., Ju, J. W., & Zhang, L. (2016). A micromechanical study of the breakage mechanism of microcapsules in concrete using PFC2D. *Construction and Building Materials*, *115*, pp.452-463
222. Zhu W, Bartos PJM (2000) Application of depth-sensing microindentation testing to study of interfacial transition zone in reinforced concrete. Cem Concr Res 30:1299–1304.
223. Zhu W, Sonebi M, Bartos PJM (2004) Bond and interfacial properties of reinforcement in self-compacting concrete. Mater Struct 37:442–448.
224. Zhu, H., Z.Zhou, R. Yang, and A. Yu (2007). Discrete particle simulation of particulate systems: Theoretical developments. Chemical Engineering Science 62 (13), 3378-3396.

Appendix A

A.1 Uniaxial compressive test (UCT)

UCT code part A: Make sample generation

```
; fname: make_assembly.p3dat
;
; Create a balls assembly from a Particle Size Distribution of a concrete
(coarse aggregate)
; sample
;=======================================================
new
title 'Uniaxial Compressives test'
; Set the domain extent
fish create domain_extent = 0.2


domain extent [-domain_extent] [domain_extent] condition destroy

cmat default model linear method deformability emod 1.0e9 kratio 0.0
cmat default property dp_nratio 0.5

;========create cylindrical walls and top and bottom wall ==========

wall generate id 1 ...
   group cylinders ...
   cylinder ...
      axis 0 0 1 ...
      base 0 0.0 -0.15 ...
      cap true true ...
      height 0.3 ...
      onewall ...
      radius 0.075 ...

; Input cylinder radius and height
define setup
bottom_disk_position_vec = vector(0.0,0.0,-0.15)
top_disk_position_vec    = vector(0.0,0.0, 0.15)
end
@setup

wall generate id 5 plane position @top_disk_position_vec ...
                  dip 0 ...
                  ddir 0

wall generate id 6 plane position @bottom_disk_position_vec ...
                  dip 0 ...
                  ddir 0
;==============   Granulometry  ========================

;Input raw data of concrete granulometry
def granulometry
  global exptab = table.create('experimental')
  table(exptab,0.00236) = 0.01
  table(exptab,0.005) = 0.152
  table(exptab,0.01) = 0.902
  table(exptab,0.014) = 0.989
  table(exptab,0.02) = 0.991
  table(exptab, 0.028) = 1.0
end
@granulometry


; Generate the sample
; Input the min diameter of aggregate and the target porosity value
; Change the number of bin input depending on the sieve test

fish create dmin = 0.00236

set random 10001
  ball distribute              ...
       porosity 0.3                                    ...
        numbin 6                                       ...
       bin 1                                           ...
          radius [0.5*dmin] [0.5*table.x(exptab,1)]          ...
          volumefraction [table.y(exptab,1)]                 ...
          group concrete                               ...
       bin 2                                           ...
          radius [0.5*table.x(exptab,1)] [0.5*table.x(exptab,2)]    ...
          volumefraction [table.y(exptab,2)-table.y(exptab,1)]      ...
          group concrete                               ...
       bin 3                                           ...
          radius [0.5*table.x(exptab,2)] [0.5*table.x(exptab,3)]    ...
          volumefraction [table.y(exptab,3)-table.y(exptab,2)]      ...
          group concrete                               ...
       bin 4                                           ...
          radius [0.5*table.x(exptab,3)] [0.5*table.x(exptab,4)]    ...
          volumefraction [table.y(exptab,4)-table.y(exptab,3)]      ...
          group concrete                               ...
       bin 5                                           ...
          radius [0.5*table.x(exptab,4)] [0.5*table.x(exptab,5)]    ...
          volumefraction [table.y(exptab,5)-table.y(exptab,4)]      ...
          group concrete                               ...
       bin 6                                           ...
          radius [0.5*table.x(exptab,5)] [0.5*table.x(exptab,6)]    ...
          volumefraction [table.y(exptab,6)-table.y(exptab,5)]      ...
          group concrete                               ...
        range cylinder end1 0 0 -0.15 end2 0 0 0.15 radius 0.075 extent


measure create id 1 radius 0.0675 ...
                bins 500 @dmin [table.x(exptab,6)]
measure dump id 1 table 'numerical'

ball attribute density 2500 damp 0.7

pause key
;=======================================================


; Calm the system

history id 1 mechanical solve time
;ball history id 2 unbalforce id 489119
;ball history id 3 contactforce id 489119
cycle 1000 calm 10
; Solve the system to a target limit (here the average force ratio)
; Use density scaling to quickly reach equilibrium

def timestep
   timestep=math.sqrt(m/K)
   time=mech.age
end


set timestep scale
solve aratio 1e-4 max_cycles 2000
set timestep auto
calm

;Delete side walls
; Be careful to include the keyword 'walls' or else facets will be deleted

wall delete range id 1 by wall


save make_assembly
return
;=================================================
; eof: Granulometry.p3dat
```

UCT code part 2 : Add Bonds

```
;fname: parallel_bonded.p3dat
;
;  Create parallel bonded sample
;=======================================================
=======================

restore make_assembly

contact model linearpbond range contact type ball-ball
contact method bond gap 2.0e-4

; set linear stiffness using methods
contact method deformability emod 3.0e10 krat 2.4

; set stiffness of bonds using methods
contact method pb_deformability emod 3.0e10 krat 2.4

; set bond strengths
contact property pb_ten 5.4e6 pb_coh 10.5e6 pb_fa 20.0

; set some damping at the contacts
contact property dp_nratio 0.5

; set ball-ball friction to non-zero value
contact property fric 0.3 range contact type ball-ball


;=======================================================

; Reset ball displacement
ball attribute displacement multiply 0.0

; Set the linear force to 0.0 and force a reset of the linear contact forces.
contact property lin_force 0.0 0.0 0.0 lin_mode 1
ball attribute contactforce multiply 0.0 contactmoment multiply 0.0
cycle 1
solve aratio 1e-5

save parallel_bonded

;=======================================================
; eof: parallel_bonded.p3dat
```

UCT code part 3 : Make Platen

```
;fname: make_platen.p3dat
;
; determine average stress and strain at walls
;=======================================================
def wall_addr
 global wp_top = wall.find(5) ; assume wall 5 is the top wall
  global wp_bottom = wall.find(6) ; assume wall 6 is the bottom wall

end
@wall_addr

;=======================================================

define setup_wall
;
; Find the walls and get initial sample dimensions

  global sample_height = wall.pos.z(wp_top) - wall.pos.z(wp_bottom)

   ;assume x and y are approximately the same in 3D
  local xmin = 1.0e12
  local xmax = -1.0e12
  loop foreach bp ball.list
    local ball_xmin = ball.pos.x(bp) - ball.radius(bp)
    xmin = math.min(xmin,ball_xmin)
    local ball_xmax = ball.pos.x(bp) + ball.radius(bp)
    xmax = math.max(xmax,ball_xmax)
  end_loop
  local diameter_ = xmax - xmin
  if global.dim = 2
    global cross_sectional_area = diameter_
  else
    ; assume cylindrical sample in 3D
    cross_sectional_area = math.pi*0.25*diameter_*diameter_
  end_if

  end

  ;====================axial stress=========================
  define axial_stress_wall
;
; Compute axial stress (positive tension) using walls
;
; Assumes global variables sample_height and sample_width have been set
;

  local force1 = -wall.force.contact.z(wp_top)
  local force2 = wall.force.contact.z(wp_bottom)
  axial_stress_wall = 0.5*(force1+force2)/cross_sectional_area
end

; =============Engineering strain==========================

define axial_Eng_strain_wall
;
; Compute axial strain (positive tension) using walls
;
; Assumes global variable sample_width has been set
;
  axial_Eng_strain_wall = 2.0*wall.disp.z(wp_top)/sample_height
end

;======================Pure Strain=======================

define axial_Pure_strain_wall
;
; Compute axial strain (positive tension) using walls
;
; Assumes global variable sample_width has been set

x=wall.disp.z(wp_top)
y=wall.disp.z(wp_bottom)
zdif = x-y

new_height= cylinder_height + zdif

  axial_pure_strain_wall = 2*zdif/(new_height+sample_height)
end

;=====================================================

define young_modulus

young_modulus= axial_Eng_strain_wall/axial_pure_strain_wall

end

;=====================================================
define loadhalt_wall
;
; Function used to stop a test when axial stress decreases to some fraction of
the peak
; Assumes axial_stress_wall is a function that returns axial stress
;
; INPUT: peak_fraction - fraction of peak stress that dictates the stopping of
the test
;                      (global float)
;
  loadhalt_wall = 0
  local abs_stress = math.abs(axial_stress_wall)
  global peak_stress = math.max(abs_stress,peak_stress)
  if abs_stress < peak_stress*peak_fraction
    loadhalt_wall = 1
  end_if
end
;=====================================================
```

UCT code part 4 : Fracture

```
; fname: fracture.p3fis
;
; Simple environment to track fragmentation in a BPM.
; Monitor LinearPBond model "bond_break" events and turn them into
fractures.
; Use the Fragment and Ball Result logic to record fragment IDs
;
;=====================================================

define add_crack(entries)
  local contact    = entries(1)
  local mode       = entries(2)
  local strength   = entries(3)
  local frac_pos   = contact.pos(contact)
  local norm       = contact.normal(contact)
  local dfn_label  = 'crack'
  local frac_dip
  local frac_dipdir
  local frac_size = contact.prop(contact,'pb_radius')

  local len2 =
math.sqrt(comp.x(norm)*comp.x(norm)+comp.y(norm)*comp.y(norm))
  if len2 = 0
    len2 = 1
  endif
  frac_dipdir = math.atan2(comp.x(norm)/len2,comp.y(norm)/len2) /
math.degrad
  local len3 = math.sqrt(len2*len2+comp.z(norm)*comp.z(norm))
  if len3 = 0
    len3 = 1
  endif
  frac_dip = math.atan2(len2/len3,comp.z(norm)/len3) / math.degrad
  if frac_dip<0.0
    frac_dip = -frac_dip
    frac_dipdir = frac_dipdir + 180.0
  endif
  if frac_dip>90.0
    frac_dip = 180.0-frac_dip
    frac_dipdir = frac_dipdir + 180.0
  endif
  if frac_dipdir<0.0
    frac_dipdir = frac_dipdir + 360.0
  endif
  if frac_dipdir > 360.0
    frac_dipdir = frac_dipdir - 360.0
  endif
  if mode = 1 then
    ; failed in tension
    dfn_label = dfn_label + '_tension'
  else if mode = 2 then
    ; failed in shear
    dfn_label = dfn_label + '_shear'
  endif
  local arg = array.create(5)
  arg(1) = 'disk'
  arg(2) = frac_pos
  arg(3) = frac_size
  arg(4) = frac_dip
  arg(5) = frac_dipdir

  global dfn = dfn.find(dfn_label)
  if dfn = null then
    dfn = dfn.add(0,dfn_label)
  endif
  local fnew = dfn.addfracture(dfn,arg)
  dfn.fracture.prop(fnew,'failure_strength') = strength
  dfn.fracture.prop(fnew,'age')  = track_time
  crack_added = true
end

define monitor
  if crack_added = true then
    local numfrag = fragment.num()
    command
      fragment compute
    endcommand
    if fragment.num() # numfrag then
      command
        ball result generate fishtime @track_time
        wall result generate fishtime @track_time
      endcommand
      map.add(track_map,track_time,numfrag)
    endif
  endif
  crack_added = false
end

define track_time
  track_time = mech.age
end

define track_init
  command
    dfn delete
    ball result clear
    wall result clear
    fragment clear
    fragment register ball-ball
    ball result addattribute fragment
    wall result addattribute velocity
  endcommand
  ; activate fishcalls
  command
    set fishcall bond_break remove @add_crack
    set fishcall bond_break @add_crack
    set fishcall 100.0 remove @monitor
    set fishcall 100.0 @monitor
  endcommand
  ; reset global variables
  global crack_added = false
  global track_time0 = mech.age()
  command
    fragment compute
    ball result generate fishtime @track_time
    wall result generate fishtime @track_time
  endcommand
  global track_map = map(track_time,fragment.num(1))
end

define track_end
  local numfrag = fragment.num()
  command
    fragment compute
  endcommand
  if fragment.num() # numfrag then
    command
      ball result generate fishtime @track_time
      wall result generate fishtime @track_time
    endcommand
    map.add(track_map,track_time,numfrag)
  endif
  make_table
end

define make_table
  local frag1 = fragment.find(1)
  local tab = table.create('volfrag1')
  loop foreach local value map.keys(track_map)
    table(tab,value) = fragment.vol(frag1,fragment.catalog.num(value)) /
fragment.vol(frag1,1)
  endloop
end

;=====================================================
; eof: fracture.p3fis
```

UCT code part 5 : Test run

```
; fname: test_perform.p3dat
;
;  Perform an uniaxial-unconfined compressive strength test on a bonded
sample
;=====================================================
restore parallel_bonded
```

```
set logfile parallel3d.log
set log on

set echo off
call make_platen.fis
call fracture.p3fis
set echo on

;=====================================================
; set up global parameters for stress and strain measurement
@setup_wall

; apply loading by moving top and bottom walls
wall attribute zvelocity -0.001 range id 5
wall attribute zvelocity  0.001 range id 6

; apply a small amount of damping
ball attribute damp 0.1

;=====================================================
; add a measurement circle to record stress
; location defaults to 0,0

;measure create id 2 radius 0.065
;history id 6 measure stresszz id 2

;=====================================================

; record histories
history id 4 @axial_stress_wall
history id 5 @axial_Eng_strain_wall

;=====================================================

; record cracks

@track_init

; cycle a few steps to get past initial vibrations
;cyc 1000

; run the test until stress falls below 70% of the peak
set @peak_fraction = 0.7
solve fishhalt @loadhalt_wall
list @peak_stress

@young_modulus

;=====================================================
save parallel_uniaxial
set log off
; eof: ucs.p3dat
```

A.2 Unreinforced flexural test (UFT)

UFT code part 1: Make sample generation

```
; fname: make_assembly.p3dat
;
;  Create a balls assembly from a Particle Size Distribution of a concrete
(coarse aggregate)
;  sample
;=====================================================
new
title '3-point flexural test'

; Set the domain extent

set random 10001

domain extent (-0.3 0.3) (-0.2 0.2) (-0.3 0.3) condition destroy
pause key

cmat default model linear method deformability emod 1.0e9 kratio 0.0
cmat default property dp_nratio 0.5
;=================create walls ============================
new


pause key

wall generate id 1 ...
   group cylinders ...
   cylinder ...
      axis 0 1 0 ...
      base -0.2 -0.095 -0.095 ...
      cap true true ...
      height 0.19 ...
      onewall ...
      radius 0.02

wall generate id 2 ...
   group cylinders ...
   cylinder ...
      axis 0 1 0 ...
      base 0 -0.095 0.095 ...
      cap true true ...
      height 0.19 ...
      onewall ...
      radius 0.02

wall generate id 3 ...
   group cylinders ...
   cylinder ...
      axis 0 1 0 ...
      base 0.2 -0.095 -0.095 ...
      cap true true ...
      height 0.19 ...
      onewall ...
      radius 0.02

wall generate id 4 ...
     box (-0.275 0.275) (-0.075 0.075) (-0.075 0.075) ...
     onewall

pause key

;===============  Granulometry  ======================
;Input raw data of concrete granulometry

def granulometry
  global exptab = table.create('experimental')
  table(exptab,0.008) = 0.145
  table(exptab,0.01) = 0.911
  table(exptab,0.014) = 1

end
@granulometry

; Generate the sample
; Input the min diamter of aggregate and the target porosity value
; Change the number of bin input depending on the sieve test
fish create dmin = 0.008

ball distribute box (-0.275 0.275) (-0.075 0.075) (-0.075 0.075) group
concrete                ...
      porosity 0.3                                  ...
      numbin 3                                      ...
      bin 1                                        ...
         radius [0.5*dmin] [0.5*table.x(exptab,1)]          ...
         volumefraction [table.y(exptab,1)]                 ...
         group concrete                                ...
      bin 2                                        ...
         radius [0.5*table.x(exptab,1)] [0.5*table.x(exptab,2)]   ...
         volumefraction [table.y(exptab,2)-table.y(exptab,1)]     ...
         group concrete                                ...
      bin 3                                        ...
         radius [0.5*table.x(exptab,2)] [0.5*table.x(exptab,3)]   ...
         volumefraction [table.y(exptab,3)-table.y(exptab,2)]     ...
         group concrete                                ...
```

```
measure create id 1 radius 0.0675 ...
                bins 500 @dmin [table.x(exptab,3)]
measure dump id 1 table 'numerical'
ball attribute density 2500 damp 0.7
;=================================================
; Calm the system

history id 1 mechanical solve time
;ball history id 2 unbalforce id 56022
;ball history id 3 contactforce id 56022
cycle 1000 calm 10
; Solve the system to a target limit (here the average force ratio)
; Use density scaling to quickly reach equilibrium

def timestep
   timestep=math.sqrt(m/K)
   time=mech.age
end

set timestep scale
solve aratio 1e-4 max_cycles 5000
set timestep auto
calm

wall delete range id 4 by wall
save make_sample
return
;=================================================
; eof: Granulometry.p3dat
```

UFT code part 2: Add Parallel bond

```
;fname: parallel_bonded.p3dat
;
;  Create parallel bonded sample
;=================================================
restore make_sample
contact model linearpbond range contact type ball-ball
contact method bond gap 2.0e-4

; set linear stiffness using methods
contact method deformability emod 3.0e10 krat 5

; set stiffness of bonds using methods
contact method pb_deformability emod 3.0e10 krat 5

; set bond strengths
contact property pb_ten 5e6 pb_coh 15e11 pb_fa 20

; set some damping at the contacts
contact property dp_nratio 0.1

; set ball-ball friction to non-zero value
contact property fric 0.753 range contact type ball-ball
;=================================================

; Reset ball displacement
ball attribute displacement multiply 0.0

; Set the linear force to 0.0 and force a reset of the linear contact forces.
contact property lin_force 0.0 0.0 0.0 lin_mode 1
ball attribute contactforce multiply 0.0 contactmoment multiply 0.0
;clean
cycle 1
solve aratio  5e-3  max_cycles 1000

;=================================================
save parallel_bonded
;=================================================
; eof: parallel_bonded.p3dat
```

UFT code part 3: Wall Function

```
def wall_addr
global wp_left = wall.find(1) ; assume wall 1 is the left support
global wp_right = wall.find(3) ; assume wall 3 is the right support
global wp_top = wall.find(2) ; assume wall 2 is the top support

wall.vel.x(wp_left)= 0
wall.vel.y(wp_left)= 0
wall.vel.z(wp_left)= 0

wall.rotation.center.x(wp_left)=0
wall.rotation.center.y(wp_left)=0
wall.rotation.center.z(wp_left)=0

wall.vel.x(wp_right)= 0
wall.vel.y(wp_right)= 0
wall.vel.z(wp_right)= 0

wall.rotation.center.x(wp_right)=0
wall.rotation.center.z(wp_right)=0

wall.vel.x(wp_top)= 0
wall.vel.y(wp_top)= 0

wall.rotation.center.y(wp_top)=0
wall.rotation.center.z(wp_top)=0

end
;=================================================
define axial_disp_wall

axial_disp_wall= wall.disp.z(wp_top)
end
;=================================================
define axial_force_wall

axial_force_wall = -wall.force.contact.z(wp_top)
end
;=================================================

define ini_mstrain (sid)
  command
    ball attribute displacement multiply 0.0
  endcommand
  global mstrains = matrix (3,3)
  global mp = measure.find(sid)
end

define accumalate_mstrain
  global msrate = measure.strainrate.full(mp)
  global mstrains = mstrains + msrate *global.timestep

  global xxmstrain = mstrains (1,1)
  global xymstrain = mstrains (1,2)
  global xzmstrain = mstrains (1,3)
  global yxmstrain = mstrains (2,1)
  global yymstrain = mstrains (2,2)
  global yzmstrain = mstrains (2,3)
  global zxmstrain = mstrains (3,1)
  global zymstrain = mstrains (3,2)
  global zzmstrain = mstrains (3,3)
end
;=================================================
define loadhalt_wall
;
; Function used to stop a test when axial stress decreases to some fraction of
the peak
; Assumes axial_stress_wall is a function that returns axial stress
;
; INPUT: peak_fraction - fraction of peak stress that dictates the stopping of
the test
;                   (global float)
;
  loadhalt_wall = 0
  local abs_force= math.abs(axial_force_wall)
  global peak_force = math.max(abs_force,peak_force)
  if abs_force < peak_force*peak_fraction
    loadhalt_wall = 1
  end_if
end
;=================================================
```

```
define loadhalt_meas
;
; Function used to stop a test when axial stress decreases to some fraction of
the peak
; Assumes measurement circle 1 is installed
;
; INPUT: peak_fraction - fraction of peak stress that dictates the stopping of
the test
;                      (global float)
;
  loadhalt_meas = 0
  local mp = measure.find(1)
  local abs_stress = math.abs(meas.stress(mp,global.dim,global.dim))
  global peak_stress = math.max(abs_stress,peak_stress)
  if abs_stress < peak_stress*peak_fraction
    loadhalt_meas = 1
  end_if
end
```

UFT code part 4: Fracture

```
; fname: fracture_1.p3fis
;
; Simple environment to track fragmentation in a BPM.
; Track LinearPBond model "bond_change" events and turn them into
fractures.
; Use Fragment logic and Ball Result logic to record fragemnt ids
;
;=====================================================

define add_crack(entries)
    local contact    = entries(1)
    local mode       = entries(3)
    local  frac_pos   = contact.pos(contact)
    local norm       = contact.normal(contact)
    local dfn_label  = 'crack'
    local  frac_size
    local  bp1 = contact.end1(contact)
    local  bp2 = contact.end2(contact)
    local  ret =
math.min(ball.radius(bp1),ball.radius(bp2));contact.method(contact,'pb_radi
us')
    frac_size = ret
    local arg = array.create(5)
    arg(1) = 'disk'
    arg(2) = frac_pos
    arg(3) = frac_size
    arg(4) = math.dip.from.normal(norm)/math.degrad
    arg(5) = math.ddir.from.normal(norm)/math.degrad
    if arg(5) < 0.0
      arg(5) = 360.0+arg(5)
    end_if
    crack_num = crack_num + 1

    if mode = 1 then
       ; failed in tension
       dfn_label = dfn_label + '_tension'
    else if mode = 2 then
       ; failed in shear
       dfn_label = dfn_label + '_shear'
    endif

    global dfn = dfn.find(dfn_label)
    if dfn = null then
       dfn = dfn.add(0,dfn_label)
    endif
    local fnew = dfn.addfracture(dfn,arg)
    dfn.fracture.prop(fnew,'age')  = mech.age
    dfn.fracture.extra(fnew,1) = bp1
    dfn.fracture.extra(fnew,2) = bp2
    crack_accum += 1
    if crack_accum > 50
       if frag_time < mech.age
          frag_time = mech.age
          crack_accum = 0
          command
             fragment compute
          endcommand
          ; go through and update the fracture positions
          loop for (local i = 0, i < 2, i = i + 1)
             local name = 'crack_tension'
             if i = 1
                name = 'crack_shear'
             endif
             dfn = dfn.find(name)
             if dfn # null
                loop foreach local frac dfn.fracturelist(dfn)
                   local ball1 = dfn.fracture.extra(frac,1)
                   local ball2 = dfn.fracture.extra(frac,2)
                   if ball1 # null
                      if ball2 # null
                         local len = dfn.fracture.diameter(frac)/2.0
                         local pos = (ball.pos(ball1)+ball.pos(ball2))/2.0
                         if comp.x(pos)-len > xmin
                            if comp.x(pos)+len < xmax
                               if comp.y(pos)-len > ymin
                                  if comp.y(pos)+len < ymax
                                     if comp.z(pos)-len > zmin
                                        if comp.z(pos)+len < zmax
                                           dfn.fracture.pos(frac) = pos
                                        end_if
                                     end_if
                                  endif
                               endif
                            endif
                         endif
                      endif
                   endif
                endloop
             endif
          endloop
       endif
    endif
end

define track_init
    command
       dfn delete
       ball result clear
       fragment clear
       fragment register ball-ball
    endcommand
  ; activate fishcalls
    command
       set fish callback bond_break remove @add_crack
       set fish callback bond_break @add_crack
    endcommand
    ; reset global variables
    global crack_accum = 0
    global crack_num = 0
    global track_time0 = mech.age
    global frag_time = mech.age
    global xmin = domain.min.x()
    global ymin = domain.min.y()
    global xmax = domain.max.x()
    global ymax = domain.max.y()
    global zmin = domain.min.z()
    global zmin = domain.min.z()

end
;=====================================================
; eof: fracture.p3fis
```

UFT code part 5: Test Run

```
restore parallel_bonded
;wall attribute zvelocity 10 range id 1

;wall attribute zvelocity 10 range id 3

;cycle 10

wall attribute zvelocity -0.001 range id 2

set gravity 0 0 -9.81
;=====================================================
```

```
set echo off
call wall_function.fis
call fracture.p3fis
;call fracture_1.p3fis
set echo on
;=====================================================
measure create id 3 radius 0.06
history id 7 measure stresszz id 3
history id 9 measure stressxx id 3
history id 10 measure stressyy id 3
set energy on
history id 1000 mechanical energy estrain
history id 1001 mechanical energy eslip
history id 1002 mechanical energy edashpot
history id 1003 mechanical energy epbstrain
history id 1004 mechanical energy ekinetic
history id 1005 mechanical energy ebody
history id 1006 mechanical energy edamp
history id 1007 mechanical energy eboundary

@ini_mstrain (3)

history id 8 @zzmstrain

set fish callback 11.0 @accumalate_mstrain
;=====================================================
@wall_addr
history id 5 @axial_disp_wall
history id 6 @axial_force_wall
;history id 2000 @numfrag

;=====================================================
@track_init
;history id 2000 @crack_num
;history id 2001 @crack_accum
;cycle 1000
set @peak_fraction = 0.05
;solve time 10
;set timestep scale
solve fishhalt @loadhalt_wall
@track_end
;set timestep auto
;list @peak_stress
```

A.3 Steel reinforced flexural test (SRFT)

SRFT code part 1: Make assembly

```
; fname: make_assembly.p3dat
;
;  Create a balls assembly from a Particle Size Distribution of a concrete
(coarse aggregate)
;  sample
;=====================================================
new
title '4-point steel reinforced flexural test'

; Set the domain extent

set random 10001

domain extent (-0.9 0.9) (-0.2 0.2) (-0.3 0.3) condition destroy

;=======================create walls ================

pause key

wall generate id 1 ...
   group cylinders ...
   cylinder ...
      axis 0 1 0 ...
      base -0.725 -0.05 -0.08  ...
      cap true true ...
      height 0.10 ...
      onewall ...
      radius 0.02

wall generate id 2 ...
   group cylinders ...
   cylinder ...
      axis 0 1 0 ...
      base -0.3 -0.05  0.08  ...
      cap true true ...
      height 0.10 ...
      onewall ...
      radius 0.02

wall generate id 3 ...
   group cylinders ...
   cylinder ...
      axis 0 1 0 ...
      base 0.3 -0.05 0.08  ...
      cap true true ...
      height 0.10 ...
      onewall ...
      radius 0.02

wall generate id 4 ...
   group cylinders ...
   cylinder ...
      axis 0 1 0 ...
      base 0.725 -0.05 -0.08  ...
      cap true true ...
      height 0.10 ...
      onewall ...
      radius 0.02

wall generate id 5 ...
     box (-0.8 0.8) (-0.03 0.03) (-0.06 0.06)  ...
     onewall

pause key

;=====================================================


def granulometry
  global exptab = table.create('experimental')
  table(exptab,0.008) = 0.145
  table(exptab,0.01) = 0.911
  table(exptab,0.014) = 1

end
@granulometry


; Generate the sample
; Input the min diamter of aggregate and the target porosity value
; Change the number of bin input depending on the sieve test

fish create dmin = 0.008

ball distribute box (-0.8 0.8) (-0.03 0.03) (-0.06 0.06) group concrete
...
      porosity 0.2                                    ...
      numbin 3                                        ...
      bin 1                                           ...
         radius [0.5*dmin] [0.5*table.x(exptab,1)]              ...
         volumefraction [table.y(exptab,1)]                     ...
         group concrete                                 ...
      bin 2                                           ...
         radius [0.5*table.x(exptab,1)] [0.5*table.x(exptab,2)]  ...
         volumefraction [table.y(exptab,2)-table.y(exptab,1)]    ...
         group concrete                                 ...
      bin 3                                           ...
         radius [0.5*table.x(exptab,2)] [0.5*table.x(exptab,3)]  ...
         volumefraction [table.y(exptab,3)-table.y(exptab,2)]    ...
         group concrete                                 ...

measure create id 1 radius 0.0675 ...
              bins 500 @dmin [table.x(exptab,3)]
```

```
measure dump id 1 table 'numerical'
ball attribute density 2500 damp 0.7 range group concrete

pause key
;=====================================================
contact groupbehavior and
cmat add 1  model linear                              ...
          method deformability emod 1.0e9 kratio 0.0 ...
          property dp_nratio 0.5                    ...
        range group concrete

cmat default type ball-facet                ...
          model linear                  ...
          method deformability emod 1.0e9 kratio 0.0 ...
            property dp_nratio 0.5

;=====================================================
; Calm the system

cycle 1000 calm 10
; Solve the system to a target limit (here the average force ratio)
; Use density scaling to quickly reach equilibrium

def timestep
   timestep=math.sqrt(m/K)
   time=mech.age
end

set timestep scale
solve aratio 1e-5 max_cycles 2000
set timestep auto
calm
save make_sample
return
;=====================================================
; eof: Granulometry.p3dat
```

SRFT code part 2: Add Reinforcement

```
;================ =STEEL REINFORCEMENT AND
STIRRUP============
restore make_sample
define make_steelbar1
  global _x = -0.8
  global _ballcnt = 1
  loop _ballcnt (70084,70351)
       command
        ball create id  @_ballcnt rad 0.004 x @_x y 0.02 z -0.05 group steel
       end_command
     _x = _x + 0.006
   endloop

end

@make_steelbar1
;pause key

define make_steelbar2
  global _x1 = -0.8
  global _ballcnt1 = 1
  loop _ballcnt1 (70352,70619)
    command
     ball create id  @_ballcnt1 rad 0.004 x @_x1 y -0.02 z -0.05 group steel
    end_command
    _x1 = _x1 + 0.006
  end_loop
end

@make_steelbar2

;pause key

define make_steelbar3
  global _x1 = -0.8
  global _ballcnt1 = 1
  loop _ballcnt1 (70620,71020)
    command
     ball create id @_ballcnt1 rad 0.003 x @_x1 y  0.02 z 0.05 group steel
    end_command
    _x1 = _x1 + 0.004
  end_loop
end

@make_steelbar3

;pause key

define make_steelbar4
  global _x1 = -0.8
  global _ballcnt1 = 1
  loop _ballcnt1 (71021, 71421)
    command
     ball create id @_ballcnt1 rad 0.003 x @_x1 y -0.02 z 0.05 group steel
    end_command
    _x1 = _x1 + 0.004
  end_loop
end

@make_steelbar4

;pause key

def make_Stirupp
   ball_pos_x = -0.797
   ball_pos_y = -0.0204
   ball_pos_z = -0.0505
   ball_pos_x0 = ball_pos_x
   ball_pos_y0 = ball_pos_y
   ball_radius = 0.003

   loop local i(1,21)
      loop local j(1,9)
         loop local k(1,21)
            ball_pos_vec = vector(ball_pos_x,ball_pos_y,ball_pos_z)
            ;ball.create(ball_radius,ball_pos_vec)
            command
              ball create position [ball_pos_x] [ball_pos_y] [ball_pos_z] radius
[ball_radius] group steel
            ;    ;ball create position [ball_pos_vec] radius [ball_radius]
            endcommand
            ;bp =
ball.create(ball_radius,vector(ball_pos_x,ball_pos_y,ball_pos_z), group steel
slot 1)
            ball_pos_x = ball_pos_x + 0.0795
         endloop
         ball_pos_x = ball_pos_x0
         ball_pos_y = ball_pos_y + 0.005
      endloop
      ball_pos_y = ball_pos_y0
      ball_pos_z = ball_pos_z + 0.005
   endloop
end
@make_stirupp

ball delete range x (-0.8 0.8) y (-0.019 0.018) z (-0.047 0.045) group steel


ball attribute density 8050.0  damp 0.3 range group steel

contact groupbehavior and
cmat add 2  model linearpbond                         ...
          method deformability emod 2.1e11 krat 3.3  ...
               pb_deformability emod 2.1e11 krat 3.3 ...
                    property fric 0 dp_nratio 0.5       ...
                          pb_ten 500e6 pb_coh 33.4e6 pb_fa 0.0 ...
        range group steel

cmat default type ball-ball    ...
          model linearpbond ...
          method deformability    emod 2.1e11 krat 3.3 ...
               pb_deformability emod 2.1e11 krat 3.3 ...
          property fric 0.364 dp_nratio 0.5           ...
                    pb_ten 500e6 pb_coh 33.4e6 pb_fa 20

cycle 4 calm 1
```

```
save add_reinforc
```

SRFT code part 3: Add Parallel bond

```
;fname: parallel_bonded.p3dat
;
;  Create parallel bonded sample
;=====================================================

restore add_reinforc

;=====================================================
; modify the 1st optional slot of the CMAT (contacts between concrete balls)
cmat modify 1 model linearpbond                         ...
              method deformability    emod 3.0e10 krat 2.4  ...
                    pb_deformability emod 3.0e10 krat 2.4  ...
              property fric 0.364 dp_nratio 0.1             ...
                     pb_ten 4.5e6 pb_coh 33.4e6 pb_fa 20.0

; apply the CMAT to select contacts only. Note however that since the
; CMAT has been modified, further contacts created between glass balls will
; have the linear parallel-bond contact model installed.
cmat apply range group concrete
contact method bond

;=====================================================

; Reset ball displacement
ball attribute displacement multiply 0.0

; Set the linear force to 0.0 and force a reset of the linear contact forces.
contact property lin_force 0.0 0.0 0.0 lin_mode 1
ball attribute contactforce multiply 0.0 contactmoment multiply 0.0

history id 1 mechanical solve time
;ball history id 2 unbalforce id 36195
;ball history id 3 contactforce id 36195

cycle 1

solve aratio 1e-5 max_cycles 1000

wall delete range id 5 by wall

;=====================================================

save parallel_bonded

;=====================================================
; eof: parallel_bonded.p3dat
```

SRFT code part 4: Wall Function

```
ef wall_addr
global wp_left = wall.find(1) ; assume wall 1 is the left support
global wp_right = wall.find(3) ; assume wall 3 is the right support
global wp_top = wall.find(2) ; assume wall 2 is the top support

wall.vel.x(wp_left)= 0
wall.vel.y(wp_left)= 0
wall.vel.z(wp_left)= 0

wall.rotation.center.x(wp_left)=0
wall.rotation.center.y(wp_left)=0
wall.rotation.center.z(wp_left)=0

wall.vel.x(wp_right)= 0
wall.vel.y(wp_right)= 0
wall.vel.z(wp_right)= 0


wall.rotation.center.x(wp_right)=0
wall.rotation.center.z(wp_right)=0

wall.vel.x(wp_top)= 0
wall.vel.y(wp_top)= 0

wall.rotation.center.y(wp_top)=0
wall.rotation.center.z(wp_top)=0
end

;=====================================================
define axial_disp_wall

axial_disp_wall= wall.disp.z(wp_top)
end
;=====================================================
define axial_force_wall
axial_force_wall = -wall.force.contact.z(wp_top)
end
;=====================================================

define ini_mstrain (sid)
  command
    ball attribute displacement multiply 0.0
  endcommand
  global mstrains = matrix (3,3)
  global mp = measure.find(sid)
end

define accumalate_mstrain
  global msrate = measure.strainrate.full(mp)
  global mstrains = mstrains + msrate *global.timestep

  global xxmstrain = mstrains (1,1)
  global xymstrain = mstrains (1,2)
  global xzmstrain = mstrains (1,3)
  global yxmstrain = mstrains (2,1)
  global yymstrain = mstrains (2,2)
  global yzmstrain = mstrains (2,3)
  global zxmstrain = mstrains (3,1)
  global zymstrain = mstrains (3,2)
  global zzmstrain = mstrains (3,3)
end

;=====================================================
define loadhalt_wall
;
; Function used to stop a test when axial stress decreases to some fraction of
the peak
; Assumes axial_stress_wall is a function that returns axial stress
;
; INPUT: peak_fraction - fraction of peak stress that dictates the stopping of
the test
;                    (global float)
;
  loadhalt_wall = 0
  local abs_force= math.abs(axial_force_wall)
  global peak_force = math.max(abs_force,peak_force)
  if abs_force < peak_force*peak_fraction
    loadhalt_wall = 1
  end_if
end
;=====================================================
define loadhalt_meas
;
; Function used to stop a test when axial stress decreases to some fraction of
the peak
; Assumes measurement circle 1 is installed
;
; INPUT: peak_fraction - fraction of peak stress that dictates the stopping of
the test
;                    (global float)
;
  loadhalt_meas = 0
  local mp = measure.find(1)
  local abs_stress = math.abs(meas.stress(mp,global.dim,global.dim))
  global peak_stress = math.max(abs_stress,peak_stress)
  if abs_stress < peak_stress*peak_fraction
    loadhalt_meas = 1
  end_if
end
```

SRFT code part 5: Fracture

```
; fname: fracture.p3fis
;
; Simple environment to track fragmentation in a BPM.
; Monitor LinearPBond model "bond_break" events and turn them into
fractures.
; Use the Fragment and Ball Result logic to record fragment IDs
;
;=====================================================
define add_crack(entries)
  local contact    = entries(1)
  local mode       = entries(2)
  local strength   = entries(3)
  local frac_pos   = contact.pos(contact)
  local norm       = contact.normal(contact)
  local dfn_label  = 'crack'
  local frac_dip
  local frac_dipdir
  local frac_size = contact.prop(contact,'pb_radius')

  local len2 =
math.sqrt(comp.x(norm)*comp.x(norm)+comp.y(norm)*comp.y(norm))
  if len2 = 0
    len2 = 1
  endif
  frac_dipdir = math.atan2(comp.x(norm)/len2,comp.y(norm)/len2) /
math.degrad
  local len3 = math.sqrt(len2*len2+comp.z(norm)*comp.z(norm))
  if len3 = 0
    len3 = 1
  endif
  frac_dip = math.atan2(len2/len3,comp.z(norm)/len3) / math.degrad
  if frac_dip<0.0
    frac_dip = -frac_dip
    frac_dipdir = frac_dipdir + 180.0
  endif
  if frac_dip>90.0
    frac_dip = 180.0-frac_dip
    frac_dipdir = frac_dipdir + 180.0
  endif
  if frac_dipdir<0.0
    frac_dipdir = frac_dipdir + 360.0
  endif
  if frac_dipdir > 360.0
    frac_dipdir = frac_dipdir - 360.0
  endif
  if mode = 1 then
    ; failed in tension
    dfn_label = dfn_label + '_tension'
  else if mode = 2 then
    ; failed in shear
    dfn_label = dfn_label + '_shear'
  endif
  local arg = array.create(5)
  arg(1) = 'disk'
  arg(2) = frac_pos
  arg(3) = frac_size
  arg(4) = frac_dip
  arg(5) = frac_dipdir

  global dfn = dfn.find(dfn_label)
  if dfn = null then
    dfn = dfn.add(0,dfn_label)
  endif
  local fnew = dfn.addfracture(dfn,arg)
  dfn.fracture.prop(fnew,'failure_strength') = strength
  dfn.fracture.prop(fnew,'age')  = track_time
  crack_added = true
end

define monitor
  if crack_added = true then
    local numfrag = fragment.num()
    command
      fragment compute
    endcommand
    if fragment.num() # numfrag then
      command
        ball result generate fishtime @track_time
        wall result generate fishtime @track_time
      endcommand
      map.add(track_map,track_time,numfrag)
    endif
  endif
  crack_added = false
end

define track_time
  track_time = mech.age
end

define track_init
  command
    dfn delete
    ball result clear
    wall result clear
    fragment clear
    fragment register ball-ball
    ball result addattribute fragment
    wall result addattribute velocity
  endcommand
  ; activate fishcalls
  command
    set fishcall bond_break remove @add_crack
    set fishcall bond_break @add_crack
    set fishcall 100.0 remove @monitor
    set fishcall 100.0 @monitor
  endcommand
  ; reset global variables
  global crack_added = false
  global track_time0 = mech.age()
  command
    fragment compute
    ball result generate fishtime @track_time
    wall result generate fishtime @track_time
  endcommand
  global track_map = map(track_time,fragment.num(1))
end

define track_end
  local numfrag = fragment.num()
  command
    fragment compute
  endcommand
  if fragment.num() # numfrag then
    command
      ball result generate fishtime @track_time
      wall result generate fishtime @track_time
    endcommand
    map.add(track_map,track_time,numfrag)
  endif
  make_table
end

define make_table
  local frag1 = fragment.find(1)
  local tab = table.create('volfrag1')
  loop foreach local value map.keys(track_map)
    table(tab,value) = fragment.vol(frag1,fragment.catalog.num(value)) /
fragment.vol(frag1,1)
  endloop
end
;=====================================================
```

SRFT code part 6: Run_test

```
restore parallel_bonded

wall attribute zvelocity -0.00001 range id 2
wall attribute zvelocity -0.00001 id 3


set gravity 0 0 -9.81

;=====================================================
set echo off
call wall_function.fis
call fracture.p3fis
```

```
set echo on
;=================================================
measure create id 3 radius 0.1
history id 7 measure stresszz id 3
@ini_mstrain (3)
history id 8 @zzmstrain
set fish callback 11.0 @accumalate_mstrain
;=================================================
@wall_addr
history id 5 @axial_disp_wall
history id 6 @axial_force_wall
;=================================================
@track_init
;cycle 1000
set @peak_fraction = 0.1
;solve time 10
solve fishhalt @loadhalt_wall
@track_end
;list @peak_stress
```